Aus dem National Center for Radiation Research in Oncology – OncoRay
Direktor: Frau Prof. Dr. Mechthild Krause

Inter- and Intrafraction Motion Management for MR guided Proton Therapy of Pancreatic Carcinoma

D i s s e r t a t i o n s s c h r i f t

zur Erlangung des akademischen Grades
Doctor of Philosophy (Ph.D.)
vorgelegt
der Medizinischen Fakultät Carl Gustav Carus
der Technischen Universität Dresden
von

Sergej Schneider
aus Ust-Grjasnucha / Russland

Dresden 2020

1. Gutachter: Prof. Dr. Wolfgang Enghardt

2. Gutachter: Prof. Dr. Mark E. Ladd

Tag der mündlichen Prüfung: 04.03.2020

gez.: .....

Prof. Dr. Jörg Kotzerke

Vorsitzender der Promotionskommission

Contents

List of Figures

List of Tables

List of Abbreviations

3DPE	3D surface scan-based polyethylene
4D	Four-dimensional
AP	Anterior-posterior
bSSFP	Balanced steady-state free precession
CBCT	Cone beam computed tomography
CT	Computed tomography
DWI	Diffusion weighted imaging
EUS	Endoscopic ultrasonography
FWHM	Full half at half maximum
GRaSE	Gradient and spin echo
GRE	Gradient recalled echo
IGRT	Image guided radiation therapy
ITV	Internal target volume
IR	Inversion recovery
IS	Inferior-superior
kV	Kilovolt
Linac	Linear accelerator
LR	Left-right
MRI	Magnetic resonance imaging
PDAC	Pancreatic ductal adenocarcinoma
PE	Polyethylene
PMMA	Poly(methyl methacrylate)

PT	Particle therapy
PU	Polyurethane
PVC	Polyvinyl chloride
QA	Quality assurance
RT	Radiation therapy
RF	Radiofrequency
SE	Spin echo
SPGR	Spoiled gradient recalled echo
TE	Echo time
TI	Inversion time
TR	Repetition time
US	Ultrasound
WER	Water equivalent ratio
XT	Photon radiation therapy

1 General introduction

Background and problem statement

With an estimated 9.6 million caused deaths in 2018, cancer is one of the leading causes of mortality worldwide (Bray *et al.*, 2018). Moreover, absolute cancer incidence rates have been continuously rising and with an expanding population and life expectancy these rates are projected to increase another 62 % by 2040 (IARC, 2018). On the other hand, the five-year survival rates for most cancer sites have been increasing, e.g. in the United States from 50 % in 1970 to 67 % in 2018 (Roser and Ritchie, 2019). This directly reflects the significant improvements in the diagnostics and treatment of cancerous diseases within the last decades (Arruebo *et al.*, 2011).

Alongside with surgery and chemotherapy, radiation therapy (RT) is one of the three main pillars of modern cancer treatment (Rosenblatt and Zubizarreta, 2017). The aim of RT is to damage the DNA in clonogenic tumor cells through the exposure of high-energetic photons or particles while keeping the dose to surrounding healthy tissue as low as reasonably achievable (Baskar *et al.*, 2012). This can be performed with a curative intent to fully sterilize the tumor cells, in a preoperative (neoadjuvant)/postoperative (adjuvant) setting to reduce tumor margins before/after surgery or with a palliative intent to reduce tumor growth and relieve the pain caused by the tumor (Lutz *et al.*, 2014). RT benefited heavily from the advances in imaging technology, improving tumor visualization in RT simulation prior to dose delivery as well as allowing for the implementation of adaptive treatment strategies that use image guidance to re-optimize RT plans during the course of treatment. This allowed for escalating the radiation dose to the tumor while sparing healthy tissue to the utmost extent (Verellen *et al.*, 2008) and thereby increasing the therapeutic window.

Amongst the broad improvements in managing cancerous diseases, pancreatic cancer presents one of the indications that withstands the progress in treatment and still has an extremely poor survival prognosis with a five-year survival rate of only 7 % – 10 % (Doi *et al.*, 2008; Siegel *et al.*, 2015). This is largely due to the late diagnosis, where in more

than 80 % of the patients diagnosed with pancreatic ductal adenocarcinoma (PDAC) tumor progress is advanced and prohibits radical surgical resection. Surgical resection, however, is still considered to be the sole curative treatment option for PDAC (Hartwig *et al.*, 2011). Although it has been indicated that neoadjuvant chemo-radiotherapy increases the rate of secondary resectability (Combs *et al.*, 2013) and the rate of microscopically radical primary tumor resections (van Tienhoven *et al.*, 2011), PDAC poses a challenge for both chemo- and radiotherapy. On the one hand, PDAC presents a distinct resistance to existing drugs used in chemotherapy (Kelsen, 1994; Hajatdoost *et al.*, 2018). On the other hand, the radioresistant PDAC is surrounded by several radiosensitive organs (Goto *et al.*, 2018), e.g. the duodenum, the bowel or the stomach, and is affected by various sources of organ motion and deformation due to respiratory induced motion, organ filling or peristalsis (Keall *et al.*, 2006). Furthermore, due to the limited soft-tissue contrast of computed tomography (CT), tumor contouring based on CT varies substantially between different radiation oncologists, leading to large uncertainties in the dose distribution applied in RT (Yamazaki *et al.*, 2007; Fokas *et al.*, 2015; Versteijne *et al.*, 2017). This makes RT for patients with PDAC particular challenging and its use is therefore still controversial.

RT of PDAC may benefit from the use of magnetic resonance imaging (MRI). MRI provides a superior soft-tissue contrast compared to CT and has shown to reduce inter-observer variations in tumor contouring (Gurney-Champion *et al.*, 2017). Its functional imaging capabilities allow for a more distinct tumor staging and control of metastatic spread (Kartalis *et al.*, 2015). Its real-time imaging capability makes it furthermore promising for organ motion evaluation (Brix *et al.*, 2014). Finally, in contrast to X-ray and CT imaging, MRI is free of ionizing radiation, allowing for repetitive imaging of patients without risking radiation induced toxicities (Bujold *et al.*, 2012).

In order to cope with the challenge posed by surrounding organs at risk, patients with PDAC may benefit from particle therapy (PT) instead of receiving conventional photon therapy (XT) (Fuji *et al.*, 2013; Jouglar *et al.*, 2016). High energetic charged particles decelerate along their beam path until they eventually stop and deposit most of their energy at the end of their track at the so called Bragg Peak (Bragg and Kleeman, 1904). This effect is used in PT to deposit a high radiation dose to the tumorous target volume while sparing critical organs behind the distal end of the beam from toxic dose. However, the nature of stopping particles leads to a strong susceptibility to density changes along the beam path. Hence, both inter- and intrafraction organ motion and deformation are particularly critical in PT (Al-

bertini *et al.*, 2010) and lead to the requirement of large safety margins, which compromise the dosimetric benefit of PT.

To mitigate interfraction motion in RT, immobilization equipment is typically used such as vacuum mattresses as well as image guidance by in-room X-ray imaging for daily patient setup verification (Riou *et al.*, 2017). In the latter, volumetric cone beam CT (CBCT) or orthogonal X-ray imaging in treatment position is matched with the CT images used for treatment planning or from CT generated digitally reconstructed radiographs, respectively. Since abdominal organs like the pancreas are poorly visualized under X-ray guidance, radiopaque solid fiducial markers are often implanted in close proximity to the tumor to facilitate co-registration of the X-ray images with the planning CT scan. These markers, however, may deteriorate image quality in CT and MRI by causing streaking artefacts in the former and geometric image distortions in the latter imaging modality (Gurney-Champion *et al.*, 2015). This may lead to errors in dose calculation or an inaccurate co-registration of CT and MR images. Furthermore, solid markers may cause significant local dose perturbations in PT (Giebeler *et al.*, 2009). Injectable liquid fiducial markers are therefore currently being developed that offer multiple advantages over solid markers such as good visibility in CT at less image degradation, low dose perturbation in PT and higher flexibility in injection (Bair *et al.*, 2015; Scherman Rydhög *et al.*, 2015). Their MRI performance for the use in pancreas tissue, however, has yet to be assessed.

Intrafraction motion of highly mobile organs like the pancreas, on the other hand, is commonly being coped with by the use of internal target volume (ITV) margins based on respiratory correlated CT (4D-CT) (Karava *et al.*, 2017). With these margins the aim is to achieve full dose coverage of the tumor in all respiratory states, including geometric errors due to positioning uncertainties, while simultaneously accepting a high dose in the included surrounding healthy tissue. For pancreas tumor motion, however, it has been shown that treatment planning based on 4D-CT is unable to accurately predict motion during the course of therapy due to inter- and intrafraction irregularities (Minn *et al.*, 2009; Ge *et al.*, 2013). This is why a mitigation of intrafraction motion during RT is often recommended to allow a reduction of ITV margins and reduce uncertainties in dose delivery. Respiratory motion is commonly mitigated through abdominal compression. Due to the strong susceptibility of PT to density changes along the beam path and since for PDAC the equipment for abdominal compression is positioned on the same axis than the target volume, care has to be taken that this equipment does not increase dose delivery uncertainties by a non-reproducible

impact on the range of the traversing beam.

The need for improved soft-tissue contrast in abdominal imaging and the susceptibility of PT to motion leads to an increased interest in the integration of MRI into the treatment planning and dose delivery workflow (Oborn *et al.*, 2017). In a technically simple approach, the integration can be approached by MRI simulation, where MRI is utilized for the delineation of relevant tumor and organ structures (Gurney-Champion *et al.*, 2017), tumor motion assessment for the definition of personalized treatment margins (Stemkens *et al.*, 2016), or is used for RT planning based on synthetic CT images generated from MRI (Hsu *et al.*, 2019). In a technically more challenging approach, MR guidance of PT can be performed, in which the treatment setup and dose delivery is adapted based on MRI. MRI is, however, particularly susceptible to geometric distortions and image artefacts, which is why the quantification of physiological properties by the use of MRI has to be thoroughly validated with ground truth measurements, which can be provided by MRI phantoms.

While a variety of concepts have been developed for the management of inter- and intrafraction pancreas tumor motion in conventional X-ray guided RT, the translation to MR guided PT is not generally feasible or is often connected with severe drawbacks (Bolsi *et al.*, 2018). Hence new concepts have to be developed and tested which correspond with the safety regulations and technical demands of MR guided PT.

Aims and hypotheses

The aim of this thesis is therefore threefold. Firstly, for interfraction motion management, a novel liquid fiducial marker, which has been shown both to be visible in X-ray imaging and not to significantly perturb the local dose distribution applied by PT, is tested regarding its applicability in MR guidance for PT of PDAC. It is hypothesized that this marker is detectable in MRI when injected in pancreas tissue and reduces the amount of MR image degradation relative to solid fiducial markers.

Secondly, for intrafraction motion mitigation the concept of applying abdominal pressure through the use of an MR compatible patient-specific corset, previously presented for use in XT, is adapted for the use in PT. For this, initially three different types of abdominal corsets are tested regarding their suitability for PT. Subsequently, with the corset considered most suitable, a clinical study is conducted to analyze the reduction of respiratory induced pancreas motion by use of time-resolved 2D-cine and respiratory correlated 4D-

MRI on a diagnostic 3.0 T MRI scanner. It is hypothesized that an abdominal corset can be implemented into the PT workflow, reduces the respiratory induced pancreas motion and is tolerated by patients with abdominal tumors.

Thirdly, to assess the accuracy that the diagnostic 3.0 T MRI scanner provides for motion characterization purposes, it's motion tracking performance had to be first evaluated with ground truth measurements. Hence, a 4D-MRI motion phantom is commissioned and implemented for quality assurance (QA) of motion depicting MRI pulse sequences and geometric fidelity. It is hypothesized that this motion phantom, originally designed for a hybrid MR-Linac system, can be implemented on a diagnostic 3.0 T MRI scanner and used therein for QA of motion depicting MRI pulse sequences and scan protocols.

Structure of the thesis

To motivate the experimental approaches and establish a theoretical foundation regarding the research aims, the clinical rational for- and state of the art of image- and especially MR guided PT of PDAC is introduced in **chapter 2**. The theoretical background of quantitative MRI will be discussed in detail to establish a foundation for quantitatively evaluating the MRI characteristics of the novel liquid fiducial marker for its use in MR guidance. In **chapter 3** these characteristics are analyzed and compared to two clinically used solid fiducial markers in a quantitatively manner in the framework of a phantom study. Furthermore, the liquid marker is tested for the first time in *ex vivo* tumorous pancreas tissue to examine its MRI visibility in human pancreas tissue. In **chapter 4**, the commissioning of the MR-Linac motion phantom on the 3.0 T diagnostic MR scanner will be described. Furthermore, a software tool will be developed for an automatic assessment of the geometrical fidelity and motion tracking accuracy of the scanner by use of this phantom for QA purposes. In **chapter 5** three different MR compatible abdominal corsets are tested regarding their applicability in PT. Subsequently, the MR pulse sequences previously tested with the motion phantom are used for analyzing the reduction of respiratory pancreas motion by application of an MR- and PT compatible abdominal corset within a patient study. The clinical implementation will be described, the patient's tolerance towards such a corset presented and the achieved reduction of pancreas motion assessed. Finally, the advances in knowledge and future perspectives of the reasearch conducted for this thesis are discussed in **chapter 6**. A summary can be found in **chapter 7** and **chapter 8** in English and German, respectively.

2 State of the art: MRI for image guided PT of pancreatic cancer

This chapter is a short theoretical introduction to the subjects relevant for this thesis and is not raising claim for completeness. Reference is made to comprehensive literature for a thorough study of the clinical rational for PT of PDAC (Robin and Goodman, 2017), the physical background of PT (Dosanjh and Bernier, 2018), the principles of MRI (Brown and Semelka, 2003) and practical applications of MR guidance in RT (Liney and van der Heide, 2019).

2.1 Clinical rationale for particle therapy of pancreatic cancer

Although pancreatic cancer is currently only the twelfth most common malignancy worldwide, its burden on society is increasing, particularly in countries with a high human development index (Wong *et al.*, 2017), e.g. in North America and Western Europe, where it is projected to be the second and third most common cause of cancer related death by 2030, respectively (Roser and Ritchie, 2019). This trend is influenced both by rising incidence rates as well as the poor treatment outcome with a five-year survival rate of only 7 % – 10 % (Doi *et al.*, 2008; Siegel *et al.*, 2015). Radical surgery is thereby still considered the only curative treatment option. However, due to the typically late diagnosis and the consequentially high rate of tumor progression, surgical resection is only an option for approximately 20 % of patients (Hartwig *et al.*, 2011). This can either be due to distant metastatic spread or due to local infiltration of crucial blood vessels (portal vein, mesentric artery, mesentric vein) located directly adjacent to the pancreatic head and body, as can be seen in Figure 2.1. Patients that undergo surgical resection, however, still frequently develop systemic (> 70 %) or local (> 20 %) disease recurrence (Vincent *et al.*, 2011).

It has been indicated that a combined neoadjuvant chemo-RT increases the rate of microscopically radical primary tumor resections (van Tienhoven *et al.*, 2011). For patients

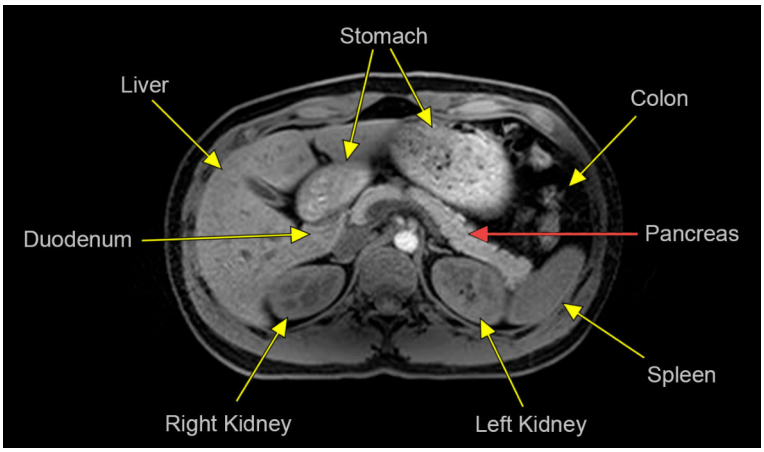

Figure 2.1: Transverse T_1 weighted MR image showing the pancreas (red arrow) in close proximity to several organs (yellow arrows), which limit the possible dose to a target volume in PDAC.

with unresectable PDAC, it has been shown that it increases the median survival (Moertel *et al.*, 1981) and furthermore yields a 30 %−40 % rate of secondary resectability (Combs *et al.*, 2013) which improves median survival up to 21 months, comparable to patients with primarily resectable PDAC (Gillen *et al.*, 2010). Using stereotactic radiosurgery local disease control was shown to be improved relative to conventional chemo-RT (Didolkar *et al.*, 2010). In the study by Didolkar *et al.* (2010) it was also shown that gastrointestinal toxicity rates were reduced when tumor tracking was performed and consequently the dose to the healthy tissue was reduced. Since the pancreas is in close proximity to several organs at risk (see Figure 2.1), the dose that can be deposited to PDAC without inducing severe gastrointestinal toxicities is limited. Considering the substantial rate of secondary resectability after radiotherapy and the favorable normal-tissue dose sparing capabilities over XT, patients with resectable, unresectable or borderline PDAC might benefit from PT. Furthermore, due to the superb soft-tissue contrast and real-time imaging capability of MRI, PT of PDAC might benefit from image guidance by MRI.

2.2 Particle therapy

PT using protons or heavier ions like helium or carbon is increasingly being investigated as alternative for XT in thoracic and abdominal tumors. This is mainly motivated by the beneficial dose distribution achievable in PT (Wilson, 1946) due to the inverse depth-dose profile found in charged particles (Bragg and Kleeman, 1904). This inverse depth-dose

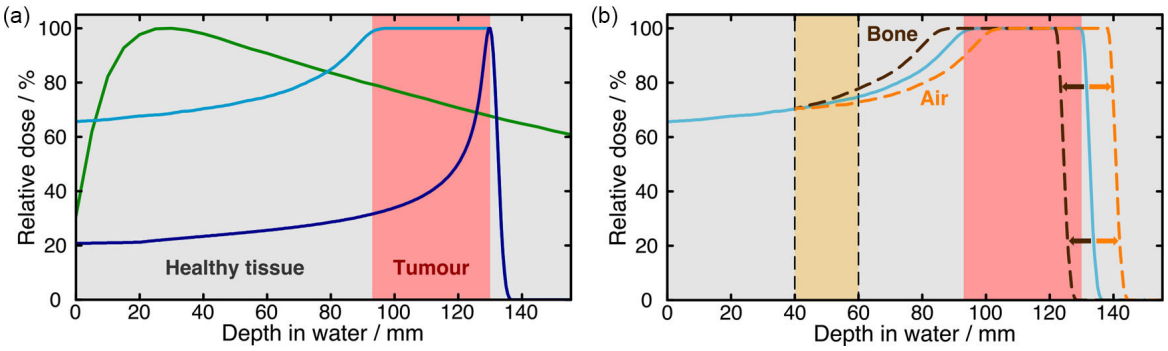

Figure 2.2: *(a)* Depth-dose profile of a 15 MeV photon beam (green), a mono-energetic 135 MeV proton beam (purple) and a multi-energy proton spread-out Bragg peak in water to homogeneously cover a hypothetical tumor (red) with the prescribed dose. *(b)* Dose variations in a proton spread-out Bragg peak due to change in anatomy due to an air or bone insert (yellow) in the beam path. The under-dosage of the tumor and the over-dosage of the surrounding healthy tissue (light blue) is visualized in the two scenarios (brown, orange). (Image courtesy: Dr. Wohlfahrt.)

profile allows for minimizing the dose to organs at risk beyond the distal end of the beam (Durante and Loeffler, 2009) as visualized in Figure 2.2 (a). Moreover, PT provides a higher relative biological effectiveness than XT (Lühr *et al.*, 2018).

Charged particles with clinically relevant energies per nucleon of up to $\sim$400 MeV/u transfer their energy primarily through the mechanism of inelastic Coulomb scattering with the shell electrons of the target tissue. The energy transfer dE within a path length dx can hence be approximated by the Bethe-Bloch formula (Bethe, 1930; Bloch, 1933)

$$-\frac{dE}{dx} \approx k_0 \frac{z^2}{\beta^2} \frac{Z}{A} \rho \left[\ln\left(2m_e c^2 \frac{\beta^2}{1-\beta^2} \right) - \beta^2 - \ln I \right], \tag{2.1}$$

where k_0 is a constant scaling factor, z is the nuclear charge and β the velocity of the projectile and Z is the atomic number and A the atomic mass of the target nuclei, as well as ρ the target's density and I its ionization potential. From equation 2.1 it follows that charged particles deposit most of their energy at the end of their track, after having been slowed down continuously, and stop at the so-called Bragg peak. This is contrary to the dose deposition by high-energetic photons, where after an initial dose build-up, the deposited dose decays exponentially with the traversed path length. In state-of-the-art RT, termed intensity-modulated RT (IMRT), implemented both for XT and PT, multiple treatment beams of varying intensities are applied from different beam directions to deliver the prescribed dose to the tumor while limiting the volume of healthy tissue exposed to high dose. The steep gradient dose fall-off of PT at the Bragg peak leads to a high sensitivity to density

changes along the beam path, as visualized in 2.2 (b). PT is therefore especially susceptible to inter- and intrafraction motion due to patient mis-positioning, respiratory induced motion, stomach and bowel filling or peristalsis.

2.3 Magnetic resonance imaging

2.3.1 Physical background

The fundamental basis of MRI is the quantum-mechanical energy separation ΔE observed in a system of nuclei with a non-zero spin exposed to a static magnetic field $\mathbf{B_0}$, termed nuclear Zeeman effect (Zeeman, 1896; Preston, 1898). Hydrogen nuclei, most commonly used in clinical MRI due to their high abundance in living organisms, are thereby separated into two energy states with the energy difference

$$\Delta E = \hbar\omega_0 = \hbar\gamma \mathrm{B}_0, \tag{2.2}$$

where $\hbar$ is the Planck constant and $\gamma/2\pi = 42.6\,\mathrm{MHz}\cdot T^{-1}$ the gyromagnetic ratio of the proton. The energy separation can be classically understood as orientation of the z component of the nuclei's magnetic momentum parallel (N_+) and anti-parallel (N_-) relative to the static magnetic field. The two energy states are thereby unequally occupied towards the lower energy state N_+ given by the ratio

$$\frac{N_+}{N_-} = e^{\frac{\Delta E}{k_B T}}, \tag{2.3}$$

with the Boltzmann constant k_B and the temperature T. The excess spins in the lower energy state lead to a net magnetization $\mathbf{M_0}$ of the tissue parallel to the static magnetic field. The net magnetization can be manipulated by excitation through a radiofrequency (RF) pulse ($\mathbf{B_1}$) with the resonance frequency ω_0 and an orientation perpendicular to $\mathbf{B_0}$. This excites the protons from the N_+ state to the N_- state and vise versa stimulates the release of energy from the protons in the N_- state which will then occupy the N_+ state. This effectively describes a rotation of the net magnetization $\mathbf{M_0}$ to a higher energy state. The rotation of $\mathbf{M_0}$ is thereby perpendicular to both $\mathbf{B_0}$ and $\mathbf{B_1}$ and thereby creates a new longitudinal magnetization $\mathbf{M_z}$ and a transverse magnetization component $\mathbf{M_{xy}}$, precessing around $\mathbf{B_0}$. The respective magnitude of $\mathbf{M_z}$ and $\mathbf{M_{xy}}$ after excitation depends on the

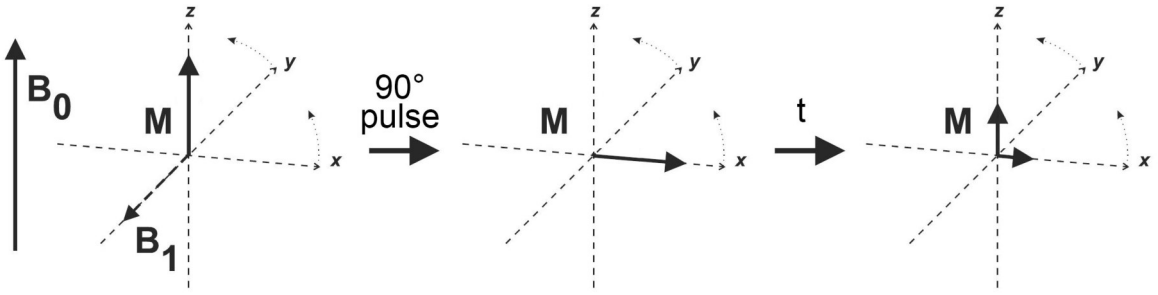

Figure 2.3: Schematic visualization of net magnetization flip towards the transverse plane in a rotating frame after RF excitation with a 90° pulse. After the time t the net magnetization shows partial longitudinal and transverse relaxation towards it's equilibrium state.

length and magnitude of the $\mathbf{B_1}$ pulse, described by the flip angle α. The excitation of $\mathbf{M_0}$ is schematically shown in Figure 2.3 in a rotating frame for an excitation pulse of $\alpha = 90°$.

After excitation, the system will de-excite into the equilibrium while emitting an RF signal with the frequency ω_0 (Bloch, 1946). The de-excitation of the net magnetization towards equilibrium, termed relaxation, is a statistical process and is defined by the macroscopic relaxation times T_1 and T_2. The longitudinal relaxation time T_1, or spin-lattice relaxation time, is the time required for $\mathbf{M_z}$ to return to 63 % of $\mathbf{M_0}$, i.e.

$$M_z(t) = M_0 - M_0 \cdot e^{-t/T_1} \cdot (1 - \cos\alpha). \tag{2.4}$$

The transverse relaxation time T_2, or spin-spin relaxation time, on the other hand, is the time required for $\mathbf{M_{xy}}$ to decay to 37 %, i.e.

$$M_{xy}(t) = M_0 \cdot e^{-t/T_2} \cdot \sin\alpha. \tag{2.5}$$

These relaxation times are material specific parameters, since they describe the rate of energy transfer from excited protons to their molecular environment (spin-lattice relaxation) and the energy transfer and dephasing within the spin system (spin-spin relaxation). The material specific properties $\mathbf{M_0}$ (which is directly proportional to the tissues spin or proton density ρ(H)), T_1 and T_2 are the basis for the superb soft-tissue contrast of MRI.

In a classical spin-echo (SE) sequence the MR signal is sampled after an echo time (TE) where at t = TE/2 the magnetization is flipped with $\alpha = 180°$ to create an *echo* of the dephasing spins during signal sampling at t = TE. In a more sophisticated gradient-recalled echo (GRE) sequence this echo is induced by fast switching of the frequency gradient coils,

which leads to an accelerated decay of the transverse coherence with the relaxation time T_2^*, for which

$$1/T_2^* = 1/T_2 + \gamma \Delta \mathrm{B}_0 \tag{2.6}$$

depending on the inhomogeneity of the local static magnetic field $\Delta \mathrm{B}_0$.

From this magnetic resonance, in an idealistic scenario one would only retrieve a single RF signal with a frequency ω_0 and an amplitude proportional to ρ(H). In order to create a 3D image, sophisticated spatial encoding is performed by the use of magnetic gradient fields. The gradient fields alter the static magnetic field in all three directions, thereby allowing for slice selected excitation (slice-encoding direction), frequency encoded signal sampling (frequency-encoding direction) and phase encoded signal sampling (phase-encoding direction) through repeated excitations at different phase gradient strengths. The excitation is therefore repeated after the repetition time (TR).

The combination of the tissue specific properties ρ(H), T_1 and T_2 with the variability of pulse sequence parameters TE, TR and α yields the potential for numerous different contrasts of identical tissue. This versatility of MRI allows, on the one hand, for superb soft-tissue contrast of different body regions but also leads to the preferred use of MRI as qualitative imaging modality.

2.3.2 Quantitative MRI

A possible method for quantitative imaging with MRI is to directly deduce the tissue specific parameters (ρ(H), T_1, T_2) by relaxometry instead of creating a qualitative signal contrast. By performing relaxometry, quantitative information correlated to pathophysiology can be retrieved. However, since relaxometry *in vivo* is highly non-trivial, lacks robustness and typically requires long acquisition times, it is not standard of care in clinical routine. In this chapter, different methods for quantification of ρ(H), T_1, T_2 and T_2^* will be shortly discussed, as they will be used primarily in chapter 3 of this thesis.

T_1 mapping

IR SE method The gold standard of measuring longitudinal relaxation times T_1 in MRI is based on an inversion recovery (IR) spin echo (SE) method (Kingsley *et al.*, 1998). Here

the signal intensity of the tissue is measured after the application of an inversion pulse ($\alpha = 180°$) at different inversion times (TI) with a subsequent SE acquisition. Under assumption of perfect 180° and 90° RF pulses the signal intensity is given by

$$SI(TI)_{IRSE} = M_0 \left(1 - 2e^{-\frac{TI}{T_1}} + e^{-\frac{TR}{T_1}}\right). \tag{2.7}$$

This acquisition effectively samples the longitudinal magnetization during longitudinal relaxation. When TR is hold constant during the different TI acquisitions, T_1 can be retrieved directly from the exponential fit.

VFA method A faster approach to quantify T_1 in MRI is by utilizing a spoiled gradient recalled echo (SPGR) sequence with multiple low flip angles, where transverse coherence is actively disrupted after every sampling (Haase *et al.*, 1986). The signal intensity of a SPGR sequence with a flip angle α is a function of T_1 and given by (Cheng and Wright, 2006)

$$SI_{SPGR}(T_1) = M_0 \cdot \sin\alpha \cdot \frac{1 - e^{\frac{-TR}{T_1}}}{1 - e^{\frac{-TR}{T_1}} \cdot \cos\alpha}. \tag{2.8}$$

When equation 2.8 is linearized with $E = e^{\frac{-TR}{T_1}}$, it follows that

$$\frac{SI_{SPGR}(T_1)}{\sin\alpha} = E \cdot \frac{SI_{SPGR}(T_1)}{\tan\alpha} + M_0(1 - E), \tag{2.9}$$

where T_1 can be extracted from the slope E of the linear function

$$T_1 = -TR/\ln(E). \tag{2.10}$$

Since this approach is sensitive on the effective flip angle α applied, one has to consider the spatial dependence of α given by the RF transmit profile B_1^+

$$\alpha(x, y) = \alpha \cdot B_1^+(x, y). \tag{2.11}$$

B_1^+ map Based on the principle of reciprocity (Hoult, 2000) the RF transmit profile B_1^+ is correlated to the RF receive profile B_1^-. When B_1^- is approximated to be equal to B_1^+, it can

be determined utilizing a dual-repetition time GRE sequence (Yarnykh, 2007)

$$\mathrm{B}_1 = \mathrm{acos}\left(\frac{\frac{S(TR_2)}{S(TR_1)} \cdot \frac{TR_2}{TR_1} - 1}{\frac{TR_2}{TR_1} - \frac{S(TR_2)}{S(TR_1)}}\right), \tag{2.12}$$

where $S(TR_{1,2})$ is the signal intensity of the GRE sequence with the repetition time $TR_{1,2}$, respectively.

T_2 mapping The gold standard for mapping the transverse relaxation time T_2 is measuring the exponential signal decay in a SE sequence at different TE. In a SE sequence the signal intensity is given by

$$SI_{SE} = k \cdot \rho(H) \cdot \mathrm{B}_1^- (1 - e^{-\frac{TR}{T_1}}) \cdot e^{-\frac{TE}{T_2}}, \tag{2.13}$$

with the proton density $\rho(H)$, the receiver coil profile B_1^- and a scaling factor k, including amongst others the receiver coil sensitivity (Muir and J Balcom, 2013).

T_2* mapping The transverse relaxation time T_2* manifests in an accelerated decay of transverse magnetization under the application of a gradient echo acquisition. In a GRE sequence the signal intensity is given by

$$SI_{\mathrm{GRE}} = k \cdot \rho(H) \cdot \mathrm{B}_1^- \cdot \sin(\mathrm{B}_1^+ \cdot \alpha) \cdot \frac{1 - e^{-\frac{TR}{T_1}}}{1 - \cos(\mathrm{B}_1^+ \cdot \alpha) \cdot e^{-\frac{TR}{T_1}}} \cdot e^{-\frac{TE}{T_2^*}} \tag{2.14}$$

and can hence be simply retrieved by fitting the exponential signal decay in a multi-echo gradient recalled echo (GRE) sequence (Sabati and Maudsley, 2013).

Δ $\mathbf{B}_0$ mapping The amount of transverse spin dephasing in between two GRE acquisitions at two different TE directly correlates with the homogeneity of the static magnetic field $\Delta\mathrm{B}_0$. This allows to map $\Delta\mathrm{B}_0$ when the phase information $\phi_{1,2}$ at different $\mathrm{TE}_{1,2}$ is acquired (Windischberger *et al.*, 2004) by

$$\Delta\mathrm{B}_0 = \frac{\phi_2 - \phi_1}{2\pi \cdot \gamma \cdot (TE_2 - TE_1)}. \tag{2.15}$$

2.3.3 MRI simulation and guidance for PT

MRI can be integrated in the RT workflow in various ways and can therein be used in both simulation and image guidance (Devic, 2012; Pollard *et al.*, 2017). The level of integration of MRI in PT lags behind that already found in XT (Paganelli *et al.*, 2018) but shall be shortly discussed with already achieved and yet to be developed applications.

MR simulation The superb soft-tissue contrast of MRI seemingly makes it an ideal modality for tumor- and organs at risk contouring in RT planning. However, in contrast to CT, MRI does not inherently provide information about the electron density of the tissue. The electron density information is, however, mandatory for dose calculation since the attenuation of radiation directly relates to this tissue property. In combination with its high geometrical fidelity, this characteristic made CT the backbone of treatment simulation in RT. The utilization of MRI in RT planning for target volume delineation was yet still suggested early on (Fraass *et al.*, 1987). In the first approach, which is still most common to date, MRI was used solely for the delineation of the tumor and potentially also for the organs at risk. The delineation of e.g. pancreas or prostate tumors based on MRI has thereby shown to reduce inter-observer variability (Villeirs *et al.*, 2005; Gurney-Champion *et al.*, 2017). The tumor and organ contours delineated are subsequently transferred from MRI to CT, after non-rigid coregistration of the MRI dataset with a CT dataset, which is later used for dose calculation and optimization. In this approach patient position verification in treatment position is still commonly performed by X-ray based image guidance. The poor soft-tissue contrast of orthogonal X-ray or CBCT, however, requires the use of fiducial markers to facilitate accurate interfraction positioning of mobile tumors like PDAC (Varadarajulu *et al.*, 2010; Van der Horst *et al.*, 2013). Hence, the MR simulation workflow would benefit from fiducial markers visible in both X-ray and MR based image modalities.

A method that is recently getting more attraction, particularly through the implementation of machine learning techniques, is the MR-only treatment planning workflow. Here, MR images are both used for delineation and dose calculation after planning by converting MR images to synthetic CT images. This conversion can be performed by an atlas-based approach (Demol *et al.*, 2016), based on non-rigid registration of the patients MRI data to a CT atlas. Furthermore, a signal intensity-based approach can be used (Tyagi *et al.*, 2017), where voxels within certain signal thresholds are overwritten with a pre-defined bulk elec-

tron density value (Hsu *et al.*, 2019), or alternatively by a sophisticated machine learning approach (Maspero *et al.*, 2018). MR-only treatment planning has shown high accuracy for both XT (Edmund and Nyholm, 2017) as well as PT (Koivula *et al.*, 2016; Maspero *et al.*, 2018) for indications like brain or prostate tumors but has yet to prove itself for the treatment planning of PDAC.

For treatment planning of tumors that show high intrafraction mobility, e.g. for abdominal tumors, simulation can include a tumor motion assessment. This allows for intrafraction motion management by addition of treatment margins to the target volume (van Herk, 2004). These margins aim to cover the tumor in all respiratory states during dose delivery, while simultaneously accepting higher dose to the included surrounding healthy tissue, and are commonly retrieved from respiratory gated 4D-CT images. Motion assessment based on 4D-CT, however, has shown to be susceptible to measurement errors by both under- and overestimating motion of abdominal and thoracic tumors (Dou *et al.*, 2015). The real-time imaging capability and high soft-tissue contrast of MRI makes it an ideal imaging modality for soft-tissue motion characterization. During treatment simulation, respiratory gated 4D-MRI has shown to provide accurate motion information (Bernatowicz *et al.*, 2016), where the respiratory states reconstructed from MRI are registered to a static CT image for 4D-CT dose calculations.

MR guidance After simulation for treatment planning, MRI can furthermore be utilized in different levels of technical integration for guidance of RT. In an off-line guidance approach, MRI can be used for an adaption of the treatment in case of changing tumor size or pathological response to treatment (Chandarana *et al.*, 2018). For off-line guidance, the patient is not required to be positioned at the treatment machine.

In the near-room approach, the designated MRI scanner is installed close to the treatment room to facilitate a shuttle-based transport in between the two. This is performed to benefit from the soft-tissue contrast provided by MRI while minimize anatomical changes in between off-line imaging and treatment. For a final position verification, however, X-ray imaging in at the treatment machine is still often necessary. The feasibility of this approach has been shown for MR guided XT (Bostel *et al.*, 2018).

With the in-room approach, the patient is scanned in treatment position while the scanner or the treatment couch are moved to furthermore reduce changing of anatomy in between imaging and treatment. While this method has been implemented clinically for neurosurgery

with a movable 1.5 T MR scanner (Chicoine *et al.*, 2011) and for MR guided XT (Jaffray *et al.*, 2014), the clinical integration of a movable in-room MR scanner in a PT facility has yet to be performed.

The highest possible level of integration is achieved with an in-beam approach in which the MRI scanner is physically integrated with the treatment machine. This allows for an imaging of the patient in the iso-center of the treatment beam and hence an off-line or on-line image based adaption without the requirement of patient repositioning. Moreover, an MR integrated system allows for the possibility of a real-time adaption of the treatment beam if the MR scanner and treatment machine are synchronized, fully exploiting the real-time imaging capability and high soft-tissue contrast of MRI. This level of integration has already been clinically introduced for XT in hybrid MR-Linac devices (Mutic and Dempsey, 2014; Raaymakers *et al.*, 2017). For PT a simultaneous proton beam irradiation and in-beam MR imaging has been shown technically feasible but the development of an integrated MR-PT system is still in its infancy (Oborn *et al.*, 2015; Schellhammer *et al.*, 2018).

3 Liquid fiducial marker for MR guided particle therapy

For several primary tumors, solid gold fiducial markers have replaced bony anatomy based X-ray position verification in RT as standard of care and thereby reduced residual setup errors (Varadarajulu *et al.*, 2010; Van der Horst *et al.*, 2013). Fiducial markers are implanted into the pancreas using endoscopic ultrasonography (EUS), a procedure that is well established and generally well tolerated (Park *et al.*, 2010). However, solid markers deteriorate image quality in CT (Scherman Rydhög *et al.*, 2017) and MRI (Gurney-Champion *et al.*, 2015), thereby hampering target volume delineation and image co-registration. Moreover, due to their high *Z*-elemental composition these markers have shown to significantly perturb the local dose distribution in particle therapy up to 80% (Newhauser *et al.*, 2007; Giebeler *et al.*, 2008; Habermehl *et al.*, 2013). Increased effort is therefore being put into the development of injectable liquid fiducial markers that may offer multiple advantages over solid markers such as: 1) good visibility in CT at less image degradation and 2) low dose perturbation in PT as well as 3) higher flexibility in injection (Bair *et al.*, 2015; Scherman Rydhög *et al.*, 2015). Their performance in MRI, however, has yet to be assessed.

The aim of this work is therefore to test a novel liquid fiducial marker (BioXmark® , Nanovi Radiotherapy A/S, Lyngby, Denmark) regarding its applicability for MR guidance in particle therapy. The marker has already been shown to be adequately visible in kilovolt (kV) X-ray, CT, CBCT and ultrasound (US) imaging and did not significantly perturb proton beam dose distributions (Scherman Rydhög *et al.*, 2017). Moreover, the marker has been shown to stay chemically stable after normo-fractionated and high-dose single-fraction proton irradiation schemes (Troost *et al.*, 2017) and has recently been validated in its long-term positional and structural stability in lung cancer patients 36 months after initial XT irradiation (De Blanck *et al.*, 2018).

At the time this study was initiated, the MRI properties of this liquid marker had not been investigated and a CE certification for its use in abdominal cancer patients was pending.

In order to compare the visibility and induced artefacts of the liquid fiducial marker in MRI with two clinically used solid gold fiducial markers, an MRI phantom was designed to mimic the relaxation properties of pancreatic tissue at a magnetic field strength of 3.0 T. Since visibility and artefacts of markers in MRI are heavily dependent on pulse sequence parameters (Rouvière *et al.*, 2006; Jonsson *et al.*, 2011; Rylander *et al.*, 2011), relaxometry was performed to evaluate visibility and the induced artefacts in a quantitative, sequence independent manner based on the methods proposed by Gurney-Champion *et al.* (2015). Finally, due to the pending CE certification for the liquid marker to be used in abdominal cancer patients, an *ex-vivo* study was conducted in which the liquid marker was injected into freshly resected tumorous pancreas tissue and qualitatively evaluated regarding its visibility in CT and MR imaging.

The results of these studies have been published by Schneider *et al.* (2018) and Schneider *et al.* (2019b), respectively. The design and manufacturing of the phantom described in this section was performed in cooperation with Nanovi Radiotherapy A/S. Gold Anchor™ and VisiCoil™ fiducial markers were kindly provided by Naslund Medical AB and IBA Dosimetry GmbH, respectively. BioXmark® was provided by Nanovi Radiotherapy A/S.

3.1 Phantom for quantification of MRI properties of fiducial markers

3.1.1 Composition of pancreas tissue equivalent gel phantom

A gel matrix was prepared mimicking the relaxation behavior of pancreatic tissue at 3.0 T ($T_1 = 725\,\text{ms} \pm 71\,\text{ms}$, $T_2 = 43\,\text{ms} \pm 7\,\text{ms}$) as reported in literature (De Bazelaire *et al.*, 2004). The gel composition was based on the evaluation and empirical model by Hattori *et al.* (2013) describing the dependency of T_1 and T_2 relaxation times to the concentrations of agarose, gadolinium chloride and sodium chloride in a carrageenan-based gel. Resulting from this model, a composition of 1.0 w/w % carrageenan, 0.03 w/w % sodium azide, 0.291 w/w % sodium chloride, 97.6 µmol/kg gadolinium chloride and 1.22 w/w % agarose dissolved in Milli-Q water is proposed to achieve the pancreas tissue equivalent relaxation properties at 3.0 T. For validation and to allow for a final adjustment of the relaxation behavior, a set of four gel samples were initially prepared with varying agarose concentrations from 1.0 w/w – 2.0 w/w % while the other parameters remained constant. A fifth sample filled

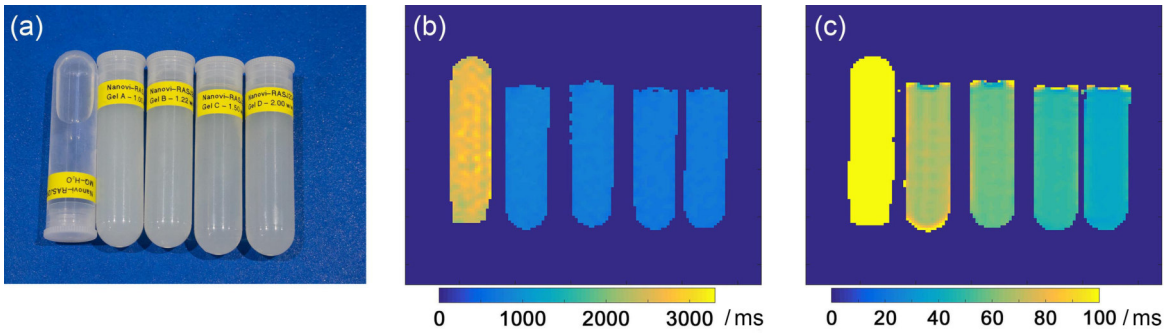

Figure 3.1: *(a)* Image of tested samples positioned in 8-channel head coil showing (from left to right) the sample filled with water and the four samples filled with gel of different agarose concentrations (1.0 w/w % – 2.0 w/w %). *(b)* T_1 map calculated based on dual-echo gradient echo sequence with varying flip angles. *(c)* T_2 map calculated based on 8-echo spin echo sequence with increasing echo time. To visualize the differences in T_2 found in the samples, the calibration window was chosen to be [0 – 100] ms, leading to the saturation of the water sample, which revealed a T_2 relaxation time of 1448 ms $\pm$ 101 ms.

with pure water was dedicated as control tube with known relaxation behavior ($T_1 = 2.9$ s, $T_2 = 1.4$ s) (Coletta, 2001) to assure the used sequences and fitting procedures performed accurately. The four samples along with a reference tube filled with water were scanned with a 3.0 T Philips Ingenuity TF PET / MR scanner using an 8-channel head coil (Philips Ingenuity TF PET/MR scanner, Philips Healthcare, Eindhoven, The Netherlands).

Determination of the T_1 relaxation time was based on the variable flip angle method (Haase *et al.*, 1986) utilizing a spoiled gradient echo (SPGR) sequence with two flip angles as described in 2.3.2. For correction of spatial inhomogeneities in the RF transmit-field (B_1^+), a B_1^+-map was additionally calculated based on a gradient echo sequence with two repetition times as described in 2.3.2. The T_1-map was corrected according to equation 2.11. T_2 mapping was performed based on a spin echo sequence with eight echo times, where T_2 was deduced as the exponential fit parameter of the observed voxel-wise signal

Table 3.1: Measured mean and standard deviation of T_1 and T_2 relaxation times of gel samples with varying agarose concentration (1.0 w/w – 2.0 w/w %) and a sample with Milli-Q water as reference sample.

Sample	MQ-H_2O	1.0 w/w %	1.22 w/w %	1.5 w/w %	2.0 w/w %
T_1 / ms	2630 ± 82	793 ± 12	769 ± 12	721 ± 11	721 ± 10
T_2 / ms	1448 ± 101	64.7 ± 0.7	56.0 ± 0.5	47.9 ± 0.6	38.9 ± 0.5

decay. Both mapping procedures included a masking of the background noise. The relevant MRI sequence parameters can be found in the supplementary Table A.1. The resulting T_1 and T_2 maps (see Figure 3.1) were manually segmented to measure the mean relaxation time of the respective sample. Based on the results shown in Table 3.1, the gel composition leading to an optimal pancreas tissue equivalency was therefore projected at an agarose concentration of 1.8 w/w %. It should be noted, however, that the measured T_1 value of all four gel samples as well as the T_2 value of two out of four gel samples (1.22 w/w – 2.0 w/w %) coincided with the literature values ($T_1 = 725\,\text{ms} \pm 71\,\text{ms}$, $T_2 = 43\,\text{ms} \pm 7\,\text{ms}$ (De Bazelaire *et al.*, 2004)) of pancreas tissue at 3.0 T.

3.1.2 Phantom design

Following the results of section 3.1.1 a gel matrix (725 g) was prepared with an agarose concentration of 1.80 w/w %. The gel components (carrageenan (7.25 g, 1.0 w/w %), sodium azide (217.5 mg, 0.03 w/w %), sodium chloride (2.11 g, 0.291 w/w %), gadolinium chloride (26.4 mg, 97.6 µmol/kg) and agarose (13.05 g, 1.8 w/w %)) were dissolved in Milli-Q water (702.7 g) in a boiling water bath for 2 h with constant stirring. Air bubbles were removed using sonication, to reduce susceptibility inhomogeneities and consequently potential static magnetic field inhomogeneities in the phantom material. The gel matrix was enclosed by

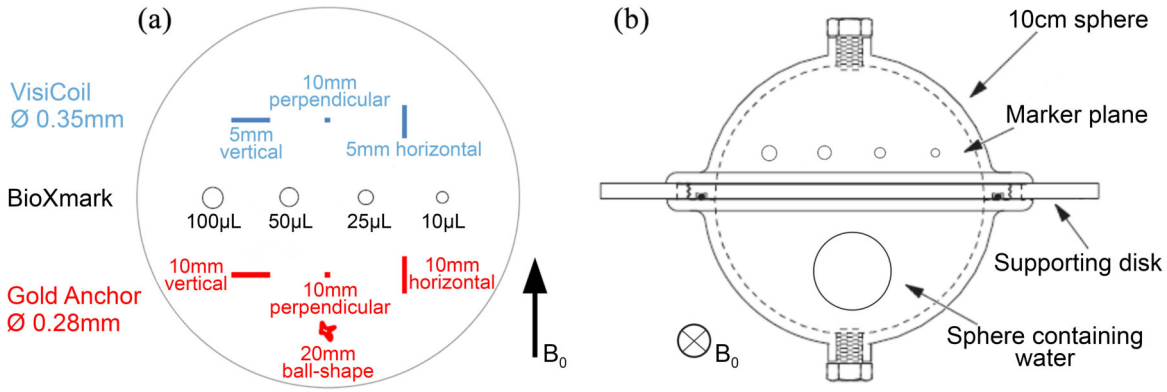

Figure 3.2: *(a)* Schematic illustration of the coronal plane of the spherical phantom containing the fiducial markers. The solid markers Gold Anchor™ and VisiCoil™ were differently oriented in respect to the static magnetic field B_0 in order to account for directional dependencies. One Gold Anchor™ was additionally placed in a ball-shaped form as often applied in clinical practice. The liquid marker BioXmark® was injected as spheres in four different volumes (10 µL, 25 µL, 50 µL and 100 µL). *(b)* Schematic illustration of the transverse view of the spherical phantom with the water sphere placed in the lower hemisphere. During MRI the phantom was aligned so the B_0 was in parallel with the marker plane and perpendicular to the transverse plane.

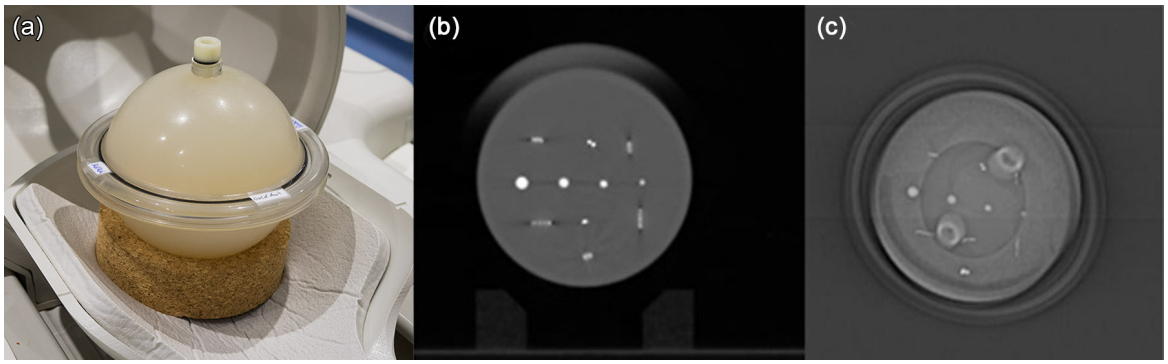

Figure 3.3: *(a)* Spherical gel phantom positioned on a cork stand for stability in the 8-channel head coil used for MRI. *(b)* Exemplary CT slice and *(c)* kV X-ray image of phantom showing all eleven implanted fiducial markers clearly visible in these two imaging modalities. The different orthogonal orientation of the solid markers can be appreciated.

a non-signal producing urethane phantom (Magpham SMR 140 phantom, The Phantom Laboratory, Salem, USA) composed of two hemispherical shells with an inner diameter of 10 cm. The spherical geometry was chosen in accordance to the recommendation by the AAPM Nuclear Magnetic Resonance Task Group No. 6 (Och *et al.*, 1992) to reduce the effects of the phantom on the static magnetic field homogeneity of the MRI scanner.

In the lower hemisphere of the phantom a polyethylene sphere with a diameter of 35 mm filled with Milli-Q water was placed. The water sphere acted as reference value for quantification of relative proton density, since no literature value of the relative proton density of pancreas tissue was available. The lower hemisphere was then fully filled with the prepared gel. The upper hemisphere was initially only filled to 75 %. Furthermore, a petri dish with a diameter of 10 cm was filled with the gel matrix up to a height of 1 cm which was allowed to set at 5 ℃ for 1 h. In the petri dish the fiducial markers were subsequently placed into the intended locations and orientations, as shown in Figure 3.2 (a). Thereafter, gel was added to the petri dish to cover all markers. Once fully solidified, the insert containing the fiducial markers were removed from the petri dish using a scalpel and transferred to the 75 % filled upper hemisphere, where additional gel was added to fully fill the hemisphere. Finally, the two hemispheres were tightly closed and the phantom was stored at 5 ℃ until use. Before any measurement, the phantom was allowed to set at room temperature for at least 10 h.

3.1.3 Investigated liquid and solid fiducial markers

The phantom was equipped with the liquid fiducial marker BioXmark® as well as two clinically used types of solid gold fiducial markers, Gold Anchor™ (Naslund Medical AB, Huddinge, Sweden) and VisiCoil™ (IBA Dosimetry, Schwarzenbruck, Germany). BioXmark® is a three-component biocompatible liquid fiducial marker, consisting of sucrose acetate isobutyrate (SAIB), organo-iodinated SAIB and ethanol. After injection in soft tissue, ethanol diffuses out of the marker, leading to an increase in viscosity. The marker comes enclosed in vials of 1 mL volume, allowing in principle for an adaption of marker size up to 1 mL depending on the injection site and the proposed imaging protocol. Due to the low initial viscosity, the marker is suitable for minimal invasive EUS guided injection using thin needles ($\leq$ 25 G). Four approximately spherical volumes of BioXmark® (10 µL, 25 µL, 50 µL and 100 µL) were positioned in the mid-plane of the phantom (see Figure 3.2 (a)). The gelatinization of the markers was induced by injection into water filled glass vials using a thin 25 G needle and a high-precision Hamilton syringe (precision $\pm$ 1 %, Hamilton Laboratory Products, Reno, USA) prior to their placement in the phantom.

For comparison, differently sized rigid gold (> 99.9% Au, VisiCoil™) and composite metal (99.5 % Au + 0.5 % Fe, Gold Anchor™) markers were placed in the same plane as the liquid markers in three different orthogonal orientations relative to the static magnetic field to cover directional dependencies. The requirement for the rigid markers was a diameter d < 0.686 mm, so that they would fit in a 19 G needle, typically used for EUS-guided fine needle aspiration of the pancreas. Four Gold Anchor™ (three d = 0.28 mm and l = 10 mm;

Figure 3.4: *(a)* Image of the tested liquid fiducial marker BioXmark® as is received in 1 mL vials (courtesy of Nanovi Radiotherapy A/S, Lyngby, Denmark). *(b)* Schematic illustration the solid Gold Anchor™ fiducial marker in linear and folded shape, which is facilitated by its segmented structure (courtesy of Naslund Medical AB, Huddinge, Sweden). *(c)* Schematic illustration the solid VisiCoil™ fiducial marker which is flexible through its helical design (courtesy of IBA Dosimetry, Schwarzenbruck, Germany).

one d = 0.28 mm and l = 20 mm) were placed in the bottom half of the mid-plane in horizontal, perpendicular and vertical orientation in respect to the static magnetic field as well as one marker in a folded ball shape, as clinically performed. Three VisiCoil™ (two d = 0.35 mm and l = 5 mm; one d = 0.35 mm and l = 10 mm) were placed in the upper half of the mid-plane in horizontal, perpendicular and vertical orientation.

3.2 Visibility and artefacts of fiducial markers in phantom at 3T MRI

Since in MRI a vast amount of contrasts can be created by the adaption of multiple sequence parameters, the typical visibility scoring found in literature is a subjective analysis by a limited amount of observers and is only valid for comparable MRI sequences. In the following chapter the aim was to provide a quantitative, pulse sequence-independent assessment of the visibility and artefacts by the tested markers in MRI. This approach was based on the method proposed by Gurney-Champion *et al.* (2015), which was extended for the purpose of including the liquid marker. In this approach the idea was to investigate the source of the markers visibility and artefact in MRI instead of their final effect in a specific sequence. For the solid markers this is mainly due to differences in magnetic susceptibility relative to their vicinity which reduces the local T_2^* relaxation time. This describes an enhanced spin dephasing, which in GRE sequences leads to pronounced signal voids in tissue caused by the marker. Therefore, in this work visibility of solid markers was analyzed by their induced reduction of surrounding T_2^* relaxation time. At the same time field perturbations can lead to geometric distortions in the images, where voxels affected are shifted relative to their actual position in the object. Artefacts caused by both solid and liquid markers will therefore be analyzed by the increase in static magnetic field inhomogeneity (ΔB_0). In case of the liquid marker BioXmark®, based on its anhydrous and ferromagnetic-free composition, low signal intensity was expected in MRI independent on the effect on the local T_2^* relaxation time. Hence the visibility of the liquid marker was analyzed by its reduction of relative water proton density ρ(H). Since visibility of an object in any imaging modality ultimately is a combination of its magnitude in contrast to the surrounding tissue and its visualized size, both visibility and artefact were separately evaluated in terms of size and magnitude, based on the approach proposed by Gurney-Champion *et al.* (2015).

3.2.1 Quantitative evaluation of marker visibility and artefacts

MRI acquisition

As described in section 3.1.1 the phantom was scanned with a 3.0 T Philips Ingenuity TF PET / MR scanner using an 8-channel head coil where special care was taken that the phantom orientation was correctly aligned with the magnetic field, as shown in Figure 3.2. All acquired data was processed with MATLAB® in order to create quantitative field maps. To facilitate a quantitative evaluation of marker visibility and artefacts based on T_2^*-, ΔB_0- and ρ(H) mapping, relaxometry was performed similarly to section 3.1.1. For T_2^*- and ΔB_0 mapping a multi-echo Spoiled gradient recalled echo (SPGR) sequence was acquired at eight echo times with equidistant intervals $\Delta TE = 4.6$ ms. From the phase image, a ΔB_0 map was calculated according to equation 2.15. To correct for phase wraps in the area of high-field inhomogeneity, phase unwrapping was performed based on the algorithms by (Ghiglia and Pritt, 1989).

For evaluating the visibility of the liquid marker a ρ(H) map was created based on a multi-echo gradient and spin echo (GRaSE) sequence (Meyers *et al.*, 2015) acquired at eight echo times with equidistant intervals $\Delta TE = 16$ ms. Based on equation 2.13, ρ(H) can be deduced for every voxel by interpolation of the exponential signal decay curve to TE = 0 ms. For this approach the T_1 decay and the inhomogeneities in B_1^- have to be considered. Therefore, a T_1 map was additionally calculated with the gold standard Inversion recovery (IR) Spin echo (SE) method acquired at six different inversion times Inversion time (TI). The complex data was then fitted to a five-parameter model (Barral *et al.*, 2010) to calculate a T_1-map. Furthermore, a B_1^- map was calculated based on a dual Repetition time (TR) Gradient recalled echo (GRE) sequence. Finally, the retrieved scaling constant was normalized to the sphere containing MQ-water to gain proton density information relative to water ρ(H).

All relevant parameters of the acquired sequences can be appreciated in the supplementary Table A.2.

Analysis

The semi-manual segmentation of markers was performed with the ImageJ software tool (ImageJ 1.41n, National Institute of Health, Bethesda, Maryland, USA). Since the visibility of the investigated markers arises from their induced signal void, the potentially visible size of the solid markers was defined as the volume of short relaxation time V($T_2^* < T_{2,low}^*$). The threshold value was set three standard deviations (i.e. $3\sigma = 12.3$ ms) lower than the mean T_2^* value of the phantom material $T_{2,phan}^*$, measured in a homogeneous slice outside the marker plane. The threshold value of 3σ was chosen in order to ensure that under the assumption of a Gaussian distribution, with 99.7 % confidence the phantom material is not falsely contributing to the segmented marker volume. A region of interest was defined around the respective marker and visually inspected for potential air inclusions. In the occurrence of the latter the segmented volume was manually corrected, which was necessary for five markers (vertical VisiCoil™, 25 µL BioXmark®, 100 µL BioXmark®, perpendicular GoldAnchor™, ball shaped GoldAnchor™). The potential magnitude of visibility was defined as the maximum relative reduction of T_2^* in the volume affected by the marker

$$M_{T_2^*} = \frac{T_{2,phan}^* - T_{2,min}^*}{T_{2,phan}^*}, \tag{3.1}$$

where $T_{2,min}^*$ is the lowest measured value within the inner fence of the segmented T_2^* dataset

$$T_{2,min}^* = min\left[Q_1 - 1.5 \cdot (Q_3 - Q_1); Q_3 + 1.5 \cdot (Q_3 - Q_1)\right], \tag{3.2}$$

to account for possible outliers. Here, Q_1 and Q_3 denote the first and third quartile of the ranked data. In correspondence to this approach the visibility analysis of the liquid marker based on ρ(H) was performed. First, a volume of low ρ(H) was determined with a threshold value lower than 3σ from the mean proton density value of the phantom material $\rho(\mathrm{H})_{phan}$ (i.e. 6 %) as a measure of potentially visible size, of which finally the relative reduction in ρ(H) was evaluated according to

$$M_{\rho(\mathrm{H})} = \frac{\rho(\mathrm{H})_{phan} - \rho(\mathrm{H})_{min}}{\rho(\mathrm{H})_{phan}}. \tag{3.3}$$

Here again $\rho(\mathrm{H})_{min}$ represents the lowest measured value within the inner fence of the

segmented ρ(H) dataset

$$\rho(\mathrm{H})_{min} = min\left[Q_1 - 1.5 \cdot (Q_3 - Q_1); Q_3 + 1.5 \cdot (Q_3 - Q_1)\right], \tag{3.4}$$

to account for outliers.

Since artefacts can arise from field inhomogeneities, the size of potential artefacts was defined as the volume of high field inhomogeneity V($|\Delta B_{0,marker}| > \Delta B_{0,high}$). The absolute value of $\Delta B_{0,marker}$ had to be considered since both the increase as well as the decrease in B_0 contributes to artefacts. In order to eliminate marker unrelated low-frequency shifts, the ΔB_0 map was subtracted by a Gaussian-filtered map (with a radius of 8 pixels). The threshold value $\Delta B_{0,high}$ was again defined as a 3σ deviation from the phantom material (i.e. 4 Hz). As a measure of magnitude of artefacts, the maximum difference in local magnetic field $\Delta_{max}B_0 = \Delta B_{0,max} - \Delta B_{0,min}$ within the volume of the respective marker was evaluated.

Results

The quantitative maps, resulting from the performed relaxometry, are depicted in Figure 3.5. For quantification of visibility of the solid and liquid markers, the T_2^* map (Fig. 3.5 (a)) and the ρ(H) map (Fig. 3.5 (b)) were used, respectively. The ΔB_0 map (Fig. 3.5 (c)) was used for quantification of artefacts, where the segmentation of all markers is shown in Figure 3.5 (d). The relationship between the potentially visible size and the potential size of artefact

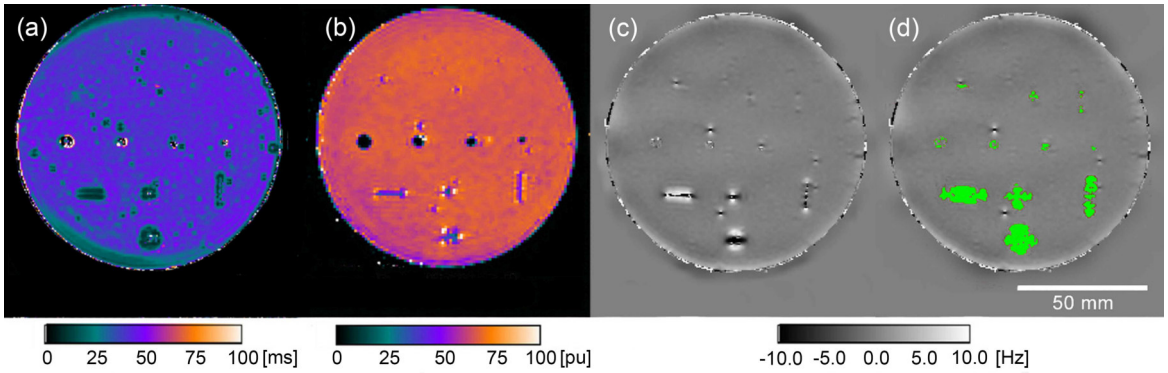

Figure 3.5: Coronal plane of the phantom including the fiducial markers showing *(a)* the T_2^* map, *(b)* the ρ(H) map in percent units [pu] relative to ρ(H) of water, *(c)* the Gaussian-filter subtracted ΔB_0-map and *(d)* the Gaussian-filter subtracted ΔB_0-map overlaid with the segmentation (green) resulting from a threshold of 4 Hz. The segmentation was corrected in the presence of artefacts due to air inclusions.

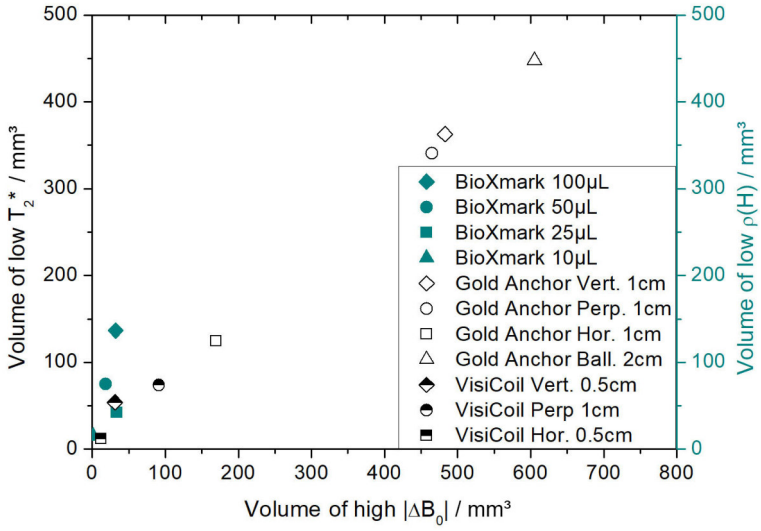

Figure 3.6: Trade-off between the volume with low transverse relaxation time T_2^* (left axis) and low relative proton density ρ(H) (right axis) as a measure of potentially visible size and the volume with high ΔB_0 as a measure of potential size of artefact.
Abbreviation: Verti. = Vertical; Hor. = Horizontal; Perp. = Perpendicular

for all markers included in the study is illustrated in Figure 3.6. Gold Anchor™ markers were found to have the largest volume of potential visibility due to the included ferric component (0.5 %). Simultaneously, Gold Anchor™ markers induced the largest volume of field inhomogeneity. As can be seen in Figure 3.6, a difference in affected volume (factor 2.8) was observed between identical Gold Anchor™ when oriented horizontally with respect to the static magnetic field or perpendicular, respectively. A similar behavior was observed for VisiCoil™, however, with a smaller absolute size of affected volume in both visibility and artefact due to the absence of iron. For the solid markers a linear dependency between potentially visible size and field inhomogeneity was observed (coefficient of determination: $R^2 = 0.996$, Spearmann correlation coefficient: $R_S = 0.99$).

The liquid marker showed only a weak correlation between potentially visible size and volume of field inhomogeneity ($R_S = 0.4$). The introduced volume of high ΔB_0 did not increase directly proportional to the potentially visible size. In the ΔB_0-map (Figure 3.5 (c)), voxels affected by high ΔB_0 were found heterogeneously spread in the direct interface between marker and phantom gel matrix. BioXmark® marker with a volume of 50 µL showed a visible size comparable to the 1 cm long solid marker VisiCoil™ in perpendicular orientation, while only showing 20 % of the affected volume in ΔB_0. The largest liquid marker (100 µL) induced a signal void comparable to the potential size of the horizontally-oriented

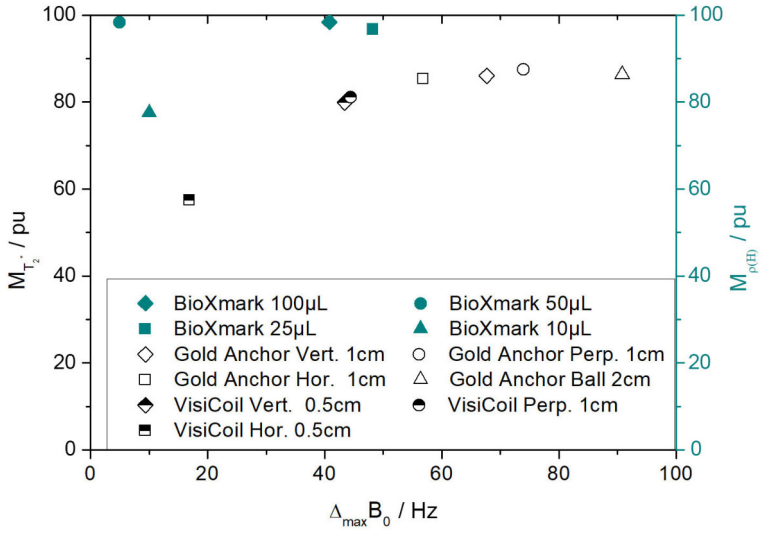

Figure 3.7: Trade-off between maximum reduction of T_2^* (left axis) and ρ(H) (right axis) in percent units [pu] as a measure of potential magnitude of visibility and the maximum magnetic field inhomogeneity introduced by the marker as a measure of magnitude of potential artefacts.
Abbreviation: Verti. = Vertical; Hor. = Horizontal; Perp. = Perpendicular

1 cm long Gold Anchor™ marker at only 19 % of the respective volume affected by artefacts. The potential magnitude of visibility and artefact (Figure 3.7) showed a non-linear correlation ($R^2 = 0.992$, $R_S = 0.964$) for the solid markers. Within the group of solid markers, Gold Anchor™ marker were found to produce the largest magnitude of visibility as well as overall the most pronounced tendency towards artefacts (91 Hz). BioXmark® marker did not show a correlation between magnitude in visibility and artefact ($R_S = 0.0$). The liquid marker with a volume of 50 µL showed to induce a high magnitude of visibility, with a relative signal reduction factor of 0.98, at the smallest potential artefact (5.0 Hz).

3.2.2 Qualitative evaluation of marker visibility

The interpretation of a low ρ(H) as the source of visibility of the liquid marker led to the expectation that the liquid marker should be similarly visible in all MRI sequences if resolution is constant, since ρ(H) affects all MRI sequences as a scaling factor in the same way. In order to validate this hypothesis, the phantom was first scanned with sequences typically used in our institution for patients with PDAC (see supplementary Table A.3 (a-d)). Additionally, in order to visualize the visibility characteristics of the fiducial markers, a SPGR sequence at two TE (e, f) was acquired as well as a SE sequence at two TE (g, h). The apparent size of the fiducial marker was then determined in sequences (e-h) to

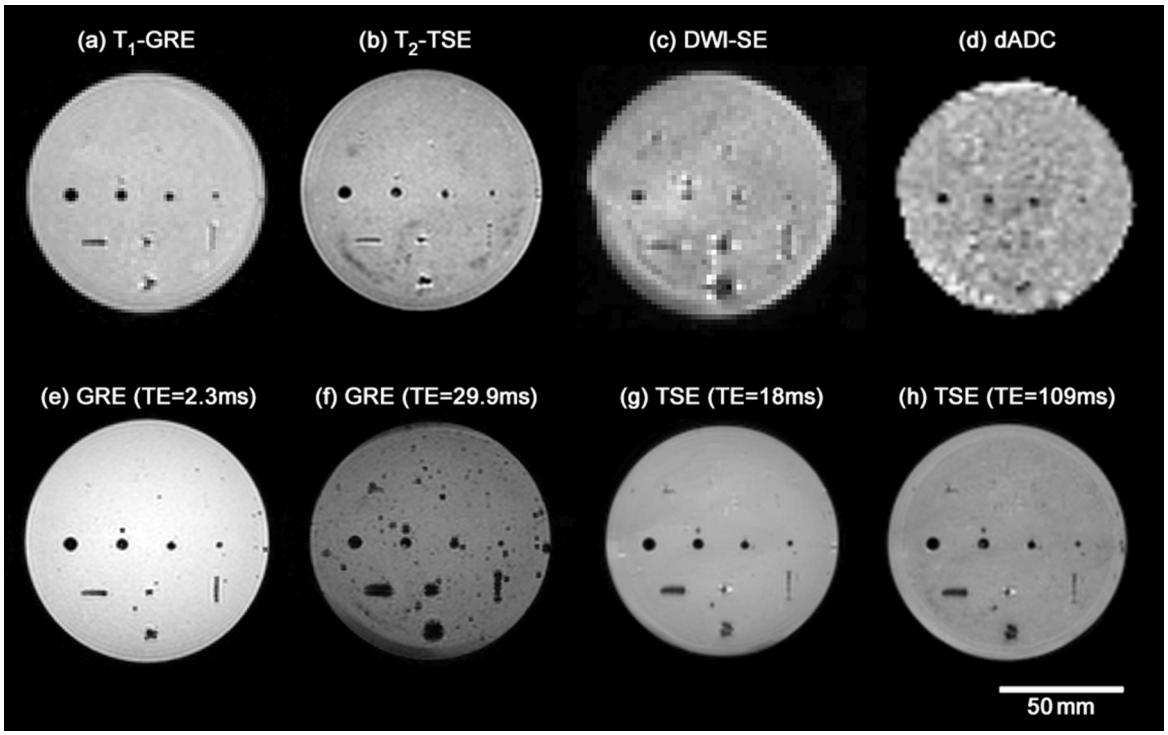

Figure 3.8: Qualitative assessment of the fiducial marker in different MRI sequences. *(a)* T_1-weighted spoiled GRE, *(b)* T_2-weighted SE, *(c)* Diffusion-weighted SE, *(d)* Apparent diffusion coeffcient map in M-gradient direction calculated from DWI image in *(c)* , *(e-f)* GRE with TE = 2.3 ms *(e)* and TE = 29 ms *(f)* , *(g-h)* SE with TE = 18 ms *(g)* and TE = 109 ms *(h)*

validate the hypothesis of the different sources of visibility for the solid and liquid markers. The size of markers was evaluated by setting a threshold value of 3σ from the mean signal of the phantom material in the respective sequence. Signal values below this threshold were considered as affected by the markers. Segmentation was manually corrected in the occurrence of air inclusions close to markers. Finally, for every type of marker, the relative standard deviation (RSD) of the visible size in the GRE sequences (e, f) was determined as a measure of change in visibility at different TE.

All markers caused signal voids in the utilized sequences. An evaluation of their respective visible size in GRE and SE sequences at different TE is shown in Fig. 3.9. Gold Anchor™ markers were especially visible in sequences that are affected by field inhomogeneity effects (i.e. GRE and DWI), in which VisiCoil™ markers were also best detectable. There, at long TE (Fig. 3.8) the solid markers appeared larger ($\mathrm{RSD}_{\mathrm{GoldAnchor}} = 70.5\,\%$, $\mathrm{RSD}_{\mathrm{VisiCoil}} = 74.0\,\%$). In SE sequences the visibility of the solid markers was smaller and relatively constant in between different TE. In particular VisiCoil™ markers were hard to

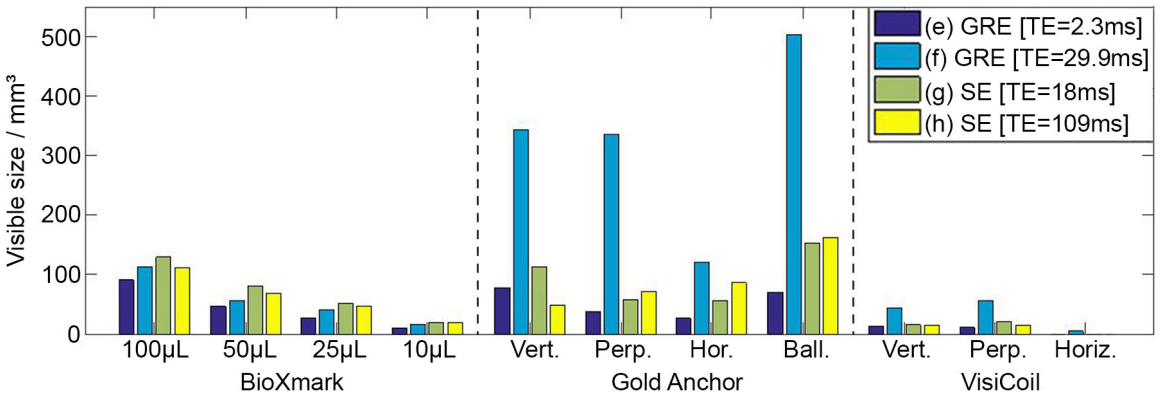

Figure 3.9: Evaluation of visible size for all 11 markers in the 4 sequences (e-h) shown in Figure 3.8 used for qualitative assessment.
Abbreviation: Vert. = Vertical; Hor. = Horizontal; Perp. = Perpendicular.

detect and Gold Anchor™ marker were much less pronounced. BioXmark® caused signal voids with comparable size at different TE ($RSD_{BioXmark} = 16.7\,\%$). This is in agreement with the understanding that the solid markers are primarily visible due to their effect on T_2^* of their surrounding tissue, while BioXmark® causes signal voids due to the lack of water protons, equally affecting all MRI sequences.

3.2.3 Discussion

In accordance with literature, the solid fiducial markers were found to cause variations in the surrounding static magnetic field due to their magnetic susceptibility difference relative to the phantom material. This was most prominent in pulse sequences that are strongly affected by inhomogeneities in the static magnetic field (e.g. GRE or DWI). On the contrary, the liquid marker did not substantially affect the surrounding tissue through an increase in field inhomogeneity, but primarily caused signal voids through the lack of water protons. The analysis based on the reduction of T_2^* relaxation time, as proposed by Gurney-Champion *et al.* (2015), led to an underestimation of the potential visibility of BioXmark®. The approach of quantifying visibility through a reduction of ρ(H) on the other hand did not cope with the potential visibility of the solid markers. This was due to their effect on the T_2^* relaxation of the surrounding tissue, leading especially in GRE sequences to a visibility larger than their physical size. Hence, for comparison the visibility of the fiducial liquid and solid markers were analyzed in their respective nature (ρ(H) for the liquid markers, T_2^* for the solid markers).

Based on the results presented, the two factors that affected the visibility of the BioXmark® marker were the resolution of the MRI acquisition and sufficient signal from the surrounding tissue as contrast to the signal void induced by the markers. When the resolution was higher than the size of the injected marker, the resulting signal voids were found to be independent of the pulse sequence parameters and were easily distinguished with a signal reduction factor of up to 0.98 (see supplementary section A.1 for evaluation of visibility in respect to resolution). Marker visibility in different pulse sequences would facilitate a co-registration of a multi-parametric MRI acquisition with CT (Fernandes *et al.*, 2017). Due to the fact that the source of visibility in BioXmark® lies in the reduction of ρ(H), which is a property directly affecting all MR sequences, no tuning of MR parameters is necessary to optimize the marker's visible contrast. However, in a more heterogeneous structure like pancreatic tissue, the size of BioXmark® of at least twice the image resolution is advised to achieve an appropriate visibility that is not hampered by partial volume effects.

Furthermore, the size of high ΔB_0, as a measure of size of artefacts, was found to be 81 % smaller around BioXmark® than the size of high ΔB_0 around the implanted Gold Anchor™ and smaller or comparable than the non-ferromagnetic VisiCoil™. The inhomogeneities were heterogeneously spread at the interface between marker and gel. In case of the 25 μL and 100 μL BioXmark®, artefacts due to small air inclusions could not be fully corrected. This indicates that the marker itself does not induce the measured field inhomogeneities, but rather small remaining air gaps from the manufacturing process of the phantom.

As found in Gurney-Champion *et al.* (2015) for the solid markers, the potential to be visible and cause artefacts strongly correlated ($R_S = 1.0$), i.e. better visibility comes at the cost of a stronger tendency towards artefacts. Both solid markers showed a linear dependency ($R^2 = 0.996$) between visible size and size of artefacts. This differs slightly from the results found in Gurney-Champion *et al.* (2015) where a non-linear dependency was reported. This difference could potentially result from differently defined thresholds in the analysis, a different acquired resolution or the smaller number of samples of solid markers in our study.

The orientation of the solid markers with respect to the static magnetic field affected their potential visibility and artefacts, in agreement with the findings in Gurney-Champion *et al.* (2015). Markers implanted horizontally showed both smaller visibility and artefacts. The perpendicular and vertical orientation induced effects of similar size. Since in the clinical case the orientation is random, we expect an average of the investigated scenarios. Gold Anchor™ markers are typically implanted in a folded ball-shaped form. The 2 cm long marker

implanted in a ball-shaped form had an effect of approximately twice (factor 1.88) the size of the mean of the horizontally and vertical orientated 1 cm long markers. In an ideal case, BioXmark® forms a spherical shape after injection, which makes the orientation relative to the static magnetic field arbitrary.

In this study, the potential magnitude of visibility was defined as the maximum relative reduction in T_2^* or ρ(H) to describe the signal voids of the markers in their respective nature. The analysis showed a result for the solid markers comparable to Gurney-Champion *et al.* (2015). We found a non-linear correlation ($R^2 = 0.992$, $R_S = 0.964$) between the potential magnitude of visibility and artefact, approaching a maximum reduction factor in T_2^* of 0.87 at increasing magnetic field inhomogeneities up to 91 Hz, where Gold Anchors™ induced the strongest field inhomogeneity. With exception of the 25 μL BioXmark® marker and the horizontally aligned VisiCoil™, BioXmark® markers induced the lowest field inhomogeneity. Again, BioXmark® showed a different dependency where the magnitude of visibility was not correlated ($R_S = 0.0$) to the magnitude in field inhomogeneity. At a high ρ(H) reduction factor of 0.98, the 50 μL liquid marker only induced low field inhomogeneities of maximum 5 Hz. The fact that the magnitude in artefact is not correlated to the size of the liquid marker indicates that the measured field inhomogeneity (especially from the 25 μL and 100 μL sized marker) is due to remaining air in the interface between marker and phantom material.

One should note that both the measured T_2^*- as well as ρ(H) reduction are dependent on the acquired voxel size. Due to a stronger partial volume effect at a lower resolution the magnitude of the reduction would be underestimated, while the size of the affected volume is overestimated. This holds true up to a minimum resolution, where the marker cannot be identified anymore and both size and magnitude would be underestimated (as shown in the supplementary A.1). On the other hand the T_2^*-reduction is also potentially overestimated at a lower resolution due to stronger dephasing within lager voxel.

One should also note that the threshold values chosen for differentiation of markers and phantom material affect the outcome of the analysis. In this study a 3σ threshold was consistently used for segmentation. In the case of the ΔB_0-map this led to a threshold of 4 Hz. It has to be noted that when e.g. using a commonly implemented DWI sequence with an in-plane resolution of 3×3 mm² at a pixel bandwidth of 30 Hz, field inhomogeneities of 4 Hz would only led to a voxel shift of approximately 0.4 mm. For most clinically used sequences this level of field inhomogeneity would have a negligible effect. Possible signal alterations due to eddy currents induced in the solid markers were not considered. Given the size and

composition of fiducial markers tested, this effect is expected to be secondary relative to the susceptibility induced T_2^*-reduction effect (Graf *et al.*, 2006; Vashaee *et al.*, 2014; Gurney-Champion *et al.*, 2016). Eddy currents resulting from changing RF-field or image gradients are, however, very likely the main source of the Gold Anchor™ signal voids observed in SE sequences (as seen in Figure 3.8). This also applies to the ρ(H)-map (Figure 3.5 (b)), where Gold Anchor™ markers appear larger than their physical size.

The markers were selected as they can be implanted using a 19 – 22 G needle, typically used for EUS-guided fine needle aspiration of the pancreas. All three included markers have been originally designed for X-ray based image guidance, but possess visibility in MRI due to their physicochemical properties and their effect on the magnetic field in the surrounding tissue. Several other commercially available solid markers such as FusionCoil™ and PolyMark™ have been developed for enhanced MRI-compatibility. Since these markers require 18-gauge needles for implantation, their suitability for use in pancreatic adenocarcinoma is compromised by the fact that they need to be inserted via the EUS-guided fine needle aspiration technique, requiring at least 19 G needles. Consequently, FusionCoil™ and PolyMark™ were not included in this study. The use of other liquid fiducial markers for CT and MR imaging has been reported in the literature. TraceIT® (Augmenix Inc, Waltham, MA), a hydrogel-based marker has been reported for use in gynaecological (Bair *et al.*, 2015), bladder (Chamie *et al.*, 2014) and oesophageal cancer (Machiels *et al.*, 2015) with sufficient visibility in both imaging modalities. In T_2-w MRI this marker was in fact visible as hyperintensity. However, due to their low X-ray attenuation, their visibility in CBCT was poor with only 22 % markers visible 13.5 days after initial injection (Machiels *et al.*, 2015). Consequently rather large volumes > 400 μL had to be injected for sufficient visibility, preventing the formation of small discrete markers. Furthermore, long-term stability, which is crucial for fractionated radiotherapy of several weeks, has been reported to be limited with only 11 % of the injected markers remaining visible in CBCT during the course of RT(Machiels *et al.*, 2015). Terry *et al.* (2014) reported the *in vitro* use of aqueous solutions of iopamidol for CT and MR imaging and concluded that a 10 % aqueous solution proved to be optimal with respect to visibility and low degree of artefacts. However, *in vivo* use of such a system for tissue injection is limited due to biological washout following injection, resulting in unspecific tissue marking.

It should be noted that due to the design of the phantom, our study only analyzed the MRI characteristics of the markers in pancreatic-like tissue at 3 T. Based on our correlation

analysis between the potential to be visible and cause artefacts, and given that susceptibility induced B_0 inhomogeneities decrease at lower magnetic field strengths (Soher *et al.*, 2007), we expect that solid markers would induce both smaller artefacts and visibility at 1.5 T and even more so at 0.35 T, commonly used for MR-Linac systems. BioXmark® however, should give similar results based on its proton density effect. Furthermore, the results based on the reduction of ρ(H) can only be limitedly transferred to the clinical case. The constructed gel phantom was designed to mimic the relaxation properties of pancreatic tissue, not to accurately resemble its ρ(H) value. No literature was found that accurately describes ρ(H) of pancreatic tissue *in vivo* relative to water. An investigation of the markers behavior in real pancreatic tissue is therefore mandatory.

3.3 Detectability of liquid fiducial marker in *ex vivo* tumorous pancreas tissue

Concluding section 3.2 the visibility of the liquid marker is induced by the low water proton density in the volume the marker is occupying. This volume effect makes the visibility of the marker strongly depending on its injection behavior. In section 3.2, the liquid markers were injected into water to facilitate gelatinization prior to placement into the phantom, leading to sphere like shapes. *In vivo*, however, a spherical injection is not ensured and will likely depended on its cellular structure. Shortly after concluding the prior presented phantom study, De Roover *et al.* (2018) found the liquid marker to be hypointense in T_1-weighted but iso-intense and consequently non-visible in prostatic tissue in T_2-weighted images at 1.5 T. This finding is in part contradictory to those of our study. Since in MR-guided RT and organ at risk delineation is often performed on or supported by T_2-weighted images, the detectability of fiducial markers in these sequences is of particular interest. Since a CE certification for the use of BioXmark® in abdominal patients was at the time of this study still pending, an *ex vivo* investigation of the markers behavior in tumorous pancreas tissue was the closest achievable to a clinical scenario. This study is described in the following chapter.

3.3.1 Material and methods

Three patients (two males, age 69 and 72; one female, age 68), suspected to have an adenocarcinoma of the pancreatic head and scheduled for primary pancreaticoduodenectomy, provided informed written consent for injection of the liquid fiducial marker into the resection specimen and for subsequent X-ray, CT and MR imaging thereof. Immediately after resection, the resection specimen was transported to the Department of Pathology of the University Hospital Carl Gustav Carus for immediate biopsy selection for frozen section analysis. During transport the specimen was stored in a container with ice to prevent enzymatic degradation. Thereafter, the injection of the markers and imaging of the resection specimen were performed within the next 2 hours, while still being on ice. In order to test the stability of the marker after fixation in formaldehyde, the complete scan protocol was repeated for one of the three resection specimens after fixation in formaldehyde for 24 hours. Surgical clips or sutures placed into the resection specimen during the surgical resection were not removed and remained present during marker injection and subsequent imaging. The study was approved by the local Ethics Committee of the Faculty of Medicine and University Hospital Carl Gustav Carus of the Technische Universität Dresden (EK-534122015).

In each specimen several liquid markers (5 – 6) of various volumes (20/25 μL, 50/60 μL, 100 μL) were injected at a depth of 1 cm – 2 cm directly adjacent to the tumour boundaries approximately 30 min after surgical resection. Moreover, three different needle sizes (18 G, 22 G, 25 G) were used during the injection into the three specimens, respectively, to test the injection behavior depending on needle size. For this, the needles were attached to a unit dose injector (MicroDose™, Vlow Medical B.V., Eindhoven, The Netherlands) for accurate and reproducible injection. The injection was performed under kV X-ray guidance to facilitate the subsequent differentiation of injected markers and surgical clips or sutures.

While in two resection specimens (specimen volume 191.0 cm^3 and 334.3 cm^3) six markers were injected, in one specimen only five markers were injected due to a relatively small size of the specimen (specimen volume 154.2 cm^3). Furthermore, for two specimens a unit dose injector was used which allowed smallest injection volumes in steps of 25 μL, while for the other specimen only a unit dose injector was available which allowed smallest injection volumes in steps of 20 μL. This led to a slightly different size and number of injected markers throughout the used resection specimens.

3.3.2 Image acquisition

Marker injection was performed under kV X-ray guidance. This enabled an injection with sufficient distance to surgical clips or sutures as well as facilitated the discrimination of markers and clips in subsequently acquired CT images (Siemens SOMATOM Definition AS, Siemens Healthineers, Erlangen, Germany). In order to test the MRI visibility of the marker *ex vivo*, pulse sequences were utilized which are also commonly used in our clinic for patients with pancreatic adenorcarcinoma. Coronal MR images were acquired with a 32-channel SENSE Torso/Cardiac coil (3.0 T Philips Ingenuity TF PET/MR scanner, Philips Healthcare, Eindhoven, The Netherlands) acquiring a T_1-weighted spoiled gradient echo sequence (GRE) and a T_2-weighted turbo spin echo (TSE) sequence. Both CT and MRI scans were performed with the specimen still placed on ice.

3.3.3 Analysis

The CT images were first rigidly registered onto the MR images taking into account the specimen contour. The markers were then segmented on the CT images as hyperintense structures with the open source software 3D Slicer (Pieper *et al.*, 2004) by threshold segmentation such that the lower threshold (i.e. 129.3 HU) was 3σ higher than the mean signal intensity of the pancreatic tissue (see Figure 3.10 (c)). In order to correctly assign the respective marker and to prevent erroneously segmenting surgical clips or sutures instead of

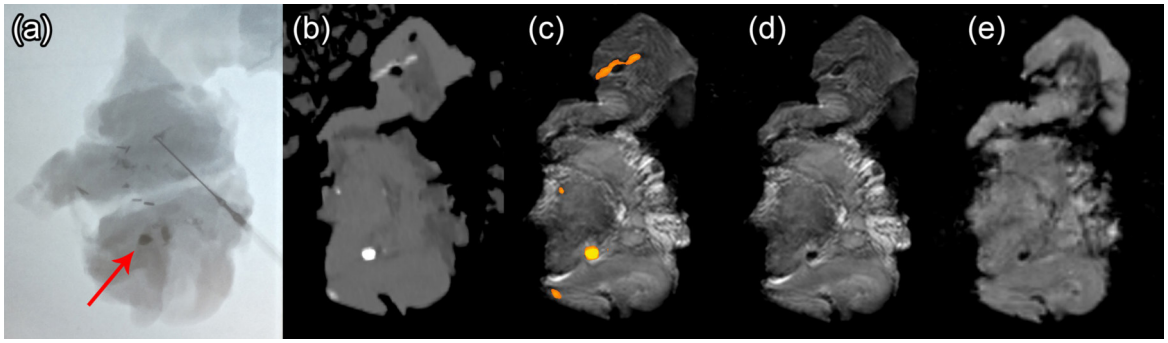

Figure 3.10: *(a)* kV X-ray of a resection specimen during marker injection in which the needle is visible on the right half of the image, as well as several surgical clips close to the marker injections of which a 100 µL marker is marked with a red arrow. *(b-e)* Coronal slice where the in (a) marked 100 µL marker is visible on CT (b) and T_2-weighted turbo spin echo (TSE) MRI superimposed with the threshold based orange-yellow CT segmentation (c), native T_2-weighted TSE MRI (d) and T_1-weighted gradient echo (GRE) MRI (e). The injected 100 µL fiducial marker is depicted as hyperintensity on CT and as signal void on T_2- (d) and T_1-weighted (e) MRI

liquid fiducial markers, the X-ray images taken during injection were used as a visual aid. MRI visibility of the liquid marker was approved if a hypointense structure was visible on MRI enclosed by the registered CT segmentation, following the results in section 3.2.1.

In order to assess the geometrical stability of the fiducial marker after fixation of the resection specimen in formaldehyde, for one resection specimen the segmentation procedure was repeated on the CT scan obtained after fixation for 24 hours. The segmented volumes of the respective markers on CT before and after fixation were compared to deduce a possible volume decrease.

3.3.4 Results

Figure 3.11 shows (from left to right) exemplary slices of the resection specimens on CT, T_1- and T_2-weighted MRI from all three patients included in this study (top to down). As can be

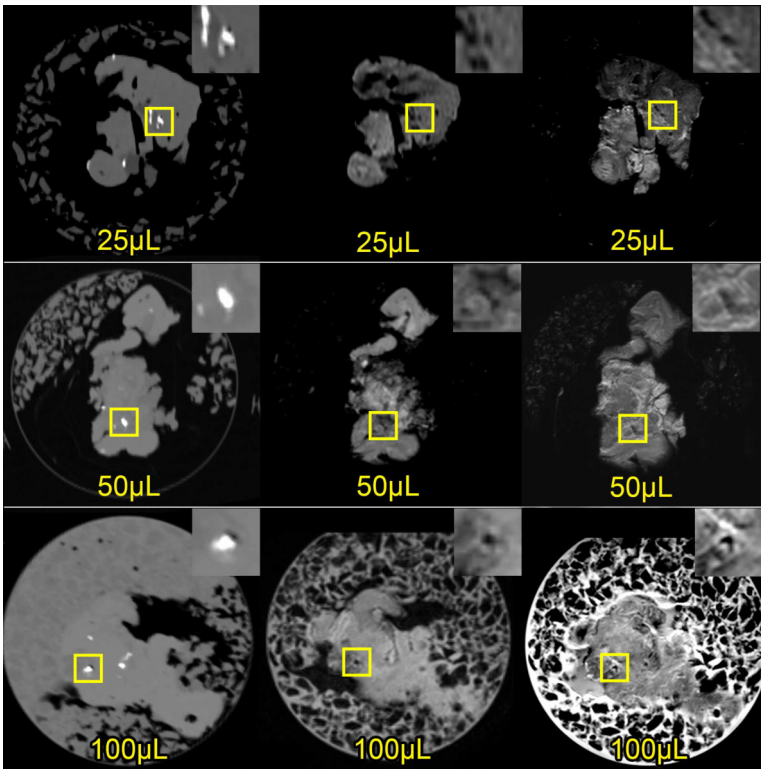

Figure 3.11: Exemplary coronal slice of all three resection specimens on CT [left], T_1-weighted gradient echo (GRE) MRI [middle] and T_2-weighted turbo spin echo (TSE) MRI [right]. In each of the three specimens one marker of different size (25 µL, 50 µL, 100 µL) was highlighted with a yellow square in the respective imaging modality. Markers are visible as hyperintensity on CT and as hypointensity on both T_1- and T_2-weighted MRI. On the top right of each segment a close-up view of the yellow squared region of interest is shown for clear visualization of the marker

appreciated, the liquid fiducial marker is detectable on CT as hyperintense structure and as hypointense structure on both T_1- and T_2-weighted MRI, respectively. Markers of all sizes (20 µL – 100 µL) tested in this study could be detected with the clinically used sequences. Noteworthy, CT revealed that injection generally resulted in a non-spherical marker, making MR detectability dependent on slice orientation and voxel size. Moreover, a diffuse injection or injection too close to the surface hampered MR detectability, leading to 4 of 17 markers being non-detectable on MRI. CT and MR images of all 17 marker injection sites can be found in the supplemental material Fig. A.4.

After 24 h fixation in formaldehyde all six markers in the investigated resection specimen were still visible on CT (see Figure 3.12 for a coronal maximum intensity projection) and MRI (Figure 3.13), and geometrically stable. Overall, the volume decrease was 6.6 % ± 13.0 %, which was expected due to the efflux of ethanol within the first 2 h after injection, as described in literature (Scherman Rydhög *et al.*, 2016). Only one 60 µL marker was partially washed out of the specimen. As was detected on the CT images, this marker was initially injected too close to the specimen surface, leading to its partial protrusion out of the specimen.

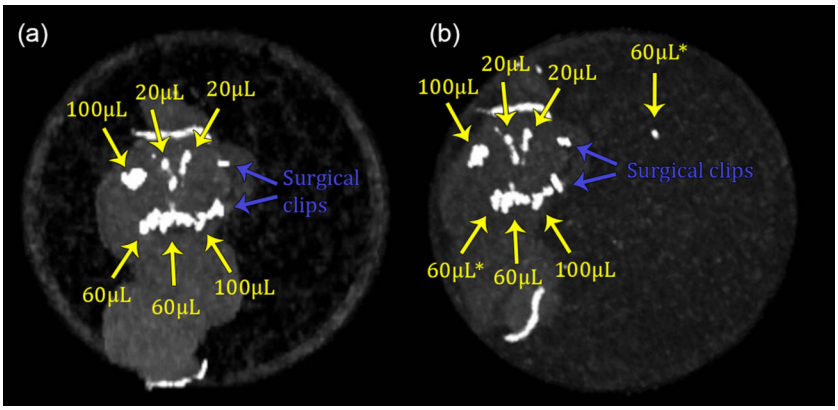

Figure 3.12: Maximum intensity projection of the resection specimen scanned with CT before *(a)* and after *(b)* fixation in formaldehyde. All six injected markers were stable in their size and position. It can be appreciated that after fixation an additional hyperintense structure was found in the top right corner of the container filled with formaldehyde. This corresponds to a partially washed out 60 µL marker (marked with an asterix).

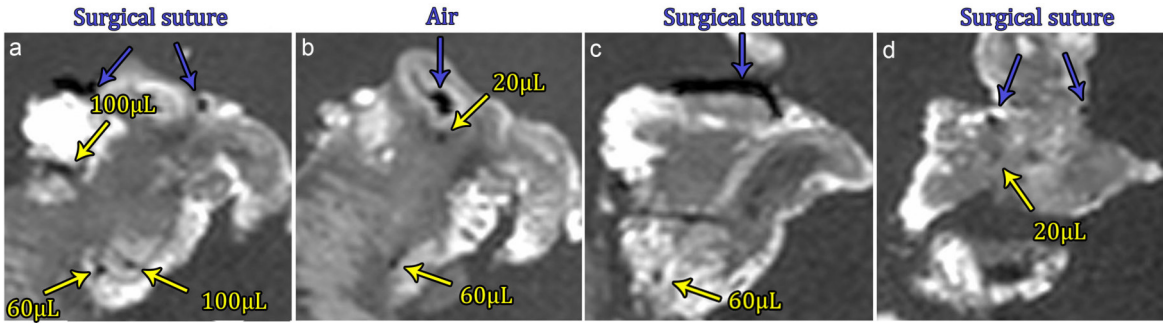

Figure 3.13: Four representative T_1-weighted MRI slices of a pancreatic cancer resection specimen fixated in formaldehyde showing all six injected markers. Remaining hypointensities caused by a surgical suture and air cavities are also visible.

3.3.5 Discussion

While marker detectability on CT imaging was found to be satisfactory with markers clearly depicted as hyperintense structures, on MRI the fiducial marker was difficult to identify due to signal voids from tissue heterogeneity, air cavities, surgical clips or sutures resembling fiducial markers in MRI. To distinguish fiducial marker induced signal voids from the latter, a prior registration with the CT images was necessary. Moreover, visible marker backflow was reduced using smaller needle diameters, and the marker was found geometrically stable after 24 h fixation in formaldehyde.

The marker detectability on MRI may improve using a composition with gadolinium leading to a hyperintense marker, which would facilitate its differentiation in heterogeneous tissue. This would however impair the markers transparency for proton beam irradiation due to the consequently higher *Z*number. On the other hand, for the *in-vivo* situation, the marker detectability is expected to improve since less or no hypointensities caused by air cavities and/or surgical clips are present. Conversely, since fiducial marker injection in case of PDAC is often performed into the adipose tissue in direct proximity of the tumour, marker detectability on fat-saturated MRI sequences will be hampered, as was also found in clinical practice with fiducial gold markers in our institute. After registration with the CT images of the specimen, many markers were still only poorly visible or even not visible at all on MRI. When investigating these markers on the CT images, it appeared that in these cases the injection was not spherical. Hence detectability was strongly dependent on the injected shape and the distance to the specimen surface. Nevertheless, in particular larger markers $\geq 50\,\mu$L, which formed sphere-like volumes, were visible as strong signal void on both T_1-

and T_2-weighted MRI. This is concordant to the results found in chapter 3.2.1, where the BioXmark® marker was found to be causing signal voids at 3 T independent of the contrast mechanism due to an apparent lack of water protons. In De Roover *et al.* (2018) the same marker was found to be isointense to prostatic tissue on T_2-weighted MR images at 1.5 T. These different findings may result from the lower field strength used in their study. It is more likely, however, that this effect resulted from a signal contamination caused by the phantom material in which the marker was injected. Since the ellipsoid shaped 300 µL marker analysed in the study by De Roover *et al.* (2018) showed a size in slice encoding direction that was close to the slice thickness acquired (4 mm), a partial volume effect cannot be ruled out.

When introduced into clinical practice, it is expected that the *in vivo* use of the BioXmark® will lead to more spherical and hence better detectable markers on MRI. This is due to the persisting metabolism and fast efflux of ethanol after injection. This effect is expected to be magnified by faster efflux and consequential faster gelation in warm *in vivo* tissue in comparison to the $\sim 4\,\mathrm{C}^\circ$ realized in this study due to the transport of the specimens on ice. Alongside, motion blurring will impede on the MR quality and will most likely require larger marker volumes of 50 µL – 100 µL to still be visible on MRI. These volumes should preferably be injected with a needle of at least 22 G preventing marker backflow. The marker's detectability on different anatomical imaging modalities is of great value to the field of radiation oncology. In addition, its minimal proton dose perturbations (Jølck *et al.*, 2014; Scherman Rydhög *et al.*, 2017), the chemical stability during a prolonged course of fractionated radiotherapy (Troost *et al.*, 2017) and also after fixation in formaldehyde makes the marker promising for neoadjuvant and definitive treatment concepts involving photon or proton beam therapy.

3.4 Summary

In this study, the MRI properties of the novel liquid fiducial marker BioXmark® have been investigated for the first time. A method for quantitative evaluation of MRI visibility and artefact, as proposed by Gurney-Champion *et al.* (2015), was used and extended to compare the liquid marker against the two commonly used solid markers Gold Anchor™ and VisiCoil™. In our approach, visibility of solid markers was determined based on their reduction

on local T_2^* relaxation time, while the visibility of the liquid marker was quantified as reduction of ρ(H) relative to water. The quantification of artefacts induced by both solid and liquid markers was based on the locally increased static field inhomogeneity by the markers. All fiducial markers were implanted within a gel phantom, mimicking the relaxation properties of pancreatic tissue at 3.0 T and were visible in this phantom as hypointense structures. While a strong correlation was found between visibility and artefacts of solid markers, in the case of the liquid marker no such correlation was found. The interpretation of visibility due to low ρ(H) in the liquid marker was validated by comparing the size of visibility in different sequences (SE and GRE) at different TE. The liquid marker was found to induce strong hypointensities at a level of background noise and showed a constant size in all tested sequences. This led to the conclusion, that the liquid marker's visibility is depending only on the combination of marker size and sequence resolution, when injected in MRI signal generating tissue.

Furthermore, BioXmark® was tested for the first time *ex vivo* in freshly resected pancreatic cancer specimen. While visibility in CT and kV X-ray was found to be satisfactory where all markers with a size between 20 μL – 100 μL was easily detectable, visibility in MRI was relatively poor due to the large amount of similar hypointensities due to tissue heterogeneity as well as surgical clips and sutures still present in the specimen. *In vivo* the visibility of the liquid marker is expected to increase due to the absence of air inclusions and surgical clips resembling the marker as well as due to the more spherical gelation in an environment with persisting metabolism. Conversely, marker visibility will suffer due to persisting motion *in vivo*. Considering both effects we expect a marker size of $>$ 50 μL to be necessary in order to allow MRI visibility of the liquid marker *in vivo*.

4 Geometric fidelity and accuracy of phantom target tracking with MRI

To increase the accuracy of RT for patients with moving tumors, it is of paramount importance to take intrafractional motion into account during pre-treatment image acquisition, treatment planning and dose delivery (Keall *et al.*, 2006). Respiratory motion is the predominant cause of intrafractional motion affecting all tumor sites in the thorax and abdomen (De Ruysscher *et al.*, 2015). The quantification and management of respiratory motion is therefore an essential component to improve treatment outcome through IGRT. Motion characterization through MRI, however, has to be approached with care due to the susceptibility of MRI towards geometrical distortion. Therefore, the accuracy and precision of dedicated MRI pulse sequences for motion tracking initially need to be assessed in a quality assurance (QA) procedure. For this purpose, MRI motion phantoms should be utilized to simulate reproducible motion patterns with known ground-truth trajectories, which are generally not available for patients due to day-to-day variations in patient anatomy, breathing patterns and uncertainties in patient positioning.

Historically QA in MRI has been radiology-oriented. Hence both QA protocols as well as commercially available MRI phantoms have largely been designed to evaluate the image quality of static objects (Jackson *et al.*, 2010). With the recent development and increased clinical interest in MR integrated RT systems, however, the evaluation of MR image quality of moving objects is becoming increasingly important, especially when used for organ motion characterization studies and gating or tracking purposes in RT. Consequently, several MRI motion phantoms are now commercially available.

In the following chapter, the aim is to develop a commissioning protocol for an MRI-Linac motion phantom on a diagnostic 3.0 T MR scanner, that is used for RT simulation purposes including organ motion characterization studies, and to assess the scanners 3D geometric fidelity and accuracy in dynamic target tracking. In section 4.1 the phantom is presented. Since the phantom was designed for use on an MR-Linac scanner with a lower magnetic

field, a positioning setup was designed, which considers safety regulations at higher magnetic fields and allows for a fast reproducible positioning at the 3 T MR scanner, which had previously been modified for radiotherapy compatibility (see section 4.2). Subsequently, a method was developed for an automatic quantification of 3D geometric distortion. With this tool a 3D GRE sequence, used for abdominal patients, was analyzed regarding its geometric fidelity (section 4.3). Preparatory to the motion analysis, relaxometry was performed (section 4.4.2) to assess the relaxation properties of the phantom's moving cylinder and the included target, for contrast optimization of the pulse sequences used for motion analysis. Finally, a method for automatic quantification of multi-dimensional target motion is presented in section 4.4 for the analysis of the MR scanner's accuracy in motion tracking. Both the distortion analysis as well as the motion tracking analysis are in principle applicable to other 4D-MRI motion phantoms and allow for repeated QA.

The results of this study have in part been published by Schneider *et al.* (2019a), in the report by Engler (2017) and in the bachelor thesis by Engler (2018).

4.1 MR-Linac motion phantom

The 4D-MRI motion phantom (MRI-LINAC Dynamic Phantom, Computerized Imaging Reference Systems Inc., Norfolk, USA) (CIRS, 2014), shown in Figure 4.1, consists of a body shell approximating a human torso in size and shape ($25.5 \times 29.5 \times 20\,\mathrm{cm}^3$). The body shell needs to be filled with an MR signal generating fluid by the user. In this study 7.6 L of mineral oil were used (Marcol Blend 3 T, Philips Healthcare, Eindhoven, The Netherlands), resulting in a total phantom mass of 12.8 kg. The phantom includes a 3D distortion grid for the assessment of geometric accuracy as well as a central fiducial aligned with exterior laser

Figure 4.1: Schematic setup of the CIRS MRI-LINAC Dynamic Phantom - Model 008M (CIRS, 2014) comprising an actuator *(left)*, modular extension shafts *(middle)*, and movable cylinder with simulated target inserted into a torso-shaped body *(right)*. (Image courtesy: CIRS, Computerized Imaging Reference Systems Inc., Norfolk, USA)

marks on the outer shell surface to facilitate a laser-to-isocenter coincidence analysis. A cylindrical thru-hole is incorporated in the phantom body to accommodate a cylinder with a decentralized hyper-intense target to perform rotational and translational movements. The 3D target motion, resulting from the combination of rotation and translation, is software-controlled by an MR-conditional actuator, positioned at a distance of up to 2.655 m from the phantom and connected with modular extendable rigid shafts. The target can optionally host MR-compatible dosimeters for verification of the dose applied by an MR-Linac device.

4.2 Positioning setup for 3.0 T MR scanner modified for RT compatibility

Setup design

The phantom was commissioned on a 3 T MRI scanner (Philips Ingenuity TF PET/MR scanner, Philips Healthcare, Eindhoven, The Netherlands) using a 32-channel SENSE Torso/Cardiac coil. The posterior coil was positioned underneath a glass-fiber flat tabletop overlay in a coil holder (Medibord Ltd, Nottingham, UK), which enabled a stable positioning of the phantom on the patient couch. Likewise, the anterior coil was positioned on a coil bridge. The combination of coil holder and coil bridge facilitated a reproducible positioning of the receiver coils relative to the phantom. In case of a patient scan this setup prevents

Figure 4.2: *Left:* setup of 4D-MRI phantom on flat tabletop overlay positioned on the patient couch. *Top right:* close-up view of phantom positioned on base plate. *Bottom right:* close-up view of actuator positioned on base plate for couch extension

body deformations due to pressure of the coil, simulating the conditions during RT dose delivery.

The maximum distance of 2.655 m between the actuator and magnetic isocenter of the MRI scanner bore, as advised by the phantom manufacturer, could not be realized on the patient couch, which only allowed for a maximum distance of 1.65 m relative to the magnetic isocenter. This provided a safety margin of only 15 cm to the 0.2 T field isoline of the MRI scanner, which was stated to be the minimum distance for safe operation by the phantom manufacturer. Hence, a fixation base plate for the actuator made of polyvinyl chloride (PVC) and polyurethane (PU) was constructed to both extend the couch by 30 cm as well as to mechanically fix the actuator to the couch in order to avoid any projectile hazard in case the 0.2 T field contour is exceeded by a user-related positioning error. Due to the extended positioning of the actuator on the fixation base plate, the phantom body was initially not in-line with the height of the actuator. Hence, new feet made out of polymethyl methacrylate (PMMA) were designed for the phantom to lift it by 17 mm to the necessary height. Incorporating the custom made feed, a positioning base plate made out of PMMA was constructed to allow fast and accurate positioning of the phantom body onto the patient couch (Figure 4.2). The positioning system was constructed with manufacturing tolerances of < 1 mm.

Positional reproducibility

Positional reproducibility was evaluated based on the distance of the central fiducial in the phantom relative to the magnetic isocenter. For such an analysis, the central fiducial is aligned with laser marks on the surface of the phantom shell. The MRI pulse sequence used for evaluation of reproducibility was a 3D GRE sequence with an isotropic voxel size of 1.5 mm and a bandwidth of 721 Hz/pixel (details of the pulse sequence can be found in the supplementary Table B.5). The same sequence was later on used for the distortion analysis. The position of the central fiducial (shown in Figure 4.3) was determined in 3D based on its center-of-mass, which was analyzed using the open source software ImageJ (ImageJ 1.41n, National Institute of Health, Bethesda, Maryland, USA). Since the central fiducial is hypointense in MRI, the images were first inverted and then threshold segmented with a threshold set 3σ higher than the background signal of the mineral oil. Within a time frame of eight months, eight measurements were performed to increase statistical significance.

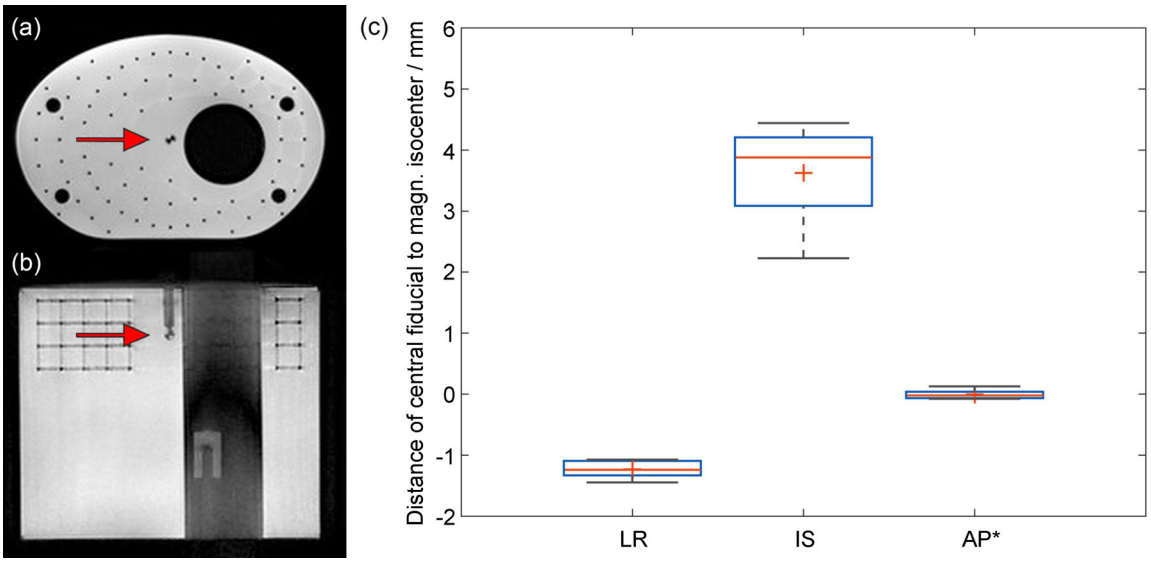

Figure 4.3: *(a)* Transverse and *(b)* coronal view of CIRS motion phantom with the central fiducial used for assessment of positional reproducibility marked with red arrow. *(c)* Distance of central fiducial to magnetic iso-center plotted as boxplot for three directions left-right (LR), inferior-superior (IS) and anterior-posterior (AP). *The distance in AP was corrected for an offset of 77.7 mm.

The results can be found in Figure 4.3 (c), where the distance of the central fiducial to the magnetic isocenter is plotted as boxplot for three directions left-right (LR), inferior-superior (IS) and anterior-posterior (AP). The distance in AP includes an offset of 77.7 mm which was corrected for better illustration. The maximum deviation found were 0.4 mm, 2.4 mm and 0.2 mm in LR, IS and AP, respectively.

Discussion

Before routine usage of the phantom on the 3.0 T MRI scanner, several setup challenges had to be overcome. The flat tabletop overlay, which enables to scan patients in radiation treatment position on the scanner's default concave shaped patient couch, allowed the usage of a coil holder to position a posterior torso/cardiac coil underneath the tabletop overlay. The coil holder setup ensures a stable positioning of the phantom directly on the flat tabletop.

Furthermore, reproducible positioning of the phantom body based on the laser marks showed to be laborious due to the large mass (12.8 kg) of the filled phantom. Therefore, an easily mountable base plate for the phantom was constructed to facilitate a fast and reproducible positioning without affecting MR image quality. While positional reproducibility

was analyzed for three directions, only the measurement in LR direction is truly assessing the reproducibility of the positioning plate, which was measured to be 0.4 mm. This is due to the fact that, firstly, the positioning in AP direction is purely affected by the patient couch. The height of the patient couch is not adjustable with the used scanner and hence showed the smallest deviation of maximum 0.2 mm. Secondly, the positioning in IS direction is mainly limited by the laser alignment, combining both user error as well as inaccuracy of the patient couch mechanics. This increased the deviation in IS direction to 2.4 mm.

MRI acquisitions with and without the actuator showed no noticeable effect on the image quality when positioning the actuator close to the 0.2 T field contour, stated as the minimum distance for safe operations by the phantom manufacturer. However, at this position magnetic forces acting on the partially ferromagnetic actuator had to be considered. The limited length of the MR scanner's patient couch allowed a positioning of the actuator with a distance of maximum 1.65 m to the magnetic isocenter, i.e. at a safety margin of only 15 cm to the 0.2 T field iso-line. An in-house developed fixation base plate increased the safety margin by 30 cm and fixed the actuator on the couch to avoid any projectile hazard in case of accidental mis-positioning of the phantom by the user. However, due to the thereby elevated position of the actuator, the phantom feed had to be redesigned to stay aligned with the actuator which lifted the phantom by an additional 17 mm. In combination with the distance due to the flat tabletop overlay, this led to a distance of the posterior coil to the phantom of $\sim$ 4 cm. Albeit a consequential reduction of the signal to noise level, image quality was sufficient to proceed with the QA assessment of clinically used pulse sequences.

4.3 Image distortion analysis

Methods

A computed tomography (CT) scan of the phantom was acquired (Somatom Definition AS, Siemens Healthineers, Erlangen, Germany) as the ground truth for assessment of the 3D geometric distortion in MRI. A 3D GRE pulse sequence (THRIVE) was used which is typically acquired for abdominal patients in our clinic. The MR images were acquired in transverse orientation with phase encoding in anterior-posterior direction. The scan parameters used for CT and MR imaging of the 3D grid are summarized in the supplementary Table

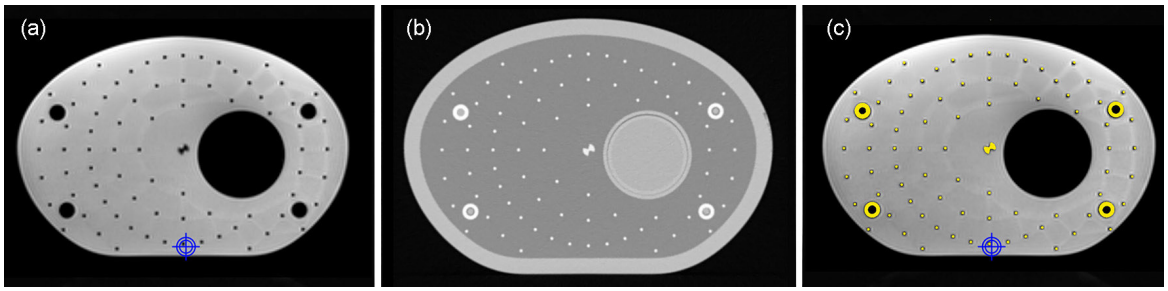

Figure 4.4: *(a)* Transverse MR image (3D T_1 GRE) and *(b)* CT image of the 3D distortion grid. *(c)* The threshold segmented grid structure (yellow) of the CT scan was rigidly registered with the MR scan based on the grid point closest to the magnetic isocenter (blue target).

B.5.

Since the used 3.0 T MR scanner only allowed for a laser alignment along the longitudinal axis, the phantom was positioned differently along the sagittal axis relative to the isocenter of the CT and MR scanner, respectively. Furthermore, since the custom-made positioning setup could only be applied on the flat tabletop of the MR scanner, positioning errors (both in translational and rotational direction) were likely introduced during the CT scan. In order to analyze the 3D image distortion in the MR images, first these positioning differences were corrected by rigid image registration. Image distortion in MRI was then determined by non-rigid image registration. Registration was performed using the open source software elastix (Klein *et al.*, 2009; Shamonin *et al.*, 2014).

Results

Figure 4.4 shows a transverse MR image (3D T_1 GRE sequence), a reference CT image of the 3D distortion grid at the same slice position and the rigid registration of both after threshold segmentation (threshold = 155 HU) of the grid in the CT scan. The magnetic isocenter in the MR images is marked with a blue target symbol, which was due to the flat tabletop overlay and the elevating phantom feet positioned at the posterior end of the phantom. In Figure 4.5, the in-plane geometric distortion is shown for four transverse slices of the grid. As expected, the MR images showed an increasing 3D distortion with increasing distance to the magnetic isocenter with a maximum distortion of $\Delta_{max} = 1.31$ mm at a distance of 160 mm, as plotted in Figure 4.6. The mean absolute 3D Euclidean distance between the grid points on MR and CT images measured over the whole grid volume was $\Delta_{mean} = 0.58\,\text{mm} \pm 0.30\,\text{mm}$. In Figure 4.7 the 2D components of the geometrical distor-

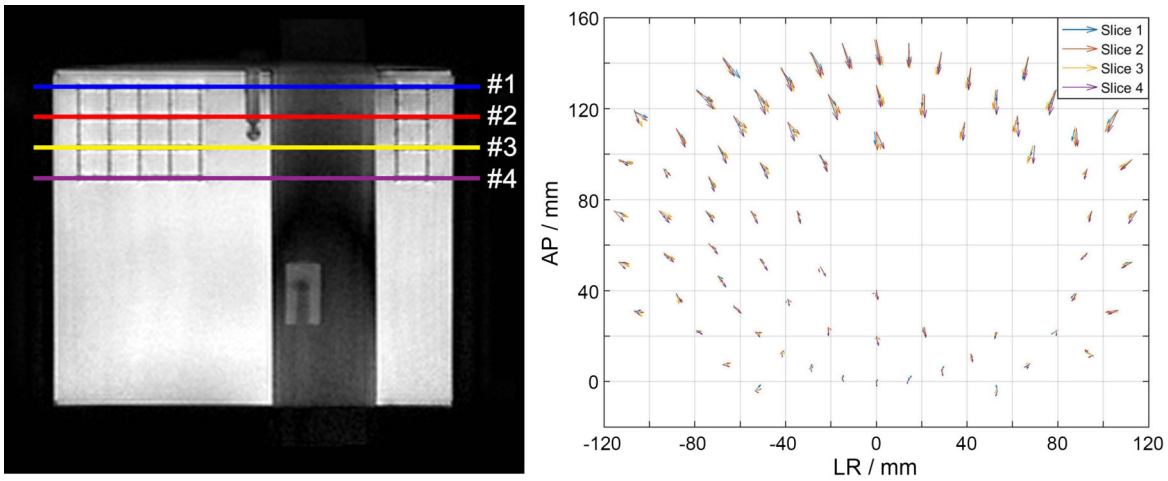

Figure 4.5: *Left:* coronal MR image of the phantom with four transverse slices (color coded) at longitudinal distances to the central fiducial of z= [+30, +10, -10, -30] mm used for the geometric distortion analysis. *Right:* measured in-plane geometric distortion between transverse CT and MR images. Arrows were elongated by 10× for better visibility.

tion is shown separately for all three orthogonal planes, where the distortion in the coronal plane is shown to be the smallest with a mean 2D distortion of $\delta = 0.35\,\text{mm}$.

Discussion

In Fatemi-Ardekani *et al.* (2015) an analysis of the 3D grid distortion on an identical MR scanner by means of different MR sequences (2D T_1w FFE, 2D T_1w TSE and 3D T_1w TFE) has shown similar maximum deviations of 1.0 mm, 0.7 mm and 1.8 mm, respectively. In the referenced study, however, distortion was considered only separately in lateral, anterior-posterior and cranio-caudal direction. In contrast, in the present study the 3D image distortion was analyzed over an elliptic cylindrical volume of $15 \times 23 \times 6\,\text{cm}^3$ using a 3D GRE (THRIVE) sequence. With a maximum 3D distortion of $< 1.31\,\text{mm}$ this sequence fulfills the criteria for stereotactic radiotherapy of targets with a diameter $> 25\,\text{mm}$ (Pappas *et al.*, 2017). It is, however, important to note that the investigated geometric distortion mainly arises from system related sources due to imperfections in the homogeneity of the scanner's static magnetic field and non-linearities in the gradient magnetic fields. Patient related sources due to magnetic susceptibility differences or chemical shift artefacts were not included in the analysis. Furthermore, the geometric distortion was only analyzed for one clinically relevant sequence having a fixed receiver bandwidth of 721 Hz/pixel. Since geometric distortion inversely correlates with bandwidth, the distortion analysis should be

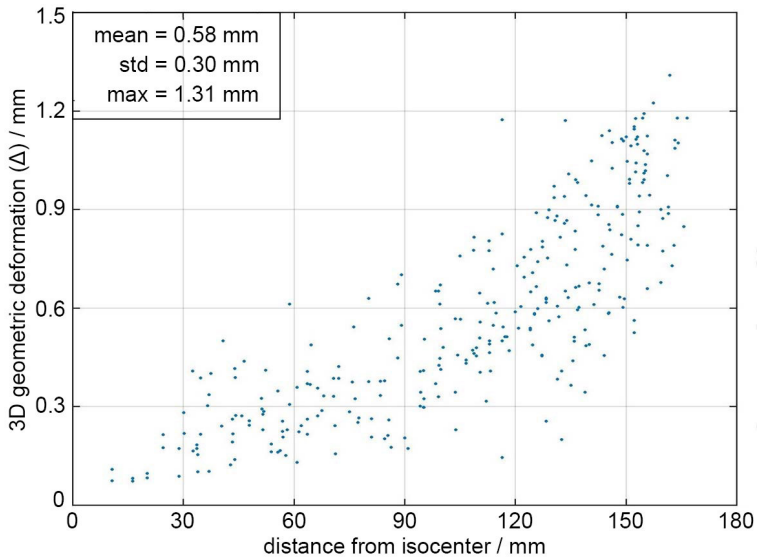

Figure 4.6: 3D geometric deformation Δ, measured by non-rigid registration of the 3D GRE MR image onto the reference CT images.

repeated when other sequences are used.

The phantom's 3D grid covers a range of 6 cm in IS direction, which is sufficient for covering the maximum possible target motion of this phantom. The 3D grid is however not an adequate replacement of a large field homogeneity phantom in order to fully describe the magnetic field homogeneity. For this purpose, different 2D/3D grid-based MR phantoms like the ACR phantom (Chen *et al.*, 2005) or large FOV field homogeneity phantoms (Wang *et al.*, 2004; Baldwin *et al.*, 2007) are available and have proven to be suitable for analysis of geometric distortions.

4.4 Target tracking accuracy

4.4.1 Static displacement in CT

In order to verify the accuracy of the target motion performed by the phantom, CT scans were acquired at different pre-set target positions. The static target displacement was set to the maximum motion amplitude used for this study, with ± 20 mm in IS, ± 5 mm in AP and ± 5 mm in LR direction, respectively. The maximum amplitude was limited by the phantom design to be ± 25 mm / ± 5 mm / ± 5 mm in IS / AP / LR direction, respectively. However the largest amplitude of ± 25 mm in IS direction could not be achieved with desired frequencies

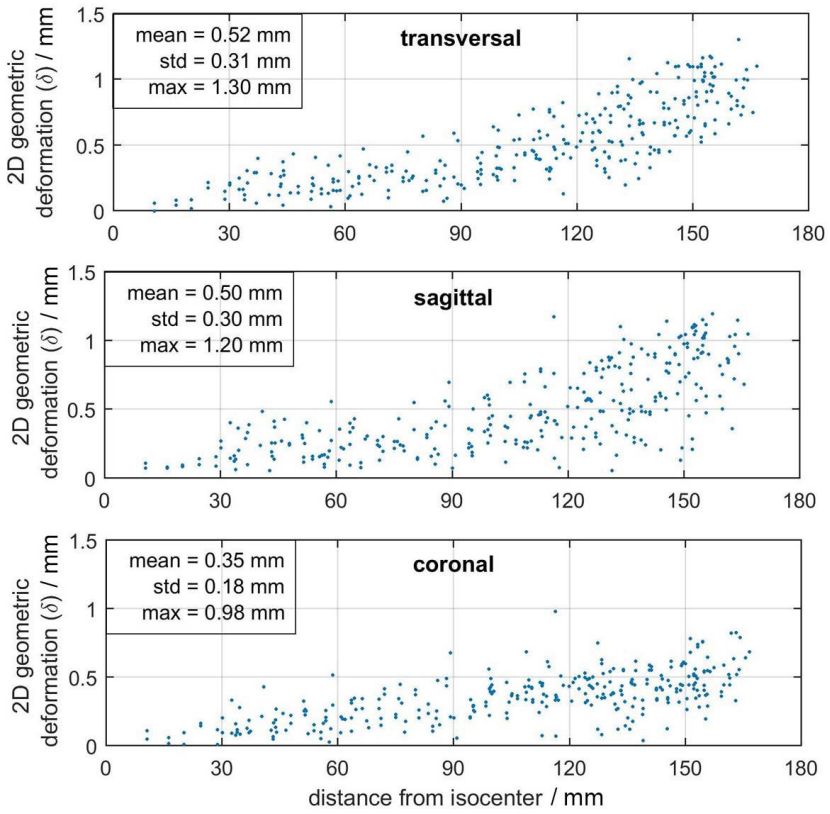

Figure 4.7: Three components of 2D (in-plane) geometric deformation δ of the 3D GRE MR image in transverse, sagittal and coronal orientation, respectively.

of 0.2 Hz, which led to the maximum ± 20 mm used in this work. The pre-set values were then compared to the displacement of the target's center-of-mass found in the CT scan, which where analyzed with the open source software ImageJ. The CT scan parameters are listed in the supplementary Table B.7.

An exemplary transverse and coronal slice of the CT scan of the phantom is shown in Figure 4.8, where the static 3D target displacement is visible for maximum and minimum target positions. The pre-set and the measured displacement are summarized in Table 4.1. While in IS direction no deviation from the pre-set displacement could be measured, the target showed a smaller displacement in AP/LR direction than defined in the controlling software, likely due to a small mis-placement of the target relative to the center of the movable cylinder. Consequently, this intrinsic error has to be considered in the assessment of target tracking accuracy with MRI.

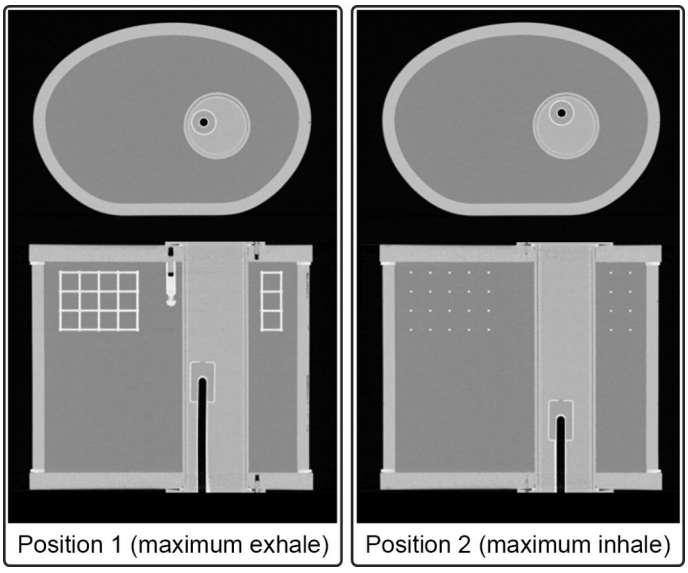

Figure 4.8: Transverse *(top)* and reconstructed coronal *(bottom)* CT image of the phantom for maximum exhale and inhale target positions: -20/-5/-5 mm in IS/AP/LR *(left)* and +20/+5/+5 mm in IS/AP/LR *(right)* .

Table 4.1: Comparison of pre-set target displacement to CT measurement between two different target positions.

Direction of displacement	Pre-set displacement / mm	Measured displacement / mm
IS	40.0	40.0
AP	10.0	9.6
LR	10.0	8.9

4.4.2 Relaxometry for MRI sequence optimization

For balanced steady-state free precession (bSSFP) pulse sequences, as used in our clinic for MRI based motion analysis, the signal intensity is given by

$$M_{SS} = \rho(\mathrm{H}) \frac{\sqrt{E_2 \cdot (1 - E_1) \cdot \sin\alpha}}{1 - (E_1 - E_2) \cdot \cos\alpha - E_1 \cdot E_2}, \tag{4.1}$$

with $E_{1,2} = e^{\mathrm{TR}/\mathrm{T}_{1,2}}$ and ρ(H) is the proton density. Under the assumption that TR $\ll T_1$ and TR $\ll T_2$, which is typically the case for TR $\approx$ 3 ms, as used for cine acquisitions, equation

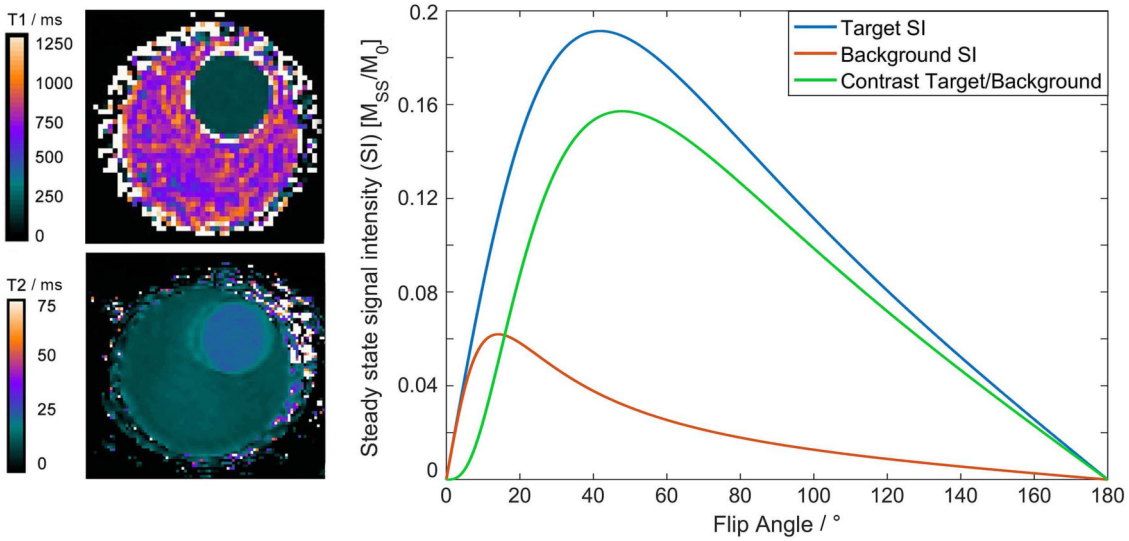

Figure 4.9: T_1*-(top left)* and T_2 *(bottom left)* relaxation times at 3T clearly show the decentralized target in the top right of the movable cylinder. *(right)* Signal of the target and background cylinder of the motion phantom as a function of flip angle in bTFE sequences, as used for motion depicting cine MRI sequences.

4.1 can be simplified to

$$M_{SS} = \rho(\mathrm{H}) \frac{\sin\alpha}{1 + \cos\alpha + (1 - \cos\alpha) \cdot (\mathrm{T_1}/\mathrm{T_2})}. \tag{4.2}$$

The contrast between two structures can therefore be modified based on the flip angle (Scheffler and Lehnhardt, 2003), if their relaxation properties are known.

Hence, MR relaxometry of the movable target and its background gel was performed, as described in section 2.3.2. For T_1 determination an inversion recovery spin-echo (IR SE) method with six different inversion times was acquired. A T_1-map was then calculated by fitting the complex data to a five-parameter model (Barral *et al.*, 2010). A T_2-map was calculated based on a gradient-and-spin-echo (GraSE) sequence (Fernández-Jiménez *et al.*, 2015) sampled at nine echo times by fitting the magnitude data to a mono-exponential function. To minimize the influence of B_1 inhomogeneities found in multi-echo SE sequences, a correction was performed by discarding the first echo signal (Lebel and Wilman, 2010; Milford *et al.*, 2015). The scan parameters used for MR relaxometry are summarized in the supplementary Table B.6.

Relaxometry yielded the quantitative T_1- and T_2-maps shown in Figure 4.9, from which it can be appreciated that the target and background gel in the movable cylinder show a

different relaxation behavior at 3 T. In Table 4.4.2 the measured relaxation behavior of target and background gel of the cylinder are shown. Based on the found relaxation properties of the cylinder, the flip angle for the theoretically optimum contrast in bSSFP sequences was found to be $\alpha = 47.8°$, as can be appreciated from the function of contrast in Figure 4.9. For bSSFP sequences this relatively large flip angle increased the acquisition time to an unacceptable level. Hence, the flip angle was finally reduced to 30°, to achieve a satisfactory temporal resolution of > 2 Hz.

Table 4.2: Measured (mean ± standard deviation) T_1 and T_2 relaxation times at 3.0 T of the target and background gel in the movable cylinder as determined by MR relaxometry.

	Phantom target	Cylinder background
T_1 / ms	208.1 ± 2.8	871 ± 36
T_2 / ms	30.5 ± 0.7	13.4 ± 1.3

4.4.3 Phantom target motion in MRI

Methods

A bSSFP sequence was used for the evaluation of 1D- and 2D-motion trajectories in single-slice coronal and transverse 2D-cine MRI. For the analysis of 3D-motion trajectories, an orthogonal 2D-cine MRI scan was acquired interleaved in transverse and sagittal orientation. Additionally, based on the method by Von Siebenthal *et al.* (2007), a 4D-MRI dataset was reconstructed for 3D motion assessment using MATLAB (MATLAB R2016a, The Mathworks Inc., Natick, USA) by retrospectively binning a multi-slice 2D-cine MRI acquisition with no slice gap combining classical phase and amplitude binning methods. The continuously acquired 2D images of a 3D volume with 40 dynamics were resorted into a maximum inhale and exhale phase as well as three phases in between with directional dependency, which were sorted based on the trajectories amplitude, to obtain eight trajectory phases in total. In order to be less affected by the binning algorithm performance the phantom's set trajectory was used as surrogate of a respiratory curve instead of a 1D MR navigator or image navigator. Moreover, a 1D MR navigator signal following the target could not be successfully extracted from the scanner. An examplary image of the phantom in two respiratory states depicted by 4D-MRI can be seen in Figure 4.10. All cine MR images were acquired with a

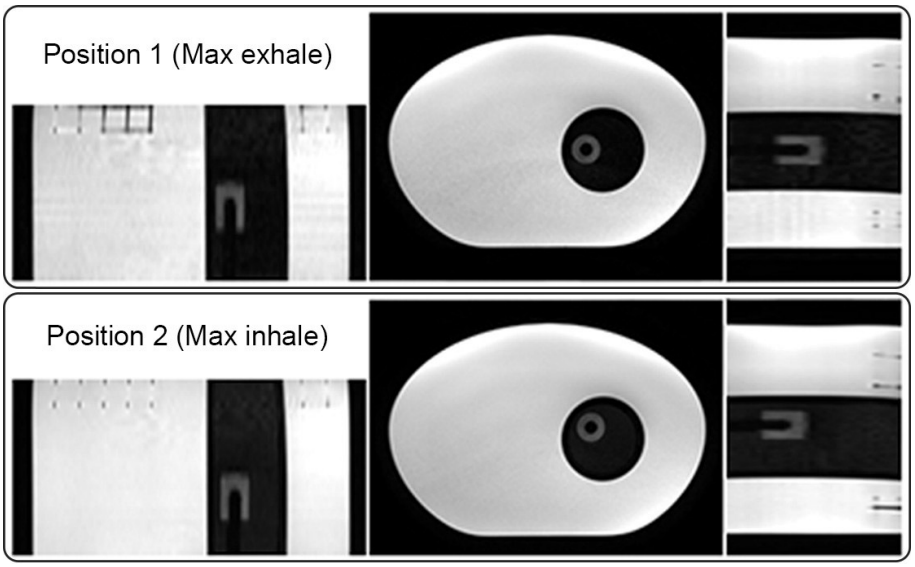

Figure 4.10: CIRS phantom performing sinussoidal 3D target motion with amplitudes of $\pm$ 7.5/5/2.5 mm in IS/AP/LR direction was scanned by means of retrospectively resorted 4D-MRI with 8 respiratory phases. The maximum exhale*(top)* and maximum inhale *(bottom)* positions are shown in all three orthogonal planes (from left to right: coronal, transverse, sagittal). The coronal and sagittal images were reconstructed from the volumetric dataset that was acquried in transverse orientation.

temporal resolution of >2 Hz.

Sinusoidal 1D-, 2D- and 3D-motion trajectories were programmed in the graphical user interface of the phantom's control software. In addition, a realistic motion pattern was imported from a 1D MR navigator scan of a healthy volunteer with a mean frequency of 0.17 Hz and motion amplitudes <20 mm. The pre-set frequencies (0.1 Hz – 0.2 Hz) and amplitudes (maximum $\pm$ 20 mm in IS, $\pm$ 5 mm in AP and $\pm$ 5 mm in LR direction) were based on breathing patterns observed in patients (Keall *et al.*, 2006). All set motion trajectories can be found in the supplementary Table B.8. For motion analysis the phantom target was aligned longitudinally to be in plane with the magnetic isocenter.

The motion analysis was performed using an in-house developed automated tracking algorithm based on functions provided by the Image Processing Toolbox of MATLAB (MATLAB R2016a, The Mathworks Inc., Natick, USA). The 2D-cine MR images were first preprocessed by applying a Gaussian filter to reduce the influence of noise and artifacts. Objects with connected structures were identified by threshold detection. From these objects, the target was identified based on its known geometric properties. Subsequently, the center-of-mass of the target was determined as a surrogate for its position at each time step. The measured positions were fit with a sinusoidal function by minimizing squared er-

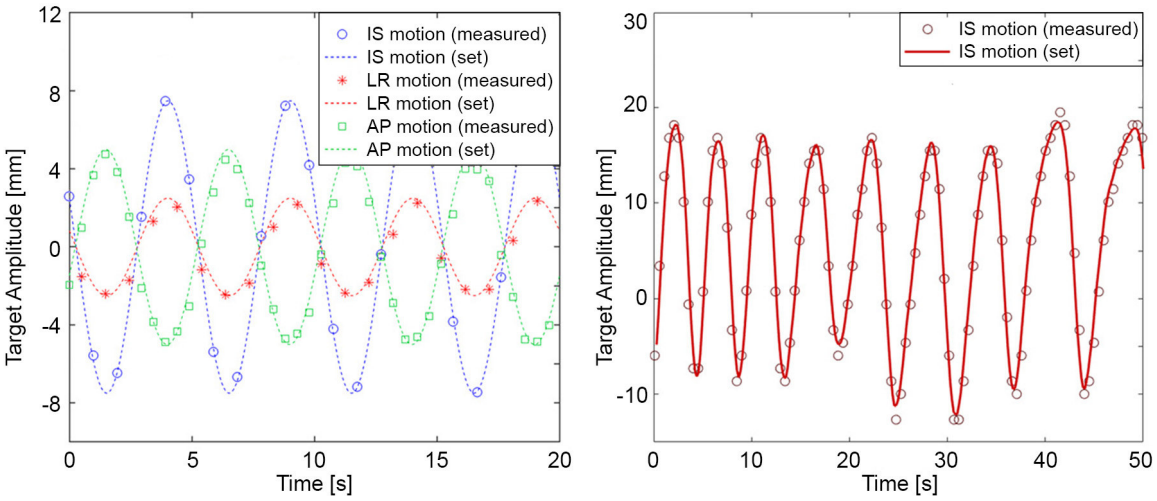

Figure 4.11: *Left:* programmed and measured 3D sinusoidal target motion patterns using pre-set amplitudes of ± 7.5/5/2.5 mm in IS/AP/LR direction. *Right:* 1D navigator-based volunteer breathing pattern with pre-set and measured target positions.

rors using the simplex search method (Lagarias *et al.*, 1998), from which the amplitude and frequency were estimated. For analysis of the 3D motion in the reconstructed 4D-MRI, the target was manually segmented in each trajectory phase over the whole volume to determine the center-of-mass in every state of motion. The maximum displacement was then determined as the distance of the target's center-of-mass between the reconstructed maximum inhale and exhale state. The MR scan parameters are listed in supplementary Table B.7.

Results

The motion trajectories programmed in the target motion control software and the motion patterns measured from 2D-cine and reconstructed 4D-MRI are listed in Table B.8. An exemplary sinusoidal 3D target trajectory and real volunteer navigator data is shown in Figure 4.11 with the respective measured target position overlayed. For the sinusoidal motion patterns, the estimated frequencies agreed within 0.5 % to the pre-set frequencies. When considering the intrinsic error in AP/LR direction found in section 4.4.1, the measured amplitudes showed a mean deviation < 0.2 mm in all three directions. For the 1D navigator motion pattern extracted from a volunteers breathing pattern, the estimated motion parameters showed a maximum deviation in amplitude of 1.0 mm and a mean deviation of 0.3 mm in IS direction (Figure 4.11). The motion amplitudes extracted from the transversely

acquired retrospectively binned 4D-MRI showed a deviation of < 0.3 mm in all directions. Due to the rotation of the target cylinder to induce motion in the transverse plane (AP/LR) it is obvious that it is not possible to set a pure 1D motion in AP/LR direction. Therefore, when a sole AP motion was set an additional displacement of 0.4 mm in LR direction was measured, whereas a pure LR motion trajectory resulted in an additional displacement of 0.5 mm in AP direction. This deviation from a set zero motion was hence treated separately and was not included in the measured deviation listed above.

Discussion

MR relaxometry was performed to facilitate sequence optimization, i.e. adaption of the flip angle for contrast enhancement of the target. However, since for motion depicting MR sequences the temporal resolution is one of the most critical sequence parameters, the flip angle was finally adjusted to achieve a sufficiently short temporal resolution of ≈ 2 Hz. For different magnetic field strengths than 3T the image quality would need to be reassessed and MR sequence parameters may need to be adjusted based on the T_1/T_2 values of the target and the background material to obtain high contrast images. The relaxation parameters should also be considered for an elaborated choice of signal generating medium for the phantom body.

The reference CT measurement of the extreme target displacement revealed a good agreement with the pre-set parameters, however not within the accuracy of < 0.1 mm as stated by the vendor. While in IS direction no measurable deviation from the set amplitude was found, in AP/LR direction the target displacement was 0.2 mm and 0.5 mm, respectively. This deviation has to be considered when analyzing the accuracy of MR based motion tracking sequences.

The measured motion parameters found by single slice 2D-cine MRI as well as orthogonal 2D-cine MRI agreed well with the pre-set values. The measured deviations in IS direction were < 0.2 mm, and in consideration of the intrinsic error found in section 4.4.1 the same deviation of < 0.2 mm were found in AP/LR direction. The 3D motion analysis based on the retrospectively resorted 4D-MRI sequence also agreed well with the set trajectory but with slightly higher deviations in IS direction of 0.3 mm. In this sequence a larger deviation in IS direction was expected, since slice orientation was transverse and therefore resolution in IS direction was the lowest (5 mm). Considering the relatively low resolution in

IS direction given by the slice thickness, the found deviation in IS direction is still remarkably small. MR motion analysis measurements with different MR motion phantoms have shown similar results with motion amplitude errors of 0.1 mm – 0.4 mm (Lagendijk *et al.*, 2008) and have reported on good agreement between measured and reference positions (Soliman *et al.*, 2016).

With respect to motion extraction in MRgRT, the 4D-MR phantom used in this study shows some limitations. Firstly, the phantom motion is purely rigid, which is usually not the case for moving tumors or organs at risk. Secondly, for patient cases, image artifacts caused by different magnetic susceptibility may occur, leading to additional magnetic field distortions of the resulting MR images (Czervionke *et al.*, 1988). Future studies should take these effects into account by combination of measurements with both rigid phantoms having highly reproducible motion behaviors and dynamic non-rigid anthropomorphic phantoms (Ehrbar *et al.*, 2016; Mann *et al.*, 2017).

4.5 Summary

A 4D-MRI dynamic phantom was successfully commissioned on a diagnostic 3.0 T MRI scanner used for MR simulation in RT. A fixation and positioning aid was designed and constructed to overcome several compatibility issues that appeared when using the MRI-Linac motion phantom on this MR scanner. The setup facilitates repeated QA, for which it allows for a highly reproducible phantom positioning.

For a fast analysis of geometric fidelity within a QA procedure, a method for automatic distortion analysis was developed based on a previously acquired reference CT scan. The analysis of a clinically used 3D GRE sequence showed that it fulfills the criteria for stereotactic radiotherapy of targets with a diameter of >25 mm with a measured maximum 3D distortion of 1.3 mm.

Furthermore, the accuracy of the 3.0 T MR scanner in tracking of motion was assessed based on single-slice 2D-cine, orthogonal 2D-cine and retrospectively resorted 4D-MRI. High-contrast and geometrically reliable 2D-cine MR images of the phantom's moving target could be obtained. The accuracy of the used sequences was found to be <0.2 mm in single-slice and orthogonal 2D-cine acquisitions, and <0.3 mm in 4D-MRI when the found intrinsic error of the target motion in AP/LR direction is considered. The high accuracy found

in the phantom measurements gave us confidence in using these sequences for organ motion assessment in patients. For the analysis of continuously acquired cine acquisitions a Matlab based tool was developed for automatic quantification of multi-dimensional target motion. The two developed tools can be used for automatic evaluation in repeating QA of spatio-temporally resolved MR sequences used for MRgRT.

5 Reduction of respiratory organ motion by use of an abdominal corset

Appropriate immobilization of the target volume is a key component in the treatment process for precise dose delivery. This is of particular importance for PT due to its relative to XT higher sensitivity to density variations caused by inter- and intrafraction changes in patient anatomy. Morphological changes along the beam path due to organ motion, deformation and filling can influence the position of the Bragg peak relative to the target volume. Furthermore, the use of active dose delivery techniques that employ scanned beams to volumetrically scan a mono-energetic Bragg peak over the target volume in combination with intrafraction organ motion may further degrade the precision of dose delivery due to the interplay effect (Phillips *et al.*, 1992; Bert *et al.*, 2008a). This may result in over- or underdosage of the target volume and unwanted dose deposition in adjacent organs at risk.

For thoracic and abdominal organs, the main source of intrafraction motion is respiration. To reduce respiration-induced uncertainties in PT, breathing motion can be accounted for by 4D treatment planning and optimizations (Bert and Durante, 2011; Graeff, 2014; Dolde *et al.*, 2018a), rescanning (Knopf *et al.*, 2011), tumor tracking (Bert *et al.*, 2008b) or gating (Mori *et al.*, 2009). However, their individual application has shown to not completely mitigate motion effects (Kraus *et al.*, 2011; Zhang *et al.*, 2018) and particularly when no active tumor motion control options are available, physically reducing respiratory induced motion by abdominal compression techniques (Fontana *et al.*, 2016; Heerkens *et al.*, 2017; Dolde *et al.*, 2018b) becomes critical in order to prevent extensive margin expansion of the planning target volume.

For PT of targets in the upper gastro-intestinal tract, motion mitigation by means of abdominal compression bands or pressure plates can exacerbate the range uncertainties when the devices extend into the treatment fields due to a limited setup reproducibility and consequential edge effects (Wroe *et al.*, 2014). In particular, pressure plates incorporated

in a frame system for reproducibility only allow for limited usability in MR guided PT due to their bulky setup. Since in PT the proton beam nozzle should be positioned close to the patient's surface in order to reduce lateral beam spread in air (Newhauser and Zhang, 2015), the risk of a collision of the immobilization device with the nozzle arises by using such frame based pressure plates. Moreover, compression bands are known to be the source of a high level of patient discomfort (Mampuya *et al.*, 2014; Van Gelder *et al.*, 2018) which can increase the tumor motion variability (Bissonnette *et al.*, 2009).

As a solution to reduce respiratory induced tumor motion in patients with pancreatic cancer, polyurethane-based customized abdominal corsets have recently been used in stereotactic XT (Heerkens *et al.*, 2017). Moreover, studies using MRI in orthogonal 2D-cine or 4D mode have shown the ability of abdominal corsets to reduce pancreatic motion mainly in inferior-superior direction (Fontana *et al.*, 2016; Heerkens *et al.*, 2017; Dolde *et al.*, 2019b). However, corsets used in XT may not be applicable for PT, since for the latter a high reproducibility of the setup for immobilization devices placed in the beam path is critical and higher standards of material properties (i.e. thickness and homogeneity) have to be met in order to be able to correctly calculate the beam penumbra and range in the patient. Therefore, in this work three types of abdominal corsets that differ in terms of material composition, size, and degree of patient customization were compared regarding their suitability for PT. In PT, the water equivalent ratio (WER) of any material placed in the beam path needs to be known precisely to ensure that the treatment planning system is able to accurately take the materials effect on beam penumbra and range into account. Hence, in section 5.1, the WER of the three tested corsets was determined and their material was analyzed to assess the degree of material homogeneity and variance in thickness. Furthermore, their effect on respiratory motion reduction was tested for one healthy volunteer based on orthogonal 2D-cine MRI and 4D-MRI.

With one corset, which was considered to be suitable for PT, a patient study was conducted. In this study, for patients with an abdominal tumor (pancreas, liver, gallbladder) scheduled for PT, an individual corset was constructed before the treatment planning was performed. In section 5.2 the implementation of the corset in the PT workflow and treatment planning is presented. The design of the corset considers several challenges which the clinical implementation brought to light (section 5.2.1). The effect of the corset on the respiratory pancreas motion was analyzed based on orthogonal 2D-cine and 4D-MRI (section 5.2.2). Finally, the patient's acceptance toward the corset was evaluated (section 5.2.3).

The results of this work have in part been published by Dolde *et al.* (2019). The measurements and analysis for the determination of the WER values of the corsets were performed with the friendly support of Nils Peters.

5.1 Comparison of three different abdominal corsets for use in particle therapy

In this study, three different abdominal corsets were investigated: a foam-based polyurethane corset (PU), a polyethylene corset (PE) and a 3D-scan based polyethylene corset (3DPE). All three corsets applied onto the healthy volunteer in this study, are shown in Figure 5.1.

Polyurethane corset (PU)

The patient-individualized PU corset (OKMSystem®, OKM Química Ortopédica, Girona, Spain) is a custom-made (Orthopädie und Rehatechnik Dresden GmbH, Dresden, Germany) solid foam-based corset enclosed in a cotton fabric, which is molded in soft condition directly around the lumbar spine, where it hardens within 20 min after mixing its initial liquid components isocyanate and polyol. The corset is fastened using hook-and-pile fasteners, which were positioned ventrally, 5 cm left of the mid-sagittal plane. In inferior-superior direction, the corset ranged from the ileum to the xiphoid process, compressing the stomach and lower four ribs. Its manufacturing and solidifying require approximately 30 min in total. This type of corset has been shown to reduce respiratory pancreas motion in the frame of stereotactic XT (Heerkens *et al.*, 2017).

Polyethylene corset (PE)

This Boston Overlap Brace (BOB)-hull orthoses (Basko Healthcare, Hamburg, Germany) corset was fitted in cooperation with the Prosthetics and Orthotics Department of the Heidelberg University Hospital, Germany. It consists of a polyethylene (PE) prefabricated symmetrically formed module that enables individual adaptation based on size and gender. Three different lordosis angles (0°/15°/30°) are available. The trim lines are adjusted to the patient's individual anatomy to avoid uncomfortable pressure to the greater trochanter and the axilla. The corset is ventrally closed by four hook-and-pile fasteners, such that no

Figure 5.1: Healthy subject with three different corsets, which were used in this study: *(a)* A patient-specific polyurethane corset (PU), *(b)* a semi-specific polyethylene corset (PE) and *(c)* an optical 3D-scan based polyethylene corset (3DPE).

fastener material or buckles are present at the side and back of the subject. This type of corset allows for an adequate stabilization of the lumbosacral spinal segments from the sacral spine (S1) up to the thoracic spine (Th8). Corset adjustment lasts for approximately 30 min.

3D-scan based polyethylene corset (3DPE)

The patient-individualized 3DPE corset (Orthopädie- und Rehatechnik Dresden GmbH, Dresden, Germany) is custom-made based on an optical 3D-surface scan (Artec Eva®, Artec3D, Luxembourg, Luxemburg) of the patient. The 3D-surface scan is performed in treatment position using a vacuum cushion (TapMed Medizintechnik Handels GmbH, Habichtswald, Germany) for modeling the dorsum from its imprint. The surface model is finally replicated as a milled wooden model onto which a 5 mm PE plate (Streifylast®/Trolen) is thermoformed in an industrial oven at 150 °C. The individually shaped corset is finally adjusted and equipped with hook-and-pile fasteners, which were positioned on the anterior and posterior left side of the corset, approximately 5 cm and 12 cm away from the mid-sagittal plane, respectively. In inferior-superior direction, the corset ranged from the xiphoid process to the ilium, compressing the stomach and the lower five ribs. The modeling and manufacturing requires two outpatient clinic appointments of 20 min duration each and a total manufacturing time of at least 3 days between the two appointments.

5.1.1 Homogeneity and thickness of the corsets

Material and methods

CT scans of all corsets were acquired (Somatom Definition AS, Siemens Healthineers, Erlangen, Germany) to assess material homogeneity and regularity of thickness (pixel

size = 0.8 mm², slice thickness = 2 mm, tube voltage = 140 kVp, tube current time product = 80 mAs). Material homogeneity was assessed based on the standard deviation of the measured CT numbers of the respective corset, measured at 10 different slice positions. Furthermore, the size and distribution of air inclusions in the PU corset was analyzed due to its heterogeneity. To quantify the size and number of air inclusions, the air inclusions were automatically threshold-based delineated in the CT image and analyzed by means of a connected-components analysis using MATLAB (MATLAB R2017b, The Mathworks Inc., Natick, USA) and analyzed thereby. The corset thickness was measured as the full width at half maximum (FWHM) of the corset's intensity profile at five different positions in five different slices in the CT images, using the open-source software ImageJ. Due to the varying thickness of the PU corset, the maximum and minimum thickness were stated instead of a mean thickness value. The thickness was measured in treatment-relevant regions of the corset around the longitudinal center and at beam angles between 140 °– 270 °. The angles were chosen based on the fact that pancreatic cancer patients are typically treated with two or three posterior oblique beams at our PT facilities in Dresden and Heidelberg.

Results

All measured material properties are listed in Table 5.1. The acquired CT images confirmed a homogeneous material in the PE / 3DPE corsets with CT values of - 130 HU ± 31 HU / - 107 HU ± 32 HU and no visible hyper- or hypointense structures. Moreover, a constant thickness of 2.8 mm ± 0.2 mm / 3.8 mm ± 0.2 mm was found for the PE and 3DPE corset, respectively. The PU corset material was inhomogeneously comprising air inclusions throughout the whole corset with sizes of up to 7.6 mm in diameter and a mean volume of 12.9 mm³ (range 1.2 mm³ – 263.7 mm³). 95 % of the air inclusions were smaller than 50 mm³, and 5 % had larger volumes of up to 263.7 mm³ (see Fig. 5.2). Moreover, smaller hyperintensities were observed in the CT images. The HU density of these small hyperintense volumes did not correspond to components in the list of materials received from the manufacturer and the origin of these hyperintensities was not identified. For the PU corset, the average CT value was - 677 HU ± 113 HU with values from - 1024 HU (air inclusions) to + 990 HU (hyperintensities). Furthermore, its thickness varied between 4.2 mm – 27.7 mm.

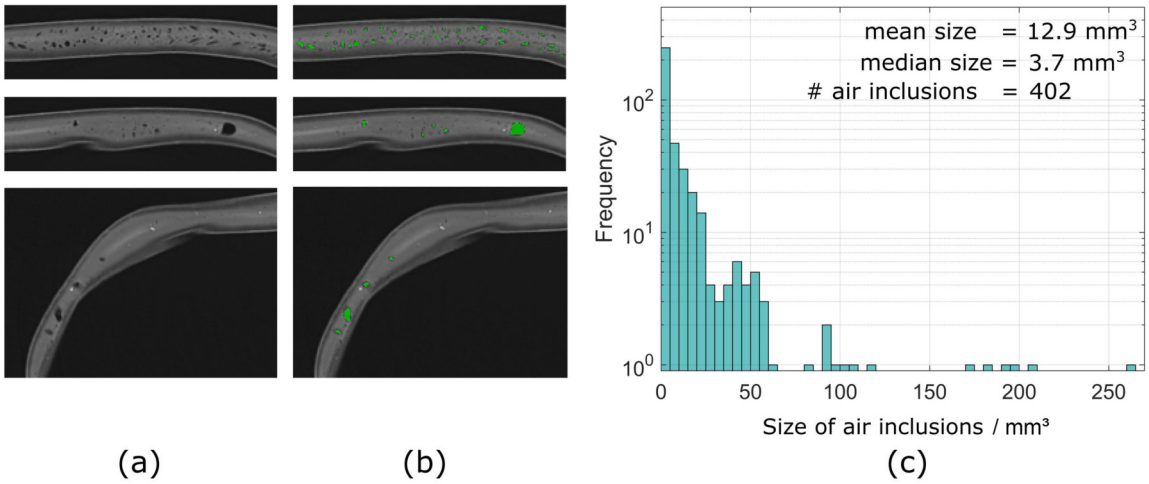

Figure 5.2: In the CT-Scan of the PU-Corset, air inclusions with different sizes are visible as shown in three exemplary slices *(a)* and with superimposed threshold-segmented volumes in green *(b)*. The distribution of the air inclusions *(c)* shows 95 % to have a volume of $< 50\,\mathrm{mm^3}$ with maximum volumes of up to $264\,\mathrm{mm^3}$.

5.1.2 Analysis of water equivalent ratios of the corsets

Material and methods

The WER is defined as the ratio of the mass thickness of water and the given material (in $\mathrm{g/cm^2}$) that leads to the same beam energy loss (De Vera *et al.*, 2013). WER measurements were performed at the University Porotn Therapy Dresden with two different proton energies (150 MeV, 200 MeV) using a multi-layer ionization chamber (Giraffe, IBA Dosimetry, Schwarzenbruck, Germany) that measured the shift of the single Bragg peak along the central beam axis after penetrating the respective corset samples. The corset samples, approximately $10 \times 10\,\mathrm{cm^2}$ in size, were positioned directly in front of the entrance window of the ionization chamber at a distance of 50 cm to the proton beam nozzle. Each sample was measured twice for both proton beam energies, respectively, with and without the PMMA cover of the ionization chamber. This increased the number of data points for each depth-dose curve, which was then fitted with a Bortfeld-fit (Bortfeld and Schlegel, 1996). The proton range was determined by the depth of the 80 % dose level at the distal dose fall-off of the Bragg peak (R_{80}). The two samples of the PU (PU1 and PU2, respectively) and PE corsets were cut out of an already manufactured corset, while the 3DPE sample was provided from raw material prior to its thermoforming. The thickness of the samples was measured with a caliper five times at three different spots around the center of the

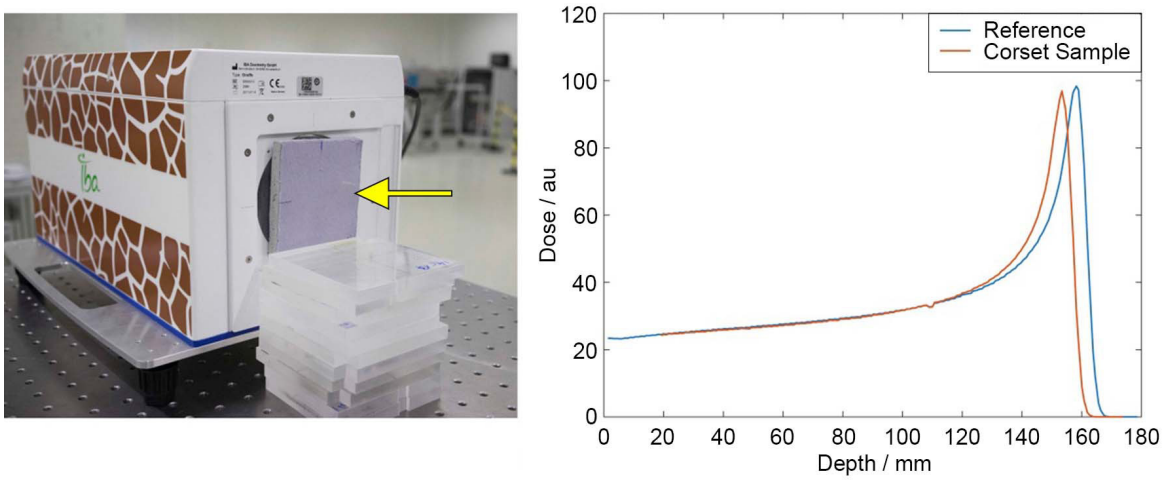

Figure 5.3: (a) Sample of the polyurethane corset (yellow arrow) positioned in front of the multi-layer ionization chamber at a distance of 50 cm to the proton beam nozzle for measurement of water equivalent ratio. (b) Depth dose curve of 150 MeV proton beam with PU corset sample in beam path and without sample as reference.

respective sample. The center of the sample was aligned with the proton beam axis.

Results

The setup for measuring the WER of the corset samples as well as an exemplary dataset showing the shifted Bragg peak for the PU sample is illustrated in Figure 5.3. Due to the inconsistent thickness of the PU corset, two samples were analyzed which were cut out from a region with the most constant thickness found in the corset. The average thickness of the PE, 3DPE and the two PU samples used for the WER measurements was $2.53\,\text{mm} \pm 0.07\,\text{mm}$, $4.87\,\text{mm} \pm 0.03\,\text{mm}$ and $11.42\,\text{mm} \pm 0.34\,\text{mm}$ / $10.10\,\text{mm} \pm 0.29\,\text{mm}$, respectively. The difference in thickness between the 3DPE corset and the 3DPE sample of 1 mm resulted from the thermo-forming of the base material during the corset manufacturing process, which reduces the thickness of the base material. The WER of the PE and the 3DPE corset averaged over the two used proton energies was almost water-equivalent with 0.9556 ± 0.0001 and 0.9900 ± 0.0030, while for the PU corset the WER was substantially smaller with 0.2980 ± 0.0010.

Table 5.1: Material analysis of the three tested corsets. The measured thickness of corsets and samples, material homogeneity as well as the average measured water equivalent ratio (WER) for protons at energies of 150 MeV *(a)* and 200 MeV *(b)*, respectively, are listed. Two samples of the PU corset (PU1, PU2) were analyzed due to the heterogeneity of the corset. For the corset thickness, sample thickness and material homogeneity, the indicated uncertainties represent the standard deviation of the measured value from multiple measurements ($N \geq 15$). The uncertainties of the WER measurement resulted from the uncertainty of the underlying Bortfeld-Fit of the depth-dose curve.

Corset	Corset thickness / mm	Sample thickness / mm	Material homogeneity / HU	WER
PE	2.8 ± 0.2	2.53 ± 0.07	-130 ± 31	$0.956 \pm 0.002^{(a)}$ $0.956 \pm 0.002^{(b)}$
3DPE	3.8 ± 0.2	4.87 ± 0.03	-107 ± 32	$0.988 \pm 0.002^{(a)}$ $0.993 \pm 0.002^{(b)}$
PU1	4.2 – 27.7	11.42 ± 0.34	-677 ± 113	$0.297 \pm 0.002^{(a)}$ $0.297 \pm 0.002^{(b)}$
PU2	4.2 – 27.7	10.10 ± 0.29	-677 ± 113	$0.298 \pm 0.002^{(a)}$ $0.298 \pm 0.002^{(b)}$

5.1.3 Respiratory motion reduction

Material and methods

To quantify respiration-induced pancreatic motion, a healthy volunteer (male, age 29 years) was scanned in treatment position with the arms positioned superior to the head (WingSTEP, Innovative Technologie Völp, Innsbruck, Austria) on a custom-made wooden flat-table top overlay inside a 1.5 T MR scanner (Magnetom Aera, Siemens Healthineers) using a combination of a 14-channel phased array spine coil, which was positioned inside the patient couch, and an 18-channel phased array torso coil, which was placed directly on the corset/volunteer.

The volunteer underwent respiratory phase-resolved volumetric 4D-MRI and fast orthogonal single-slice 2D-cine MR imaging in coronal and sagittal orientation while subsequently wearing one of the three corsets and without corset for reference. The scans were performed twice on two consecutive days to investigate reproducibility of the pancreatic motion reduction. The 4D-MRI data hence provides information about the interfraction motion variability. No specific breathing instructions were given to the volunteer, aiming to acquire

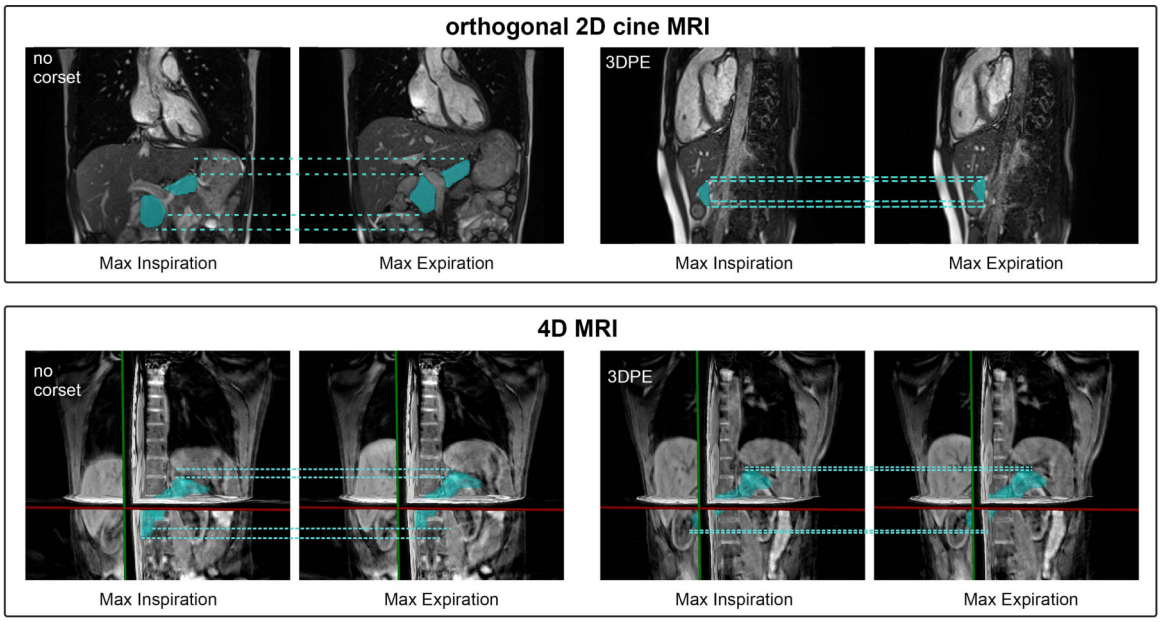

Figure 5.4: Orthogonal single-slice 2D cine (coronal and sagittal) (*top*) and 4D MRI (*bottom*) of healthy volunteer in free breathing (*left*) and wearing the 3DPE corset (*right*) showing the state of maximum expiration and inspiration. The pancreas is segmented and lines are added at the caudal and cranial edge of the pancreas to visualize the amount of pancreatic motion.

free-breathing patterns. For the 4D-MRI measurements, a T_1-weighted GRE sequence with radial golden angle stack-of-stars sampling was used to acquire 3D images under free breathing of the subject (field of view = $384 \times 384\,\text{mm}^2$, pixel spacing = $1.5 \times 1.5\,\text{mm}^2$, slice thickness = 3 mm, spokes per partition = 2100, bandwidth = 610 Hz/pixel, echo time (TE) = 1.5 ms, repetition time (TR) = 3.3 ms, flip angle = 12°, acquisition time = 8 min, reconstructed phases per respiration = 20). The raw data were reconstructed offline, using a motion-compensated iterative reconstruction algorithm, based on a k-space-center self-gating signal, which provides up to 20 overlapping breathing phases (Rank *et al.*, 2016). On each 4D-MRI data set, the pancreas was manually delineated on the end-inhale and end-exhale images using the open-source software MITK (German Cancer Research Center, Heidelberg, Germany). All contours were validated by an experienced radiation oncologist. The center-of-mass of these delineations was determined to estimate the pancreatic motion in IS, AP and LR directions.

To allow an analysis of pancreas motion during individual breathing cycles and thereby assess the intrafraction motion variability, orthogonal single-slice 2D-cine MRI were acquired using a TrueFISP sequence in coronal and sagittal orientation at a frame rate of

approximately 4 Hz (field of view = 384 × 384 mm², pixel spacing 1.5 × 1.5 mm², slice thickness = 4 mm, bandwidth = 1030 Hz/pixel, TE = 1.26 ms, TR = 222.3 ms, flip angle = 55 °, acquisition time = 50 s). The pancreas was manually segmented in the 2D images and tracked by the position of its center-of-mass. The motion amplitude was determined as the average peak-to-peak motion amplitude between several inhale and exhale states, where the upper and lower 2.5 % of the data were discarded (M_{95}) to reduce the effect of outliers. For each motion direction the standard deviation of the respective motion amplitude is given as measure of intrafraction variability.

The 2D-cine MRI data was used to determine the real-time motion amplitudes in IS, LR and AP direction of a selected area of the pancreas as well as the length of breathing cycles, whereas the 4D-MRI data provides averaged information over several breathing cycles in IS, LR and AP directions for the full pancreas volume. Exemplary images of 2D-cine and 4D-MRI are shown in Figure 5.4 where the pancreas was segmented and lines were added at the cranial and caudal edges for visualization of motion between maximum inhale and maximum exhale states.

Results

Orthogonal 2D-cine MRI showed that all three corsets reduced pancreatic center-of-mass motion mainly in IS direction. Without corset, the analysis of the 2D-cine MRI showed an average pancreas motion in IS direction of 16.9 mm ± 1.7 mm (range 10.4 mm – 25.7 mm). With the corsets, this motion was substantially reduced to an average of 7.5 mm ± 1.6 mm (range 2.5 mm – 10.3 mm), 9.2 mm ± 2.6 mm (range 3.0 mm – 14.7 mm), and 8.7 mm ± 1.9 mm (range 2.9 mm – 15.0 mm) for the PU, PE and 3DPE corset, respectively. Hence, on average, the respiratory induced motion amplitude in IS direction was reduced by 56 %, 46 % and 49 % with the PU, PE and 3DPE corset, respectively. Compared to the intrafraction motion variability in IS direction in free breathing (σ = 1.7 mm), motion variability was similar for the PU (σ = 1.6 mm) and 3DPE (σ = 1.9 mm) corset and slightly increased for the PE corset (σ = 2.6 mm). The motion amplitude in AP and LR direction in free breathing was substantially smaller with 3.1 mm ± 0.8 mm in AP and 2.8 mm ± 1.1 mm in LR direction. By application of the corset, the motion amplitude in these two directions was consequently only slightly reduced to 2.1 mm ± 0.5 mm, 1.7 mm ± 0.6 mm and 1.1 mm ± 0.7 mm in AP direction and 1.1 mm ± 0.7 mm, 2.1 mm ± 1.0 mm and 1.3 mm ± 0.7 mm for LR direction

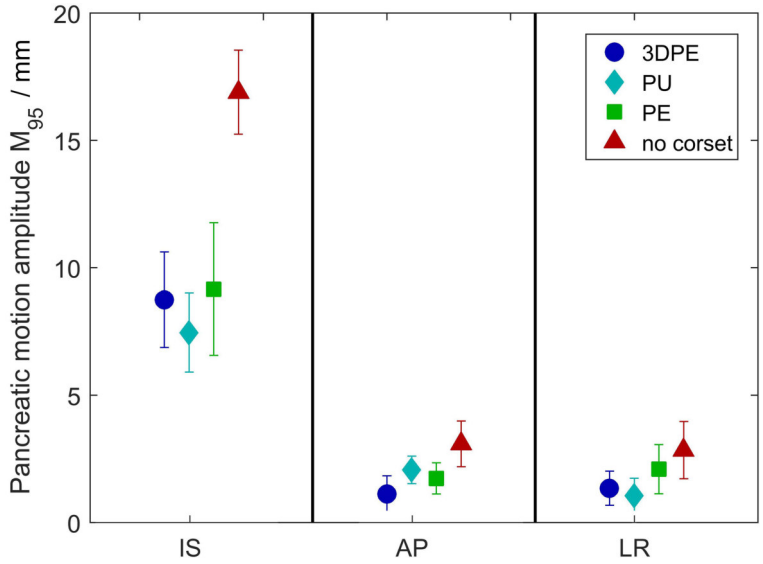

Figure 5.5: Pancreas motion amplitudes on two consecutive days extracted from coronal / sagittal 2D-cine MRI (4 images/s) of a volunteer wearing three different corsets and the reference measurement without corset. Motion amplitudes are given as averaged peak-to-peak M_{95} amplitudes, where the upper and lower 2.5 % of data was discarded to reduce the effect of outliers.
Abbreviations: 3DPE = three-dimensional-scanned polyethylene, PU = polyurethane, PE = polyethylene.

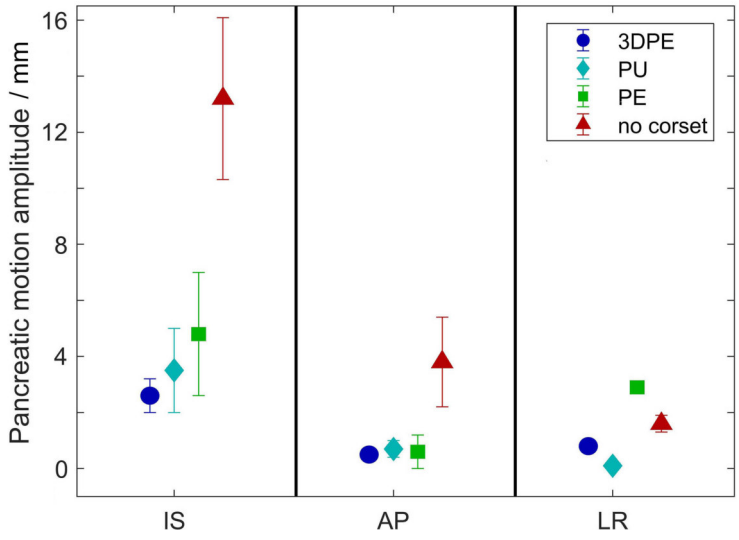

Figure 5.6: Average center-of-mass motion of the pancreas in inferior–superior (IS), anterior–posterior (AP) and left–right (LR) direction with the PU, PE and 3DPE corsets and without corset extracted from 4D-MRI. The error bars represent the range of motion on the two consecutive days on which the measurements were performed.
Abbreviations: 3DPE = three-dimensional-scanned polyethylene, PU = polyurethane, PE = polyethylene.

for the PU, PE and 3DPE corset, respectively. When wearing either of the corsets, the breathing frequency increased, leading to a mean length of breathing cycles of 3.2 s ± 0.4 s, 3.3 s ± 0.6 s, and 4.6 s ± 1.1 s for the PU, PE and 3DPE corset, respectively, instead of 7.1 s ± 0.7 s without corset. The summarized results of the motion as measured in orthogonal 2D-cine MRI is shown in Figure 5.5.

4D-MRI was in accordance with the results found in 2D-cine MRI in that all three corsets reduced pancreatic center-of-mass motion mainly in IS direction but also reduced motion in AP direction substantially as well as increased the interfraction motion variability in these two directions. IS motion was found to be on average 3.5 mm ± 1.5 mm, 4.8 mm ± 2.2 mm and 2.6 mm ± 0.9 mm with the PU, PE and 3DPE corset, respectively, as opposed to 13.2 mm ± 2.9 mm without corset. In AP direction, the mean amplitude was reduced from 3.8 mm ± 1.6 mm without corset to 0.7 mm ± 0.3 mm, 0.6 mm ± 0.6 mm and 0.5 mm ± 0.2 mm with the PU, PE and 3DPE corset, respectively. In LR direction, mean amplitudes without corset of 1.6 mm ± 0.3 mm were observed, which were decreased by the PU and 3DPE corset to 0.1 mm ± 0.1 mm and 0.8 mm ± 0.1 mm and increased by the PE corset to 2.9 mm ± 0.2 mm. The detailed values are illustrated in Fig. 5.6.

5.1.4 Discussion

All three corsets evaluated in this study reduced respiratory induced pancreatic motion, in particular in IS direction. Compared to the study by Heerkens *et al.* (2017), investigating the pancreatic motion reduction for 10 patients by use of a PU corset based on orthogonal single-slice 2D cine MRI and reporting a mean IS motion reduction of 4.1 mm (36 % reduction), in this study pancreatic motion reduction based on orthogonal 2D-cine MRI yielded a reduction of 8.4 mm (50 % reduction) in IS direction by use of three different corsets in a single healthy subject.

In this study, pancreatic motion reduction was also analyzed based on 4D-MRI, which revealed a motion reduction of around 9.6 mm (73 % reduction) in IS direction. While 4D-MRI is volumetrically more reliable than orthogonal 2D-cine MRI, since it includes the full volume of the pancreas, it can be affected by the resorting algorithm. Furthermore, the 4D-MRI acquisition requires a longer acquisition time and hence includes more respiratory cycles. Lastly, since image quality in 4D-MRI is degraded relative to single-slice 2D cine MRI, segmentation is more prone to errors and could distort the results. These funda-

mental differences between the two image modalities could explain the difference in mean pancreas motion found between orthogonal 2D-cine and 4D-MRI.

Additionally, a noticeable AP motion reduction of 3.2 mm (84 % reduction) was observed in 4D-MRI, as well as 1.5 mm (47 % reduction) in 2D-cine MRI, whereas in the previous study by Heerkens *et al.* (2017) no motion reduction was observed. As reported by other studies analyzing respiratory induced motion reduction by abdominal compression (Fontana *et al.*, 2016; Heerkens *et al.*, 2017; Dolde *et al.*, 2019b), such results are highly patient-specific with a large inter-patient variability. Since only one healthy subject was included in this study, the magnitude of motion reduction found should not be generalized but understood in the context of a feasibility study.

Moreover, as opposed to the corset design presented in this study, covering the ribs and abdomen in order to reduce both abdominal respiratory motion and chest breathing, the corset used by Heerkens *et al.* (2017) left out the ribs to promote chest breathing. It is therefore likely that these differences in corset design may contribute to the divergence in observed motion reduction patterns. One has to note, that for free-breathing the volunteer was scanned with the anterior coil positioned directly on his chest since no coil holder setup was available for this scanner. This could have influenced the amount of respiratory motion in the reference scan. On the other hand, care has been taken that the already light weighted coil was not compressing the volunteers chest to minimize its affect on respiration.

While 2017 (2017) aimed for a utilization of the corset in stereotactic XT, the focus in this study was on its applicability for PT, for which constant and reproducible corset thickness and homogeneity are more critical than for XT. With regard to the material properties, both the PE and the 3DPE corset showed potential to be used in PT since they have a constant thickness and are made of a homogeneous material with WER values similar to adipose tissue (Möhler *et al.*, 2018). From a manufacturing point of view, the 3DPE corset is more time-consuming and hence also more costly as a consequence of the additional necessary working hours by a trained technical orthopedic staff. This, on the other hand, allows for flexibility in the design and hence a positioning of corset opening and buckles that does not collide with intended treatment beam directions, in order to avoid beam edge effects where imperfect reproducibility of positioning leads to under- or over-shoot of the proton beam. Although the treatment planning system will take the resulting range shifts into account and robust treatment planning can partially compensate for imperfect reproducibility in positioning, shifts in patient position relative to the edges will impact the range of the

traversing beam and should be avoided if possible. The design of the 3DPE corset considered that beam angles between 40°–100° were *a priori* not intended for pencil beam scanned PT planning since the presence of the stomach and the large intestine prevents the usage of left lateral (oblique) beam angles for pancreatic patients in our institutes due to the otherwise strong density changes the beam path (Batista *et al.*, 2017; Stefanowicz *et al.*, 2018). Hence, the left lateral part was chosen as an opening. The PE corset, on the other hand, shows partially overlapping material layers at the anterior side, where the four hook-and-pile fasteners are placed (see Figure 5.1). Since for this corset the opening is fixed by design, it compromises the use of anterior beams, since edge effects may occur due to the fact that the beam will pass across edges of the corset layers or the closing buckles. In order to minimize the impact of air gaps on beam penumbra, the corset should closely match the patients' skin surface. However, since no CT scan of the healthy volunteer wearing the corset could be acquired, the fitting accuracy of the corset to the body surface could not be investigated.

The WER measurements show that both PE corsets with their WER of 0.956 – 0.991 as well as the PU corset with a WER of 0.298 would have an impact on the range shifts in PT, and hence need to be included in the treatment planning. The measured WER showed to be constant for the two proton beam energies used, which is in good agreement with literature (Palmans and Verhaegen, 1997; Akbari *et al.*, 2014). The PU corset showed pronounced wrinkles, air cavities and a variable thickness throughout the whole corset. In collaboration with two experienced orthopedic technicians the manufacturing of the PU corset was slightly varied with different volunteer positioning to thereby produce a corset with a more constant thickness and reduce air inclusions. Since after three attempts no improvements were observed, the idea of creating a homogeneous PU corset was discarded. Depending on the size of air cavity in the beam path, this heterogeneity could lead to range shifts from 1.3 mm – 7.6 mm for varying corset thicknesses of 4.2 mm – 25.6 mm. For XT, these drawbacks would have no detrimental effect on dose deposition, besides an increased skin dose by the corset that needs to be considered (Heerkens *et al.*, 2017). For XT purposes, the use of the PU corset would hence allow for a patient-individualized solution, which has low manufacturing costs and lead time. For PT, the air inclusions in the PU corset make it unsuitable, since the resulting range shifts lead to increased range uncertainties (Paganetti, 2012).

The difference in measured thickness between the PE-based sample used for WER de-

termination and the corsets themselves is partially influenced by the different measurement procedures. While the thickness of the samples was measured 15 times around their center with a caliper, it was determined as full width at half maximum (FWHM) values in the respective CT scans for the corset at 15 different positions. Due to the pixel width of 0.8 mm in the CT scans, the determination of the small corset thicknesses might be distorted. Furthermore, the discrepancy of the measured thickness of the 3DPE corset and the samples used for WER measurements results from the thermoforming process underlying the corsets manufacturing. This leads to a decreased thickness of the thermoformed corset relative to its base material used as sample.

For fractionated radiation treatment of patients with pancreatic carcinoma, it is well-known that intra-abdominal anatomy changes occur from day to day, depending on the filling of the stomach and bowel (Van der Horst *et al.*, 2013). Moreover, substantial weight loss has been observed in these patients during the course of treatment (Naumann *et al.*, 2013). These factors compromise the setup reproducibility and may require the corset pressure to be adjusted between treatment fractions in order to secure adequate immobilization. This study has shown that pancreatic motion reduction obtained with patient-individualized corsets is similar to that of the semi-specific corset. Therefore, semi-individualized corsets may be sufficient, which would have the advantages of re-usability and shorter manufacturing time. Still, substantial inter-patient variability has to be expected. This variability may depend on natural breathing patterns (i.e. chest or abdominal breathing), the size and location of the primary tumor, and its infiltration into surrounding tissues. Therefore, a comparative study with a large patient cohort is mandatory to get good statistics and analyze subgroups.

From a logistic point of view, the construction and adjustment of the PE and 3DPE corsets requires the cooperation with an orthopedic institution and the technical infrastructure. On the other hand, the PU corset can be produced by the clinical staff, after an initial training. While the PU and non-individualized PE corsets required only 30 min of adjustment time, for the 3DPE-corset a manufacturing time of 3 days were needed, which also scales with the costs of these corsets.

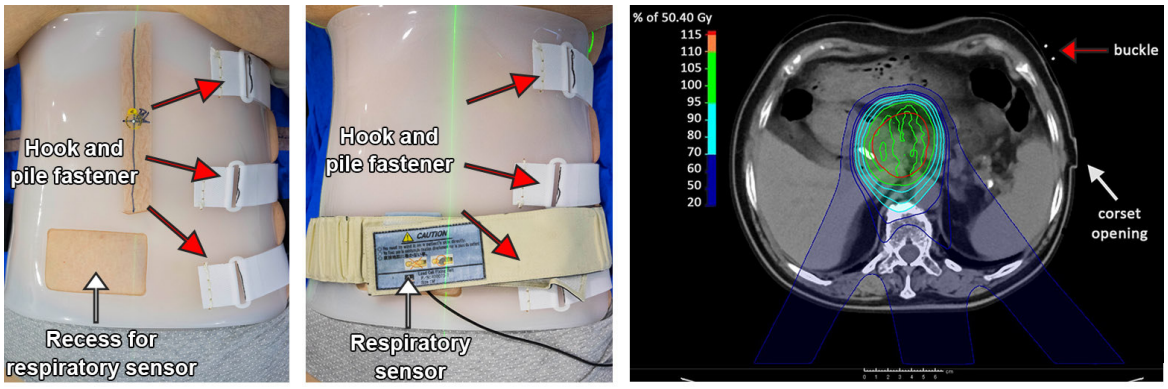

(a) (b) (c)

Figure 5.7: (a-b) Patient positioned in a vacuum mattress for acquisition of a 4D planning CT wearing the 3DPE corset. A recess (white arrow in (a)) is incorporated into the corset for positioning of a respiratory sensor (white arrow in (b)) for 4D CT reconstruction. (c) Example of a delivered proton therapy plan (robustly optimized scanned pencil beam) of a patient with a carcinoma of the pancreatic head wearing the 3DPE corset. Three beam angles were applied (140°, 170°, 208°) to accumulate a dose of 50.4 Gy within 28 fractions in the internal clinical target volume (red contour). The buckle of the corsets hook-and-pile fasteners and the corset opening are marked (red arrow in (c)). Beam angles penetrating these structures (40°–100°) were avoided.

5.2 3DPE corset for patients with abdominal cancer

5.2.1 Clinical implementation of 3DPE corset

For the implementation of the 3DPE corset in the existing clinical workflow for PT of abdominal cancer patients, several requirements had to be considered in the design of the corset. In our clinic, the treatment planning of moving tumors is based on 4D CT, where for its retrospective reconstruction the respiratory signal is extracted by use of a pressure sensor using the Anzai respiratory gating system (Anzai Medical Co., Ltd., Tokyo, Japan). The initially tested strategy in which the sensor was positioned above the corset on the patients upper right chest led to a poor performance of the sensor. Hence, a recess of $10 \times 6\,\mathrm{cm}^2$ was incorporated into the corset at the lower right abdomen caudally of the umbilicus (see Figure 5.7 (a)), which facilitated the use of the pressure sensor as typically performed without a corset by the medical technical assistance staff.

The cranial end of the corset was positioned at the height of the xiphoid process in order to omit the breasts of the patient from the corset, due to their tendency towards variability, which can hamper reproducible tightening of the corset but still include the lower four ribs to reduce of both chest and diaphragmatic breathing. As discussed in section 5.1.4 and illustrated in Figure 5.7, the corset was designed such as that both the buckles of the hook-

and-pile fasteners as well as the corset opening were placed laterally left of the patient to not interfere with the applied PT beams. With this design, a potential positional variability of the buckles and opening would have no disturbing effect on the dose distribution during PT. In order to allow for reproducible tightening of the corset, marks were drawn on the fastener when the corset was first applied during acquisition of the planning CT scan. To avoid covering of the fastener by the vacuum mattress, the buckles had to be positioned anterior of the patient's mid-plane without colliding with a potential anterior-posterior proton beam (0°).

Based on the results of the material analysis in section 5.1.1, it was shown to be sufficient to directly transform the measured CT values of the planning CT scan to WER values with the clinically used Hounsfield look-up table. This was due to the adipose tissue equivalency (Möhler *et al.*, 2018) of both CT values (- 107 HU $\pm$ 32 HU) and WER values in proton irradiation (0.991 $\pm$ 0.002) in combination with the small and constant corset thickness of 3.8 mm $\pm$ 0.2 mm. An already conservatively estimated error of 10 % in the translation of HU to the stopping power would consequently only lead to a maximum error of 0.38 mm in the proton range prediction. In Figure 5.7, a clinically applied PT dose distribution is shown, where a patient with a carcinoma of the pancreatic head was irradiated with three proton beams with angles between 140°– 208° to deposit a dose of 50.4 Gy within 28 fractions to the internal clinical target volume (iCTV).

5.2.2 Pancreas motion reduction by use of an abdominal corset

Methods

To assess the reduction of respiratory induced pancreas motion, a clinical study was conducted including patients with abdominal cancer (pancreas, gallbladder, liver). The study, which was initially designed to solely include pancreas cancer patients, was extended to other abdominal cancer patients due to an otherwise insufficient acquisition rate. Still, the motion of the pancreas was still analyzed for patients with all three tumor sides and the consequential heterogeneity of the patient cohort was accepted. The study was approved by the local Ethics Committee of the Faculty of Medicine and University Hospital Carl Gustav Carus of the Technische Universität Dresden (EK-398092016). 16 patients provided informed written consent for the manufacturing of a patient-individualized abdominal corset and for performing an MRI scan with a protocol combining diagnostic pulse sequences with

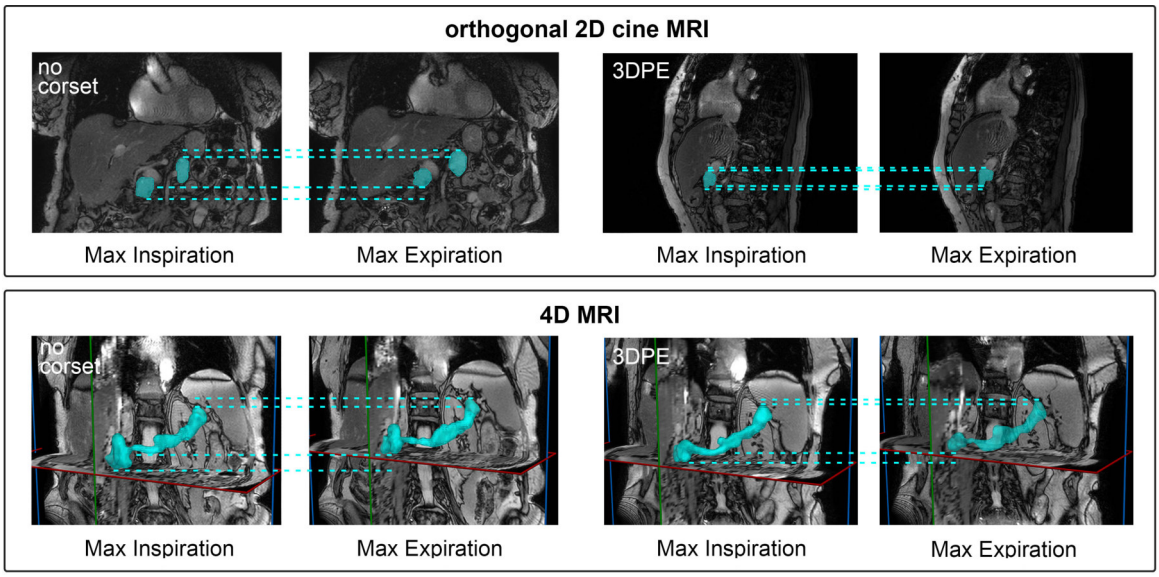

Figure 5.8: Orthogonal (coronal and sagittal) single-slice 2D-cine MRI (*top*) and 4D-MRI (*bottom*) of patient in free breathing (*left*) and wearing the 3DPE corset (*right*) showing the state of maximum expiration and inspiration. The pancreas is segmented and lines are added at the caudal and cranial edge of the pancreas to visualize the amount of pancreatic motion.

pulse sequences for motion characterization.

Out of the 16 patients included in the study, 1 patient dropped out of the study due to cancer related death before a CT or MRI scan could be acquired and for 2 patients it was decided to not perform an MRI scan due to their hip implants. Although the presence of MR-compatible hip implants was no exclusion criteria per se, in one case no technical data of the implant could be provided in time while in the second case the implant set a limit on the product of specific absorption rate (SAR) times acquisition time that could not be met with our combined diagnostic and study related MR protocol without risking an unacceptable temperature increase. Of the resulting 13 patients scheduled for MRI, 1 MRI scan had to be aborted due to severe claustrophobia of the patient. Furthermore, 3 patients did not fit in the MR scanner, as it was modified for RT compatibility. These patients were scanned in the MR scanner without coil holder, as a consequence of which the anterior MRI coil was positioned directly on the patient. Their MRI data was not included in the motion analysis since effectively no reference scan during free breathing was acquired. Consequently, in the motion analysis 9 patients were included (3 male and 6 female; average age 72.9 ± 9.6 years). Out of these 9 patient datasets, for 2 patients the reconstruction of the 4D-MRI dataset (initially based on radial k-space sampling) did not result in images with a suffi-

cient quality for analysis. During the transition towards the multi-slice based 4D-MR pulse sequence used in this study, the MR protocol was adapted which lead to erroneously not acquiring the orthogonal 2D-cine MRI dataset for one patient. Hence, while 8 patients were evaluated by use of 2D-cine MRI only 7 patients were evaluated by use of 4D-MRI.

To quantify the reduction of respiration-induced pancreatic motion by use of the 3DPE corset the included patients were scanned on a flat-table top overlay (Medibord Ltd, Nottingham, UK) with a 3.0 T MR scanner (Philips Ingenuity TF PET/MR scanner, Philips Healthcare, Eindhoven, The Netherlands) using a 32-channel SENSE Torso/Cardiac coil. The MRI pulse sequences for motion analysis were acquired first with the patient wearing the corset. Directly afterwards, the corset was removed and the patient was scanned in free breathing to acquire a reference dataset. Subsequently, diagnostic MRI sequences (T_2-TSE, DWI, T_1-GRE with contrast agent) of approximately 20 min scan time were acquired to aid the contouring by the radiation oncologists and check for a potential metastatic spread of the tumor. The anterior and posterior parts of the coil were positioned around the patient with a coil holder system. Unlike in RT, the patients arms were positioned next to the body, since a positioning of the arms superior to the head could not be realized due to the limited space in the 60 cm diameter bore of the MRI scanner.

The patients underwent orthogonal single-slice 2D cine MRI in coronal and sagittal orientation at a frame rate of approximately 2 Hz (field of view = 375×375 mm², resolution = 1.0×1.0 mm², slice thickness = 7 mm, bandwidth = 1929 Hz/pixel, TE = 1.1 ms, TR = 2.2 ms, flip angle = 27 °, acquisition time = 1 min) for the assessment of the mean pancreas motion as well as its intrafraction motion variability. As measure of intrafraction motion variability, the standard deviation of the peak-to-peak pancreas motion amplitude was determined by manual segmentation of the pancreas over several respiratory cycles and determination of its center-of-mass motion. Furthermore, a 4D-MRI dataset was reconstructed for an averaged 3D motion assessment of the full pancreas volume over several breathing cycles by retrospectively binning a multi-slice 2D-cine MRI acquisition (field of view = $375 \times 375 \times 120$ mm³, resolution = 1.0×1.0 mm², slice thickness = 5 mm, bandwidth = 1929 Hz/pixel, TE = 1.1 ms, TR = 2.2 ms, flip angle = 27 °, acquisition time = 9 min) to 10 respiratory phases with differentiation between mid-inhale and mid-exhale phases. The resorting algorithm was based on the method described by Von Siebenthal *et al.* (2007). However, instead of acquiring a navigator slice in between every two image slices, the reconstruction in this study was performed with an image-based navigation method. There-

fore, the continuously acquired parallel coronal 2D images of a 3D volume with 50 dynamics were resorted based on the position of the dome of the liver in each MR image. This position was retrieved from a non-rigid registration of the respective dynamics using the open source software ANTs (Avants *et al.*, 2008; Avants *et al.*, 2014). This provided the information about the respiratory state, necessary for the 4D-MRI reconstruction. On each 4D-MRI data set, the pancreas was manually delineated on the end-inhale and end-exhale images using the open-source software MITK. The center-of-mass of these delineations was determined to estimate pancreatic motion in IS, AP and LR directions. No specific breathing instructions were given to the patients. The MRI scan was only performed once before the start of treatment. An assessment of the interfraction motion variability was therefore not performed.

Exemplary images of 2D-cine and 4D-MRI are shown in Figure 5.8 where the pancreas is segmented in maximum exhale and maximum inhale.

Results

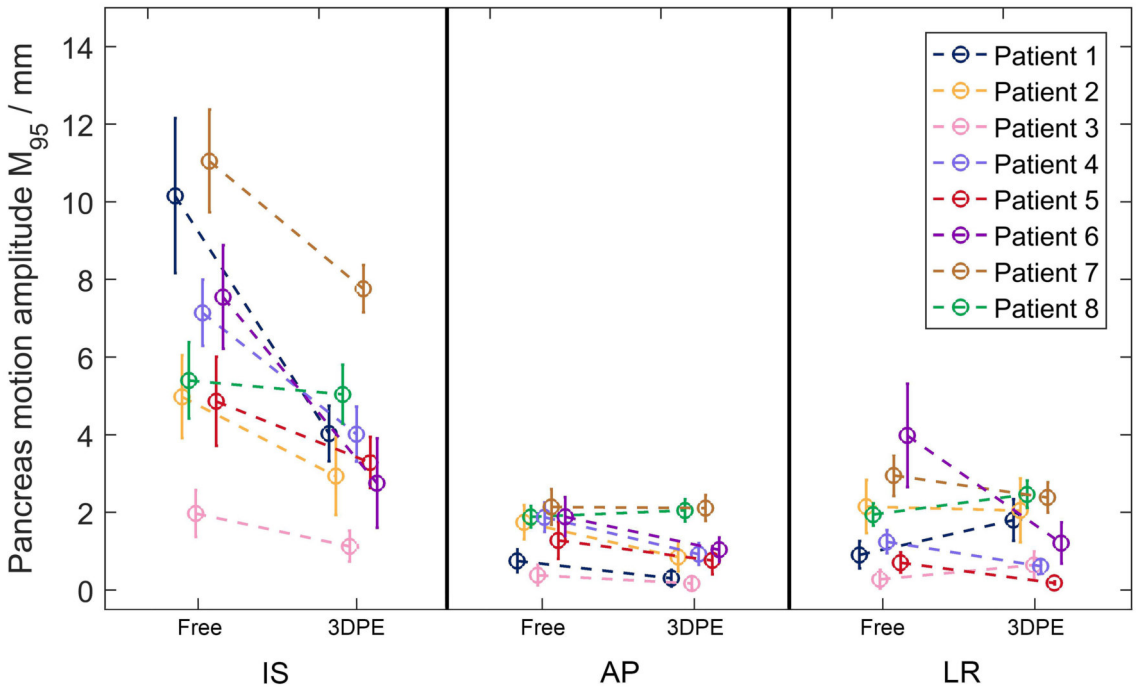

Figure 5.9: Mean center-of-mass motion amplitude M_{95} of the pancreas in inferior–superior (IS), anterior–posterior (AP) and left–right (LR) direction in free breathing and with the 3DPE corset for 8 patients as determined by orthogonal single-slice 2D-cine MRI.

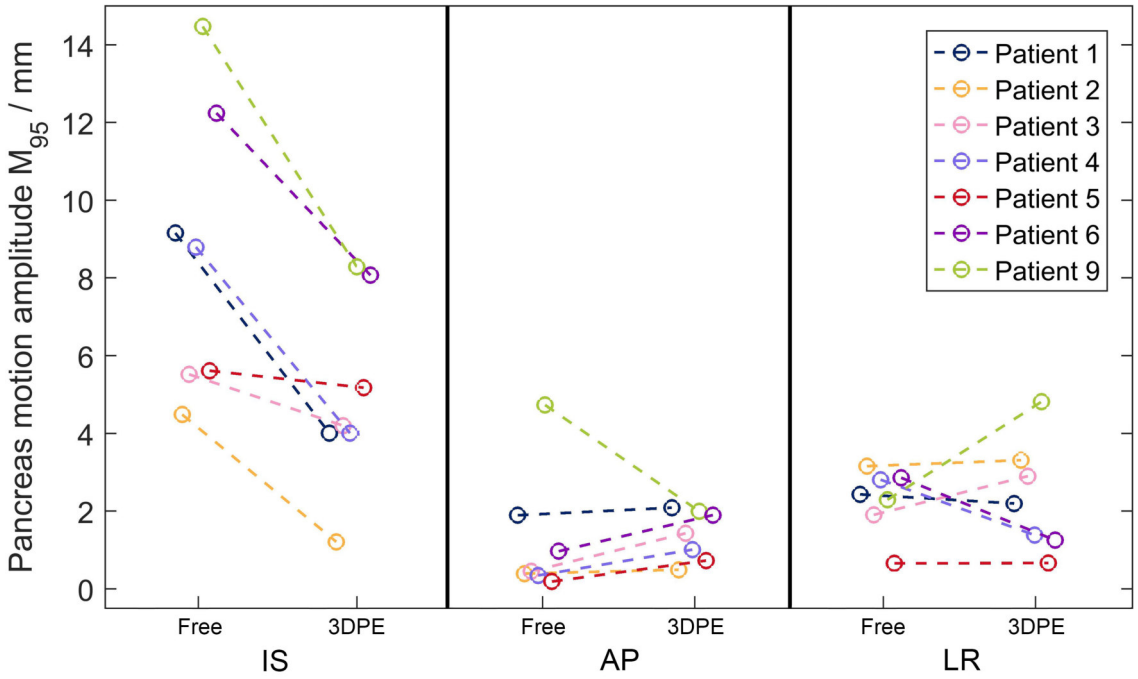

Figure 5.10: Center-of-mass motion of the pancreas in inferior–superior (IS), anterior–posterior (AP) and left–right (LR) direction with the 3DPE corsets and without corset for 7 patients as determined by 4D-MRI. For Patient 9 no orthogonal single-slice 2D-cine MRI was acquired and for Patient 7 & 8 no 4D-MRI dataset was acquired.

Motion assessment based on orthogonal 2D-cine MRI revealed that pancreas motion was mainly found in IS direction and was reduced in IS direction by 2.8 mm (42 % reduction, $p < 0.05$) when the abdominal corset was applied from in average 6.5 mm $\pm$ 3.7 mm in free breathing to 3.8 mm $\pm$ 1.1 mm with the corset. Here, the stated standard deviation combines both the measured inter-patient motion variability as well as intra-patient motion variability. The patients intrafraction motion variability decreased from 1.5 mm in free breathing to 0.9 mm ($p < 0.01$) when the corset was applied. Pancreas motion in AP and LR direction was small in free breathing with 1.5 mm $\pm$ 0.2 mm in AP and 1.8 mm $\pm$ 0.7 mm in LR direction and consequently not substantially influenced by the use of the corset with 1.0 mm $\pm$ 0.1 mm (31 % reduction, $p < 0.05$) in AP and 1.4 mm $\pm$ 0.3 mm (20 % reduction, $p > 0.05$)in LR direction. Combining all directions, the corset reduced motion in 3D from 7.1 mm $\pm$ 4.4 mm to 4.4 mm $\pm$ 1.5 mm (39 % reduction).

Motion assessment based on 4D-MRI showed a generally higher pancreas motion in IS direction relative to the motion amplitude found in 2D-cine MRI. Motion in IS direction was reduced by 3.6 mm (42 % reduction, $p < 0.05$) when the abdominal corset was ap-

plied from in average 8.6 mm ± 3.7 mm during free breathing to 5.0 mm ± 2.4 mm with the corset. Pancreas motion in AP and LR direction was again small during free breathing with 1.3 mm ± 1.6 mm in AP and 2.3 mm ± 0.8 mm in LR direction and consequently not significantly influenced ($p > 0.05$) by the use of the corset with 1.3 mm ± 0.6 mm in AP and 2.4 mm ± 1.4 mm in LR direction. Combining all directions, the corset reduced motion in 3D from 9.1 mm ± 3.5 mm to 5.9 mm ± 2.1 mm (35 % reduction).

5.2.3 Patient acceptance of abdominal corset

After manufacturing of the 3DPE corset and the acquisition of both the planning CT scan and the MRI scan the patients were asked to fill out a questionnaire assessing the level of discomfort in six questions. At this point in time, the patients wore the corset for approximately 5 minutes during manufacturing, 30 minutes during CT scanning and 20 minutes during MRI scanning. 13 patients were asked to fill out the survey, which includes four patients who wore the corset during MRI but were not included in the motion analysis in section 5.2.2. The results can be seen in Figure 5.11. The corset was generally well tolerated with on average no complaints or no pain in all categories. In only one patient slight discomfort during the manufacturing was found and in one patient slight discomfort was found regarding breathing ability and the general feeling of pressure during CT and MRI

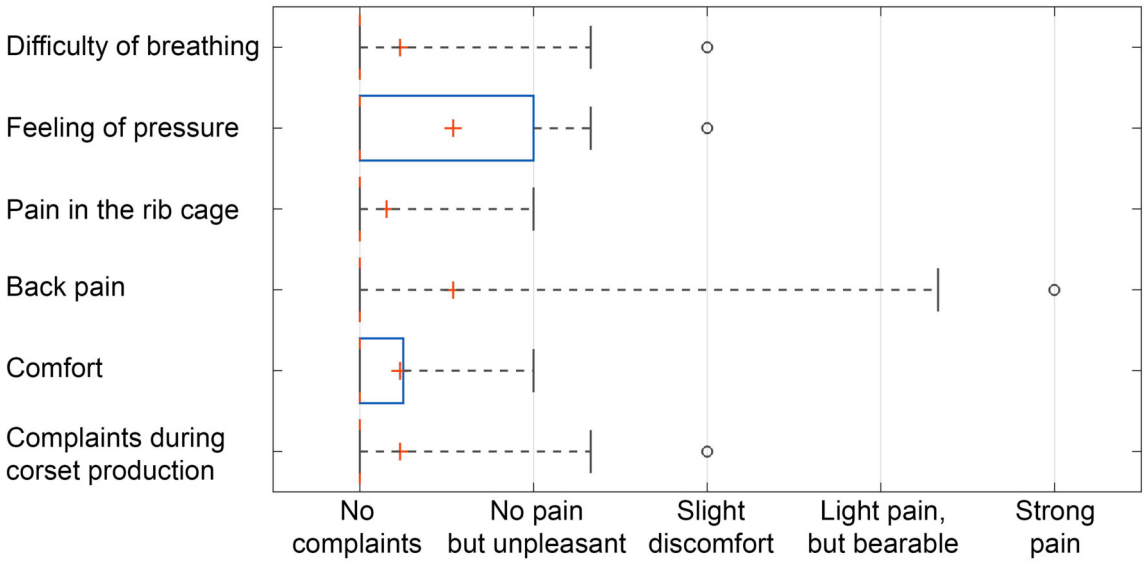

Figure 5.11: Results of survey analyzing the patient acceptance of abdominal corset after manufacturing and wearing the abdominal corset during planning CT and MRI, including 13 patients.

scanning, respectively. Two patients mentioned light or strong back pain. However, both patients already complained about back pain before application of the corset, indicating that the pain was probably not related to the corset.

5.2.4 Discussion

While the 3DPE corset was successfully implemented in the PT workflow of 13 patients with abdominal cancer several challenges and limitations should be noted. Due to the relatively high thickness of the 3DPE corset material ($\sim$4 mm) and its consequential inflexibility, its use for patients who's weight significantly changes in between treatment planning and dose delivery has been shown to be laborious and led to one case (male patient with hepatocellular carcinoma) where re-planning without corset was necessary. Considering the comparable motion reduction of the 3DPE and PE corset, as found in section 5.1, with the PE corset's thinner material and higher flexibility, the manufacturing of the 3DPE corset with thinner base materials seems promising but was not investigated.

The cranial end of the 3DPE corset was designed so that it would be positioned at the height of the xiphoid process. This position was chosen in order to omit the breasts which are heavily affected by weight gein and thereby reduce application difficulties in this scenario. This position on the other hand coincides with the dome of the liver and hence for patients with hepatocellular carcinoma may lead to a partially overlapping corset with the proton beams, potentially increasing range uncertainties. For patients with pancreatic cancer this position includes the whole target volume and hence does not pose any risk.

After initially extracting the respiratory signal during 4D CT scanning with the pressure sensor placed on the upper right chest, leading to a poor signal extraction, a recess was incorporated in the corset in order to place the sensor on the lower right abdomen. This facilitated the use of the sensor as performed without corset and was well perceived by the staff of medical technical assistants. The issue of positioning a respiratory sensor could be also resolved by a higher integration of MRI into the PT workflow, where e.g. a static CT could be registered to motion resolved MR images (Dolde *et al.*, 2018a) to gain the motion information required for personalized ITV margins. This would eliminate the need for external respiratory signal extraction, since MRI offers multiple options for respiratory signal extraction (1D-MRI navigation, self-navigation through radial k-space sampling, image-based self-navigation through body contour information). Since the MR scanner in our institute

does not allow for a positioning of the patients with their arms above their head, as performed during RT, such an integration is not feasible yet.

Hence, opposed to RT, in our study the arms of the patients were positioned next to the body, since a positioning of the arms superior to the head could not be realized in the MR scanner's 60 cm diameter bore with the additional reduction of space due to the flat-table top. This could have influenced the respiratory behavior and consequently the respiratory induced organ motion.

The pancreas motion, as measured in the patients included in the study, was found mainly in IS direction, in accordance to literature and the volunteer study, described in section 5.1.3. Both orthogonal 2D-cine MRI as well as 4D-MRI revealed a reduction of pancreas motion in IS direction by 41 % – 42 %. Yet, the absolute motion amplitudes measured with both image modalities differed, where 4D-MRI showed larger motion amplitudes as well as a larger motion reduction by use of the corset with a reduction of 3.8 mm vs. 2.6 mm in 2D-cine MRI. This divergence is affected by several factors. First, single-slice 2D-cine MRI only captures the motion of a selected volume. Furthermore, this motion can be affected by through-plane motion, which can distort the real motion. 4D-MRI includes the full volume of the pancreas and is hence not affected by through-plane motion. On the other hand, the reconstruction algorithm used for 4D-MRI in the patient study has the tendency to overweight deep-inspiration states, that would potentially be discarded as outliers in the M_{95} motion analysis based on 2D-cine MRI. No data is discarded in the 4D-MRI reconstruction and for every slice the maximum state of inspiration and expiration is determined individually based on the cranio-caudal position of the dome of the liver. This effect is partially compensated by the larger volume over which the pancreas motion was determined in 4D-MRI but could influence the results towards larger motion amplitudes. Additionally, the limited image quality of the reconstructed 4D-MR images can influence segmentation and hence distort the measured pancreas motion. While 2D-cine MRI only gives information about a selected volume with potential distortion due to through-plane motion, it is a real-time imaging modality that is not affected by resorting errors. Finally, only 6 out of the 9 patients were included in both 2D-cine and 4D-MRI evaluation, whereas 2 patients were included in the 2D-cine MRI analysis with no 4D-MRI available and 1 patient was included in the 4D-MRI analysis with no 2D-cine MRI available.

In general, however, the results from both image modalities conclude that pancreas motion is mainly found in IS direction and is reduced by the use of an abdominal corset by

$\sim$ 41 %. The free breathing pancreas motion found in the patient cohort (8.6 mm (4D MRI) / 6.6 mm (2D-cine MRI) in IS direction) was substantially smaller than the motion found in the healthy volunteer (13.2 mm (4D-MRI) / 16.9 mm (2D-cine MRI) in IS direction). This also reduced the potential absolute motion reduction by use of an abdominal corset which scales with the initial pancreas motion found in free breathing condition. In our study 4 patients showed free breathing motion amplitudes in IS direction < 6 mm, as measured with 2D-cine MRI. For those patients the corset only reduced motion by 1.2 mm whereas the other 4 patients showed a larger pancreas motion which was reduced by 4.6 mm. This corresponds in 4D-MRI to 3 patients with free breathing motion amplitudes in IS direction of < 6 mm which was reduced by 1.7 mm by use of the corset and 4 patients with amplitudes in IS direction of > 6 mm which was reduced by 5.2 mm. This underlines the significance of inter-patient variability. A strategy for a selection of suitable patients for the manufacturing of a patient individualized abdominal corset is therefore advised.

How to select patients eligible for wearing a corset during the course of radiation therapy is an open question. A previous study with liver tumor patients furthermore reported on dosimetric benefits of abdominal compression using a pressure belt for moderate and large tumor motion amplitudes > 7 mm in pencil beam scanning PT (Lin *et al.*, 2017). For patients with initially small tumor motion of < 7 mm, however, abdominal compression was found to be needless. In the AAPM task group 76 report (Keall *et al.*, 2006) a slightly more conservative limit of < 5 mm is stated, under which motion is considered insignificant enough that no respiratory management is required. However, this report does not explicitly address PT. Furthermore, the selection of suitable patients may depend on the tumor infiltration, the patients' condition and willingness to tolerate the abdominal pressure during repeated imaging and irradiation fractions.

The results of the survey filled out by 13 patients included our study showed that the corset is well tolerated with generally no complaints or no pain felt. This includes patients who underwent EUS guided fine-needle aspiration for injection of fiducial markers within 5 days before application of the corset. Only two patients complained about back pain, however, for both patients this back pain was present before application of the corset. At least in one of those patients, the pain was likely cancer related due to its infiltration into the aorta and vertebrae. It has to be noted, however, that the level of discomfort scales with the pressure that is applied with the corset. Since the corset pressure was applied in coordination with the patients, the level of pressure was naturally limited by the patients

tolerance and is reflected in the results.

Lastly, the need of abdominal compression could be resolved by the implementation of gating or tracking strategies in PT. However, while for XT a synchronized anatomical imaging and radiation is available, e.g. by use of MR-Linacs, in PT gating or tracking strategies can to date only be applied by extraction of respiratory information through external surrogates like pressure sensors or optical body contour scanning. The correlation of external surrogates to target motion is, however, questionable.

Furthermore, respiratory gating techniques increase the treatment time particularly in intensity modulated RT where gating can lead to a 4- to 15-fold increase in delivery time. (Keall *et al.*, 2006). Highly increased delivery times correlate to the likelihood of patient movement and have been suggested to reduce tumor control due to the increased intrafraction repair of sublethally damaged tumor cells. Live target tracking, on the other hand, is only sparcely available (e.g. CyberKnife (Snider *et al.*, 2012)) due to an insufficient speed of synchronizing imaging with the treatment beam.

5.3 Summary

In this study the use of a patient individualized abdominal corset for MR guided PT of patients with abdominal cancer was investigated and implemented in PT for the first time in the frame of a clinical study. First, three different types of MR compatible abdominal corsets were investigated regarding their applicability in PT. While the effect on respiratory induced motion reduction was comparable for all three, their material properties and manufacturing procedure differed substantially. The corset that requires the least additional effort in manufacturing and that has already been used in XT (Heerkens *et al.*, 2017) was found to be not suitable for PT due to its inhomogeneous material properties. Hence, a patient individualized PE corset was selected that on the one hand requires several days of manufacturing by trained orthopedic technicians but on the other hand can be implemented in PT without the risk of increasing inaccuracies in dose deposition.

As a second step, the abdominal corset was implemented into the clinical PT workflow in our institute for 13 patients with abdominal cancer, where the corset was well tolerated and did not induce strong discomfort. The MRI-based assessment of respiratory induced motion reduction in 9 patients through the use of the corset revealed that its application reduces 3D

pancreas motion in average by 37 % from 9.1 ± 3.5 mm to 5.9 ± 2.1 , as measured by 4D-MRI, or 38 % from 7.1 ± 4.4 mm to 4.4 ± 1.5 mm, as measured by orthogonal 2D-cine MRI. The main direction of motion was thereby in IS direction. The amount of motion reduction, however, strongly correlates with the magnitude of motion in free-breathing. Consequently, a general implementation of such individualized corsets into PT seems to be not justified when considering the additional time and costs required, but is rather only suggested for patients with initially large amount of respiratory induced motion. How to best select suitable patients for wearing a corset during the course of RT was not investigated and remains an open question.

6 General discussion and future perspectives

The aim of this thesis was to investigate and develop methods for the management of inter- and intrafraction motion for MR guided PT of PDAC. Three main hypotheses were therefore tested in this thesis.

Firstly, it was hypothesized that a novel liquid fiducial marker (BioXmark®) is detectable in MRI tumorous pancreas tissue while reducing the image distortion relative to commonly used solid fiducial markers. A utilization of BioXmark® *in vivo* was, however, not possible due to the pending CE certificate. Therefore, a gel phantom was designed that mimicked the relaxation behavior of pancreas tissue at 3 T MRI. With 4 BioXmark® markers and 7 solid fiducial markers (Gold Anchor™, VisiCoil™) placed inside this phantom, the visibility and artefacts of the markers were quantitatively assessed and compared through MR relaxometry. Furthermore, the MRI visibility of BioXmark® was tested for the first time in *ex vivo* tumorous pancreas resection specimens to assess the marker's gelation in human pancreas tissue.

Secondly, for intrafraction motion mitigation an MR compatible patient-specific corset was developed for the use in PT and implemented within the framework of a clinical study. It was hypothesized that such a corset reduces the respiratory induced pancreas motion, is tolerated well by patients with abdominal tumors and is suitable for a safe implementation in PT. As a preparatory step, three different types of abdominal corsets were tested regarding their suitability for PT. Subsequently, a clinical study in 13 was conducted with one of these corsets patients to analyze the reduction of respiratory induced pancreas motion by use of time-resolved 2D-cine and retrospectively resorted 4D-MRI on a diagnostic 3.0 T MRI scanner.

Thirdly, to assess the accuracy of motion depiction provided by the diagnostic 3.0 T MRI scanner, it's motion tracking performance had to be first evaluated with ground truth measurements. Hence, a 4D-MRI motion phantom was commissioned for QA purposes. It was hypothesized that a 4D-MRI motion phantom designed for an hybrid MR-Linac system can be implemented at a diagnostic MRI scanner and used therein for QA of motion estimation

based on time-resolved 2D-MRI and retrospectively resorted 4D-MRI. For this, a positioning and fixation setup was designed and software tools for an automatic assessment of phantom target tracking accuracy and 3D geometric fidelity were developed. Motion depicting MR pulse sequences and a clinically used 3D sequence were assessed regarding their motion tracking performance and geometric fidelity.

A recapitulation and reflection of the results of this thesis and future perspectives are discussed in this chapter.

6.1 Liquid fiducial marker for interfraction motion management in MR guided PT

Residual patient setup errors in IGRT have been shown to be reduced by the use of solid fiducial markers in patients with PDAC (Varadarajulu *et al.*, 2010; Van der Horst *et al.*, 2013). However, solid markers as utilized in image-guided XT can significantly perturb the local dose distribution in PT (Newhauser *et al.*, 2007; Giebeler *et al.*, 2008; Habermehl *et al.*, 2013). Furthermore, they are either poorly visible in MRI or are visible due to a large difference in magnetic susceptibility relative to the surrounding tissue. This leads to a correlation between visibility and image distortion in MRI (Gurney-Champion *et al.*, 2015) and makes the MR visibility of solid markers pulse sequence dependent. Since for MR guided PT patient position verification is still performed using X-ray imaging, the visibility of fiducial markers in both imaging modalities is crucial for patients with abdominal tumors.

In this work, an injectable liquid fiducial marker, BioXmark®, which has been previously shown not to locally perturb dose distributions in PT (Scherman Rydhög *et al.*, 2017), has been investigated regarding its MRI properties at 3 T for the first time (**chapter 3**). For a quantitative analysis, MR relaxometry was performed of the marker after being implanted inside a gel phantom that mimicked the relaxation behavior of pancreas tissue. The phantom also included two types of clinically utilized solid markers (Gold Anchor™, VisiCoil™) for direct comparison. It was found that the liquid marker is visible in MRI as strong signal void (signal reduction factor $>60\,\%$) independently of the used pulse sequence when the size of the spherically gelated marker exceeds the voxel size by a factor of at least 3 times. Furthermore, it was shown that neither the liquid marker's size nor the magnitude of visibility correlates with the degree of artefacts, as was found for the other two types of solid

markers.

To confirm the results of the phantom study, an *ex vivo* study was performed. In this study 5 – 6 markers of three different size categories (20/25 μL, 50/60 μL, 100 μL) were injected in three tumorous pancreas resection specimens by the use of different needle sizes (18 G, 22 G, 25 G), respectively, resulting in 17 markers being implanted in total. Markers of all three size categories could be detected as hypointensities in both T_1 and T_2 weighted MRI. Only the injection with the 18 G needle was observed to cause marker backflow, increasing non-spherical gelation and thereby potentially deteriorating visibility. The results from the current studies and from the investigations found in literature, showed that the liquid fiducial marker has beneficial properties for use in MR guided PT relative to solid fiducial markers such as high visibility in CT and MRI, low image degradation and no dose perturbation in PT. Based on the investigated MRI characteristics, the application of BioXmark® in MR guided PT for patients with PDAC is advised using sizes of injected markers of $>50\mu$L and ≤ 22 G needles for injection.

Before BioXmark® can be clinically used, its MRI properties needed to be tested in real pancreatic tissue. Since CE certification for use in abdominal patients was missing at the time of the study, an *ex vivo* study was performed in order to investigate the visibility of the marker after gelation in human pancreas tissue. It has to be noted, however, that the gelation behavior *ex vivo* and consequently the markers visibility is likely to differ from the *in vivo* situation. An investigation of the gelation behavior in an *in vivo* environment is therefore strongly advised. This is because the gelation behavior of the marker also directly affects the possible interfraction positioning accuracy where large diffusely gelated markers would impair the accuracy of image registration. As revealed by CT in the current presented study, the non-spherical gelation lead to 4 of the total 17 markers, with volumes between 20 μL – 60 μL, being non-detectable in MRI.

Since to date X-ray based patient position verification is still a crucial step for most PT protocols, the visibility of BioXmark® in kV X-ray imaging is of utmost importance. This was, however, not yet systematically analyzed for injection sites in the upper abdomen. As a first step, it is recommended to systematically analyze the marker's X-ray visibility within a phantom study, using a suitable phantom that mimics the X-ray attenuation of abdominal organ behavior in patients. Such a study is currently being performed in our institute. Since the gelation of the marker will also affect its X-ray visibility an *in vivo* investigation is necessary before a general recommendation can be given. This should be performed as soon as

the CE certification for the use of BioXmark® in patients with PDAC has been granted.

Despite the detectability as hypointensity in MRI, BioXmark® could potentially benefit from the addition of an MR contrast agent (e.g. gadolinium) to the marker composition. This would allow for a detection of the marker as hyperintensity in T_1-w MR images and thereby possibly improving the detectability of the marker in the heterogeneous environment of pancreatic tissue. However, the addition of the high-Z element gadolinium could lead to dose perturbation in PT and hence would have to be carefully investigated by a dosimetric study.

With a potential future integration of MRI and PT into a hybrid in-beam MR-PT system, fiducial markers may not be required for accurate target position verification anymore due to the then available soft-tissue visualization in treatment position. However, the integration of MR-PT systems to in-beam MR guided PT is still in its infancy (Schellhammer *et al.*, 2018). Realized near-room MR guided PT solutions by the use of a shuttle-based transport MR systems (Bostel *et al.*, 2018), on the other hand, still require X-ray position verification in treatment position. This is why in the near future, fiducial markers will likely remain clinically relevant for accurate target positioning of patients with abdominal cancer. For these patients, BioXmark® could be a promising candidate for use in X-ray and MR image guided PT.

6.2 Geometric fidelity and accuracy of target motion tracking with MRI

Besides interfraction target motion due to positioning uncertainties and organ filling, respiratory induced intrafraction target motion is a major source of uncertainty in PT. The superb soft-tissue contrast of MRI in combination with its real-time capability makes it a promising imaging modality for motion characterization. However, the versatility of MRI comes with various sources of image distortion, stemming from different hardware components or scan protocols. Hence, organ motion characterization through MRI has to be approached with care. The accuracy and precision of dedicated MRI pulse sequences for motion tracking has to be assessed through a QA procedure that additionally allows to detect a possible drift in imaging performance over time.

Since the diagnostic 3.0 T MR scanner used in this thesis has not been utilized for organ

motion quantification studies before, its target tracking performance was not known. To assess the scanner's accuracy in target tracking, in **chapter 4** an 4D-MRI motion phantom was commissioned for use on the diagnostic scanner. Prior to the phantom's commissioning on the MR scanner, the performance of the phantom itself was evaluated by reference CT measurements. For the use on MRI, an MR compatible positioning and fixation setup was designed for reproducible positioning of the phantom on the patient couch and for the safe use of its MR-conditional actuator. Single-slice 2D-cine MRI, orthogonal 2D-cine MRI and retrospectively resorted 4D-MRI sequences for evaluation of target tracking accuracy were used, based on bSSFP sequences. Relaxometry of the movable cylinder was performed to facilitate contrast optimization in bSSFP sequences. Matlab based software tools were developed for an automatic analysis of the phantom target tracking accuracy as well as for the geometrical distortion assessment using the phantom's 3D distortion grid in order to facilitate a fast QA procedure. This is particularly recommended when new pulse sequences for motion assessment are to be implemented. A full QA protocol was, however, not established since the criteria for imaging performance in MR guided PT still have to be defined.

The geometric distortion of a clinically utilized 3D GRE sequence was evaluated showing a maximum distortion of < 1.3 mm over an elliptic cylindrical volume of $15 \times 23 \times 6$ cm^3. This agrees with the requirements for stereotactic RT of targets with a diameter of > 25 mm (Pappas *et al.*, 2017). Furthermore, based on a reference CT scan, it was shown that the motion phantom performs accurately in translational motion (IS direction) but contains an intrinsic error in rotational motion, which manifests in smaller motion amplitudes in AP and LR direction by 4 % – 11 % than pre-set. This is likely due to a small mis-positioning of the target within the moving cylinder and has to be considered when evaluating the motion tracking accuracy provided by the MRI scanner. Considering these results, the single-slice 2D-cine and orthogonal 2D-cine sequences showed a high target tracking accuracy of < 0.2 mm in all three directions for targets within a radius of 10 cm from the isocenter performing regular sinusoidal motion. Similarly, the retrospectively resorted 4D-MRI sequence showed a tracking accuracy of < 0.3 mm. These results encouraged us to use these sequences for motion characterization of patients with abdominal tumors without the necessity for a systematic geometric correction.

Despite the high geometric fidelity and tracking accuracy found for the diagnostic 3.0 T MRI scanner when using the MR-Linac motion phantom, these results cannot be fully trans-

lated to a patient scenario. Here, susceptibility induced magnetic field inhomogeneities of ~ 2 ppm (Lundman *et al.*, 2017) are typically higher than for a largely homogeneous phantom. This increases the geometric distortion when scanning patients. Moreover, opposed to the phantom target, pancreas motion patterns are described by a non-rigid motion of an asymmetric target. In single-slice 2D-cine MRI, through-plane motion of such an asymetric target can simulate a motion which is actually not present in 3D. It is therefore recommended to test the accuracy of both the scanner as well as the used motion tracking algorithms with an anthropomorphic phantom, that allows for reproducible non-rigid 3D motion patterns (Mann *et al.*, 2017).

The 3D distortion analysis performed based on the phantom's 3D grid yields high geometric fidelity of the clinically used 3D GRE sequence in accordance with the requirements for stereotactic RT of medium sized targets. However the integrated grid only allows for an analysis within 6 cm depth in IS direction. Therefore, it cannot fully replace distortion analysis based on large FOV field homogeneity phantoms (Wang *et al.*, 2004; Baldwin *et al.*, 2007), which are recommended to be used for full FOV distortion analysis.

6.3 Reduction of respiratory organ motion by use of an abdominal corset

Respiration is the main cause for intrafraction target motion affecting all abdominal organs. Although different abdominal compression techniques have been implemented in the clinical routine of RT to reduce the target motion induced uncertainty in dose application, they all come with their pro's and con's. Moreover, the techniques routinely used in X-ray guided XT are often based on body frames and pressure plates positioned on the patients stomach. These techniques, however, cannot safely be applied in MR guided PT of PDAC due to incompatible materials, possible distortion of the treatment beams or relatively large setups and hence geometrical incompatibility with the MR scanner or PT facility.

In **chapter 5** the application of an abdominal corset in PT was tested for the first time. Here, three different types of abdominal corsets (PU, PE, 3DPE) were analyzed regarding their suitability for application in PT in terms of their motion reduction capability and their effect on the treatment beam, combining the information about WER, material homogeneity and thickness. In a feasibility study with a single healthy volunteer using 2D-cine and

4D-MRI, all three corsets have been shown to reduce respiratory induced pancreas motion to a similar degree primarily in IS direction by 46 % – 56 % (7.7 mm – 9.4 mm). The PU corset, which had already been implemented in XT (Heerkens *et al.*, 2017) was, however, considered not to be suitable for PT due to its material inhomogeneity and the consequential increase in dose uncertainty. Although the material properties of the semi-individual PE corset would allow for an implementation in PT, it was excluded due to the fixed anterior opening of the corset. Limited reproducibility would lead to distortion of anterior beams, which where not excluded in our clinic for patients with PDAC.

Hence, for the clinical implementation, a patient individualized PE corset was selected that was manufactured based on an optical 3D surface scan of the patient and allowed for a flexible design of the corsets opening, buckles and size. The 3DPE corset was adapted considering several clinical requirements including the treatment position, the applied beam angles and respiratory signal extraction during planning CT scan by a pressure sensor. The corset was tested in a clinical study including 13 patients with abdominal cancer. The corset was therein fully implemented in the PT workflow including the planning CT scan, a combined diagnostic and motion characterizing MRI scan as well as in the fractionated dose delivery scheme. The corset was therein well tolerated.

The intrafraction pancreas motion reduction due to the corset was determined by means of orthogonal single-slice 2D-cine MRI and retrospectively resorted 4D-MRI. Out of the 13 successfully included patients only the MRI dataset of 9 patients was used for motion assessment. For the 4 patients not included in the motion assessment the RT compatible setup could not be used and lead to a positioning of the anterior coil directly on the patients abdomen, potentially distort their free-breathing behavior. 2D-cine MRI allowed for the analysis of the real-time pancreas motion, limited to a selected slice. It yielded information about intra-patient motion variability and the average motion amplitude, while excluding outliers. 4D-MRI, on the other hand, yielded information about the average motion of the full pancreas volume, where due to the reconstruction algorithm, no outliers where excluded, potentially leading to a slight overestimation of the average motion amplitudes. Average motion amplitudes were reduced in 3D by 37 % (3.2 mm), as measured by 4D-MRI, or by 38 % (2.7 mm) as measured by 2D-cine MRI. The pancreas showed a dominant motion in IS direction, which was consequently also the direction most reduced by the application of the corset. Furthermore, 2D-cine MRI revealed that by use of the corset, intrafraction motion variability was reduced. No dosimetric evaluation was performed to quantify the dose

reduction to healthy tissue due to the corset. Such an analysis was beyond the scope of this thesis but should be performed in future studies to further quantify its expected clinical benefit.

The motion reduction capability of the 3DPE corset matches the motion reduction capability of a PU corset found by Heerkens *et al.* (2017) where in average a motion reduction of 36 % (4 mm) was found. The 10 patients included in the aforementioned study showed on average larger motion amplitudes than for the patients found in the current study. It has to be noted, however, that other than in Heerkens *et al.* (2017), where solely patients with PDAC were selected, our study was extended to include patients with cancer of the liver and gallbladder. The decision to include these patients was made to increase the initially very low rate of patients included in our study, but led to a heterogeneous patient cohort and the evaluation of pancreas motion for patients with a tumor-free pancreas. Furthermore, due to the limited space of the 60 cm wide MR bore, the treatment position with the arms positioned over the head could not be realized. This could have affected the absolute values of respiratory motion. It is not appearant from Heerkens *et al.* (2017) if patients were scanned with their arms above their heads or next to their body a statement about a potential difference cannot be made.

Several studies reported about pancreas tumor motion with on average significantly larger amplitudes of up to several centimeters (Bussels *et al.*, 2003; Minn *et al.*, 2009). Considering the seemingly constant 30 % – 50 % relative motion reduction achieved through the abdominal corset, patients with larger respiratory motion amplitudes would benefit more from its application. The 9 patients included in the current study included 4 patients where pancreas motion amplitudes were already noticeably small (<6 mm) during free breathing. For these patients the corset only reduced motion in average by merely ~ 1 mm. This shows that a decision strategy is mandatory to select patients for which the corset reduces motion significantly enough to cover the additional time and effort required for its manufacturing. This could potentially be performed by external respiration analysis, but would in an ideal case include a fast MRI scan to estimate the tumor motion characteristics. A fast single-slice 2D-cine MRI would suffice for this purpose but would on the other hand likely be challenging to implement due to the typically low availability of MRI scan time.

Our study also showed that although the corset only increased the patient chest diameter by ~ 1 cm, several patients could not be successfully scanned in the RT compatible MR setup using the coil holder for the MR surface coils, since this setup reduces the already

limited space in the 60 cm MRI bore. This emphasizes a drawback of MRI which is the generally limited space in the scanner's bore, excluding large or obese patients.

6.4 Future perspectives

Before a general recommendation for the clinical use of BioXmark® in PT of PDAC can be made, a systematic study on its visibility in X-ray imaging (including kV-CBCT) should be performed. As a first step, a phantom mimicking the X-ray attenuation properties of abdominal organs should be used to test the marker's visibility in different injection sites. As soon as the CE certificate for clinical use in abdominal tumor patients has been granted, an *in vivo* study should be conducted to validate if the marker's gelation behavior in *in vivo* pancreas leads to satisfactory visibility in X-ray and MR imaging.

A 4D-MRI motion phantom has been commissioned on the diagnostic 3.0 T MRI scanner and its target tracking accuracy has been assessed for selected motion depicting pulse sequences. This allows to perform QA of the scanner on a regular basis with a safe and reproducible positioning of the phantom and its actuator as well as an automatic evaluation of tracking accuracy. A QA protocol has, however, yet to be established including clinically motivated criteria for imaging accuracy and a typical time frame for re-evaluating image performance has to be set, based on the hardware dependent performance drifts. It is, however, strongly recommended to perform the described QA tests whenever new motion depicting sequences are used for clinical purposes. For QA on a potential future MR-Linac system, the tested motion phantom can be utilized as well, yet the fixation setup would not be necessary due to the lower static magnetic field. For the application on an MR-Linac the phantom would furthermore allow for the evaluation of tracking and gating accuracy and efficiency as well as dosimetric measurements of moving targets.

In cooperation with the ORD (Orthopädie- und Rehatechnik Dresden GmbH, Dresden, Germany) a concept of applying abdominal compression with a patient individualized MR guided PT compatible abdominal corset has been developed and confirmed to reduce respiratory induced motion. The established workflow allows for future manufacturing of the PT compatible abdominal corset. In order to estimate the clinical benefit, a dosimetric evaluation has to be performed where the possible reduction of dose to healthy tissue would be evaluated. Finally, the cost-effectiveness of the 3DPE corset should be assessed, where a

possible gain in quality adjusted life years is compared to its production costs. This however, would require a long-term study with more patients included for statistical significance.

Due to the high technical requirements for the manufacturing of the 3DPE corset, its clinical implementation is dependent on the cooperation with a orthopedic institute. Its transferability to other PT centers can therefore not be generalized. The investigated motion management techniques can also be translated to MR guided XT, for example for usage within an MR-Linac, but should be re-evaluated against other existing methods considering the complexity of the manufacturing of the presented corset. For XT the PU corset seems sufficient and requires less costs and temporal effort than the 3DPE corset.

7 Summary

Background

Patients with pancreatic cancer (PDAC) might benefit from proton therapy (PT) due to its potential to better spare healthy tissue from toxic dose than conventional MV X-ray therapy (XT). However, the poor soft-tissue contrast of X-ray based image guidance techniques and inter- and intrafraction organ motion increase the uncertainties during dose application. Hence, guidance by MR imaging might be a beneficial approach due to its high soft-tissue contrast and real-time imaging capability. In the transition from conventional X-ray guided XT to MR guided PT, methods for the management of inter- and intrafraction motion have to be re-evaluated, adapted or newly developed.

Hypotheses

For interfraction motion management it was hypothesized that the novel liquid fiducial marker BioXmark® is detectable on MRI when injected in pancreas tissue and reduces image degradation relative to commoonly used solid fiducial markers. For intrafraction motion mitigation it was hypothesized that a patient-specific MR compatible abdominal corset is feasible to be used in PT, reduces the respiratory induced pancreas motion and is well tolerated by patients with abdominal tumors. To assess the accuracy that the utilized clinical 3.0 T MRI scanner provides for the motion characterization study, first ground truth measurements had to be performed. Therefore, a 4D MR-Linac motion phantom was selected It was hypothesized that this phantom can be implemented at a diagnostic MRI scanner and used therein for QA of motion depicting pulse sequences.

Material and methods

The BioXmark® was quantitatively analyzed regarding its MR characteristics by relaxometry and compared to two solid fiducial markers in the framework of a gel phantom study. Furthermore, the MRI visibility of BioXmark® was tested for the first time in *ex vivo* tumorous pancreas tissue. An MR-Linac motion phantom was commissioned at a diagnostic 3.0 T MR scanner and a tool was developed for automatic assessment of the 3D geometrical fidelity and motion tracking accuracy of the used scanner. The material properties of three different corsets were tested regarding their applicability in PT. Furthermore, their effect on pancreas motion reduction was tested on a healthy volunteer by use of orthogonal 2D-cine and 4D-MRI on a 1.5 T MRI scanner. Subsequently, a clinical study was conducted, including 13 patients with abdominal cancer. Within the study, the effect on respiratory induced pancreas motion through the used 3DPE corset was analyzed by use of orthogonal 2D-cine and 4D-MRI on a 3.0 T MRI scanner. Furthermore, the patient's tolerance towards the corset was assessed.

Results

BioXmark® did not show a correlation between magnitude of visibility and artefact ($R_S = 0.0$) and only a weak correlation between size of visibility and artefact ($R_S = 0.4$). Contrary, for the solid markers a linear dependency between size of visibility and artefact was observed ($R_S = 0.99$) and a non-linear correlation between the magnitude of visibility and artefact ($R_S = 0.964$).

Injected in three *ex vivo* pancreas resection specimen, BioXmark® was detectable as hypointensity on both T_1-w and T_2-w MRI. Markers of all three size categories (20/25 µL, 50/60 µL, 100 µL), injected with three differently sized needles (18 G, 22 G, 25 G), could be detected with the clinically used sequences. However, a diffuse gelation or an injection too close to the surface hampered detectability, leading to 4 out of 17 markers being non-detectable on MRI.

The MR-Linac motion phantom was successfully commissioned on a diagnostic 3.0 T MRI scanner. A fixation and positioning aid was designed and constructed to allow a safe and reproducible positioning of the actuator and the phantom (< 0.4 mm). A tool for automatic distortion analysis was developed based on a reference CT scan. The analysis of a clinically used 3D GRE sequence revealed a maximum 3D distortion of 1.3 mm over an

elliptic cylindrical volume of $15 \times 23 \times 6\,\mathrm{cm}^3$. The reference CT scan also showed an intrinsic error of the target motion in AP/LR direction. High-contrast and geometrically reliable 2D-cine MR images of the phantom's moving target could be obtained. A tool for automatic target tracking was developed which revealed high accuracy of the motion depicting sequences ($< 0.2\,\mathrm{mm}$ in 2D-cine acquisitions, $< 0.3\,\mathrm{mm}$ in 4D-MRI).

A comparable reduction of respiratory induced pancreas motion of 46 % – 56 % (7.7 mm – 9.4 mm) was found for all three corsets. The material analysis, however, excluded the PU corset from use in PT due to its heterogeneities and showed that the 3DPE corset can be integrated in PT planning with the clinically used Hounsfield look-up table. The 3DPE corset was implemented into the PT workflow within a clinical study for 13 patients with abdominal cancer, where the corset was well tolerated. The MRI-based assessment of respiratory induced pancreas motion in 9 patients with and without the corset yielded a pancreas 3D motion reduction of in average 37 % ($\sim 3.3\,\mathrm{mm}$).

Conclusions

BioXmark® and the developed 3DPE corset have been considered suitable for use in MR guided PT. BioXmark® was visible as signal void in MRI independently of the used pulse sequence when exceeding the voxel size. BioXmark® , however, has to be investigated *in vivo* to confirm its MRI visibility in a realistic environment, which could potentially lead to a different gelation behavior affecting visibility. The developed corset reduced respiratory pancreas motion in patients with abdominal tumors and can be used in future for patients in MR guided PT. The study also revealed that a distinct amount of patients does not significantly benefit from a corset due to their already small ($< 6\,\mathrm{mm}$) pancreas motion in free breathing. Hence, a prior estimation of the patient's individual free breathing motion should be included before an abdominal corset is implemented in their PT workflow. The MR-Linac motion phantom showed a high accuracy in motion depiction and can be used in future for QA of the diagnostic MRI scanner for motion depicting sequences. This is strongly advised when new pulse sequences are implemented.

8 Zusammenfassung

Hintergrund

Patienten mit Bauchspeicheldrüsenkrebs könnten von der Protonentherapie (PT) profitieren, aufgrund ihres Potentials der Schonung von Risikoorganen. Jedoch führen die inter- und intrafraktionelle Beweglichkeit der Bauchspeicheldrüse zu hohen Unsicherheiten bei der Dosisapplikation und erfordern daher große Sicherheitssäume. Aufgrund des hohen Weichgewebskontrastes in der MRT und der Möglichkeit der Echtzeitbildgebung gewinnt die Unterstützung der Strahlentherapie durch die MRT stetig höheres Interesse. In der Translation von konventioneller Röntgen-geführter XT zur MR-geführten PT müssen Methoden zur Kontrolle der inter- und intrafraktionellen Organbeweglichkeit re-evaluiert, adaptiert oder neu entwickelt werden.

Fragestellung/Hypothese

Für die interfraktionelle Bewegungskontrolle wurde die Hypothese aufgestellt, dass der neu entwickelte Flüssigmarker BioXmark®, injiziert in Pankreasgewebe, sichtbar in der MR-Bildgebung ist und verglichen zu üblich verwendeten soliden Markern die Bildartefakte reduziert. Für die intrafraktionelle Bewegungskontrolle wurde erwartet, dass ein Patienten-individuelles MR-kompatibles Korsett die atmungs-induzierte Pankreasbeweglichkeit reduziert, von Patienten mit Tumoren im Oberbauch gut vertragen wird und in die PT implementiert werden kann. Ein 4D MR-Linac Bewegungsphantom wurde für die Evaluierung der Geometrietreue und der Genauigkeit der Bewegungswiedergabe des genutzten diagnostischen 3.0 T MR Scanners verwendet. Es wurde erwartet, dass dieses Phantom für die Verwendung am diagnostischen MR Scanner implementiert werden kann und für die Qualitätssicherung von bewegungscharakterisierenden MR Pulssequenzen genutzt werden kann.

Material und Methode

Die MR Eigenschaften von BioXmark® wurden in einer Phantomstudie durch MR Relaxometrie quantitativ analysiert und verglichen mit zwei Arten von soliden Marker. Des weiteren wurde die MR-Sichtbarkeit von BioXmark® das erste mal in *ex vivo* tumorösem Pankreasgewebe getestet für Markern dreier Größenkategorien (20/25 μL, 50/60 μL, 100 μL), injeziert mit jeweils drei verschiedenen Nadelgrößen (18 G, 22 G, 25 G). Ein 4D MR-Linac Bewegungsphantom wurde für den diagnostischen 3.0 T MR Scanner unserer Klinik kommissioniert und Programme für die automatische Evaluierung der 3D Geometrietreue und Genauigkeit der Bewegungscharakterisierung entwickelt. Drei Korsetts aus verschiedenen Materialien (PU, PE, 3DPE) wurden in Bezug auf die Verwendbarkeit in der PT untersucht. Des weiteren wurde der Effekt der Korsetts auf die Reduzierung der Pankreasbeweglichkeit bei einem gesunden Freiwilligen analysiert, mittels zeitaufgelöster 2D-cine MRT und respirationskorrelierter 4D-MRT in einem 1.5 T MR Scanner. Daraufhin wurde eine klinische Studie durchgeführt, die 13 Patienten mit Tumor im Oberbauch einschloss. Im Rahmen der Studie wurde der Effekt des verwendeten 3DPE Korsetts auf die Reduktion der Pankreasbeweglichkeit analysiert, mittels 2D-cine MRT und 4D-MRT in einem 3.0 T MR Scanner. Abschließend wurde die Patienten-Verträglichkeit bei Anwendung des Korsetts analysiert.

Ergebnisse

Für BioXmark® wurde keine Korrelation zwischen der Intensität der Sichtbarkeit und Artefakte gefunden ($R_S = 0.0$) und nur eine schwache Korrelation zwischen der Größe der Sichtbarkeit und Artefakte ($R_S = 0.4$). Im Gegensatz dazu wurde für die soliden Marker eine lineare Abhängigkeit der Größe der Sichtbarkeit und Artefakte ($R_S = 0.99$) und eine nicht-lineare Abhängigkeit zwischen der Intensität der Sichtbarkeit und Artefakte gefunden ($R_S = 0.964$). Nach Injektion in drei *ex vivo* Pankreas-Resektionspräparate war BioXmark® als Hypointensität in sowohl T_1- als auch T_2- gewichteten MR Bildgebung sichtbar. Marker aller drei getesteten Größenkategorien waren in klinisch verwendeten MR Sequenzen detektierbar. Jedoch führte eine diffuse Gelierung oder Injektion zu nah am Geweberand zur Minderung der Detektierbarkeit. Dies hatte zur Folge hatte, dass 4 von in Summe 17 Markern in der MR-Bildgebung nicht erkennbar waren.

Das MR-Linac Bewegungsphantom wurde erfolgreich am diagnostischen 3.0 T MR Scanner kommissioniert. Eine Fixierungs- und Positionierungshilfe wurde entwickelt und kon-

struiert, die eine sichere und reproduzierbare Positionierung des Aktuators und des Phantoms (< 0.4 mm) ermöglichte. Ein Programm zur automatischen Verzerrungsanalyse wurde entwickelt, basierend auf einer Referenz-CT Aufnahme. Die Auswertung einer klinisch verwendeten 3D GRE Sequenz offenbarte eine maximale Verzerrung von 1.3 mm in einem elliptischen Zylindervolumen von $15 \times 23 \times 6\,\text{cm}^3$. Das Referenz-CT offenbarte zusätzlich einen Abweichung der eingestellten Targetbeweglichkeit in AP/LR Richtung. Kontrastreiche und geometrisch korrekte 2D-cine MR Bilder des sich bewegenden Phantom-Targets konnten aufgenommen werden. Ein Programm für ein automatisiertes Target-Tracking wurde entwickelt, welches eine hohe Genauigkeit der bewegungscharakterisierenden Sequenzen bestätigte (< 0.2 mm in 2D-cine MRT, < 0.3 mm in 4D-MRT).

Eine vergleichbare Reduzierung der respirationsbedingten Pankreas-Bewegung von 46 % – 56 % (7.7 mm – 9.4 mm) wurde für die drei getesteten Korsetts gefunden. Die Materialanalyse führte jedoch zum Ausschluss des PU Korsetts für die Verwendung in der PT, aufgrund der gravierenden Heterogenität des Korsettmaterials. Das 3DPE Korsett wurde als für die PT implementierbar bewertet, wobei eine direkte Integration in der PT Planung mit der klinisch verwendeten Hounsfield-SPR Übersetzungstabelle möglich war. Das 3DPE Korsett wurde für 13 Patienten mit Tumor im Oberbauch in den PT Arbeitsablauf integriert, in welchem das Korsett von den Patienten gut toleriert wurde. Die MR-basierte Analyse der respirationsbedingten Pankreasbewegung in 9 Patienten mit und ohne Korsett ergab eine Reduzierung der Beweglichkeit um 37 % ($\sim$ 3.3 mm).

Schlussfolgerungen

BioXmark® und das entwickelte 3DPE Korsett wurden als verwendbar für die MR geführte PT bewertet. BioXmark® war in der MR-Bildgebung als Hypointensität sichtbar, unabhängig von der verwendeten MR Pulssequenz, solange die Markergröße die Voxelauflösung überschritt. Die MR-Sichtbarkeit von BioXmark® sollte jedoch *in vivo* getestet werden, da sich dort die Gelierung unterscheiden könnte und dementsprechend die Sichtbarkeit beeinflussen könnte.

Das MR-Linac Bewegungsphantom kann in Zukunft für QA von bewegungscharakterisierenden Pulssequenzen des diagnostischen MR Scanners verwendet werden. Dies ist empfohlen, wann immer neue Pulssequenzen implementiert werden.

Das entwickelte Korsett reduziert die respirationsbedingte Pankreas-Beweglichkeit in Pa-

tienten mit Tumor im Oberbauch um $\sim$37 % und kann in Zukunft für die MR geführte PT verwendet werden. Die Studie offenbarte jedoch auch, dass eine erhebliche Anzahl an Patienten nicht von der Verwendung eines Korsetts profitiert, aufgrund ihrer initial geringen Beweglichkeit bei freier Atmung ($<$ 6 mm). Schlussfolgernd ist eine vorherige Einschätzung der Beweglichkeit jedes individuellen Patienten bei freier Atmung zu empfehlen, bevor eine Entscheidung über die Implementierung des Korsetts in der PT getroffen wird.

Bibliography

Akbari M, Yousefnia H, and Mirrezaei E. 2014. Calculation of water equivalent ratio of several dosimetric materials in proton therapy using FLUKA code and SRIM program. Appl Radiat Isot 90:89–93. DOI: 10.1016/j.apradiso.2014.03.012.

Albertini F, Hug E, and Lomax A. 2010. The influence of the optimization starting conditions on the robustness of intensity-modulated proton therapy plans. Phys Med Biol 55:2863–78. DOI: 10.1088/0031-9155/55/10/005.

Arruebo M, Vilaboa N, Sáez-Gutierrez B, Lambea J, Tres A, Valladares M, and González-Fernández A. 2011. Assessment of the evolution of cancer treatment therapies. Cancers 3:3279–3330. DOI: 10.3390/cancers3033279.

Avants B, Epstein C, Grossman M, and Gee J. 2008. Symmetric diffeomorphic image registration with cross-correlation: evaluating automated labeling of elderly and neurodegenerative brain. Med Image Anal 12:26–41. DOI: 10.1016/j.media.2007.06.004.

Avants BB, Tustison N, Stauffer M, Song G, Wu B, and Gee J. 2014. The Insight ToolKit image registration framework. Front Neuroinform 8:44. DOI: 10.3389/fninf.2014.00044.

Bair R, Bair E, and Viswanathan A. 2015. A radiopaque polymer hydrogel used as a fiducial marker in gynecologic-cancer patients receiving brachytherapy. Brachytherapy 14. DOI: 10.1016/j.brachy.2015.08.008.

Baldwin L, Wachowicz K, Thomas S, Rivest R, and BG F. 2007. Characterization, prediction, and correction of geometric distortion in 3 T MR images. Med Phys 34:388–99. DOI: 10.1118/1.2402331.

Barral J, Gudmundson E, Stikov N, Etezadi-Amoli M, Stoica P, and G Nishimura D. 2010. A robust methodology for in vivo T-1 mapping. Magn Reson Med 64:1057–67. DOI: 10.1002/mrm.22497.

Baskar R, Lee KA, Yeo R, and Yeoh KW. 2012. Cancer and radiation therapy: current advances and future directions. Int J Med Sci 9:193–9. DOI: 10.7150/ijms.3635.

Batista V, Richter D, Combs S, and Jäkel O. 2017. Planning strategies for inter-fractional robustness in pancreatic patients treated with scanned carbon therapy. Radiat Oncol 12. DOI: 10.1186/s13014-017-0832-x.

Bernatowicz K, Peroni M, Perrin R, Weber D, and Lomax AJ. Feb. 2016. 4D dose reconstruction for scanned proton therapy using liver 4DCT-MRI. Int J Radiat Oncol Biol Phys 95:216–223. DOI: 10.1016/j.ijrobp.2016.02.050.

Bert C and Durante M. 2011. Motion in radiotherapy: Particle therapy. Phys Med Biol 56:R113–44. DOI: 10.1088/0031-9155/56/16/R01.

Bert C, Grözinger S, and Rietzel E. 2008a. Quantification of interplay effects of scanned particle beams and moving targets. Phys Med Biol 53:2253–65. DOI: 10.1088/0031-9155/53/9/003.

Bert C, Saito N, Schmidt A, Chaudhri N, Schardt D, and Rietzel E. 2008b. Target motion tracking with a scanned particle beam. Med Phys 34:4768–71. DOI: 10.1118/1.2815934.

Bethe H. 1930. Zur Theorie des Durchgangs schneller Korpuskularstrahlen durch Materie. Ann Phys 397:325–400. DOI: 10.1002/andp.19303970303.

Bissonnette JP, Franks K, G Purdie T, J Moseley D, Sonke JJ, A Jaffray D, Dawson L, and Bezjak A. 2009. Quantifying interfraction and intrafraction iumor motion in lung stereotactic body radiotherapy using respiration-correlated cone beam computed tomography. Int J Radiat Oncol Biol Phys 75:688–95. DOI: 10.1016/j.ijrobp.2008.11.066.

Bloch F. 1933. Zur Bremsung rasch bewegter Teilchen beim Durchgang durch Materie. Ann Phy 408:285–320. DOI: 10.1002/andp.19334080303.

Bloch F. 1946. Nuclear induction. Phys Rev 70:460–474. DOI: 10.1103/PhysRev.70.460.

Bolsi A, Peroni M, Amelio D, Dasu A, Stock M, Toma-Dasu I, Witt Nyström P, and Hoffmann A. 2018. Practice patterns of image guided particle therapy in Europe: A 2016 survey of

the European Particle Therapy Network (EPTN). Radiother Oncol 128. DOI: 10.1016/j.radonc.2018.03.017.

Bortfeld T and Schlegel W. 1996. An analytical approximation of depth-dose distributions for therapeutic proton beams. Phys Med Biol 41:1331–9. DOI: 10.1088/0031-9155/41/8/006.

Bostel T, Paffenberger A, Delorme S, Dreher C, Echner G, Haering P, Lang C, Splinter M, Laun F, Müller M, Jökel O, Debus J, Huber P, Sterzing F, and Nicolay N. 2018. Prospective feasibility analysis of a novel off-line approach for MR-guided radiotherapy. Strahlenther Onkol 194:425–434. DOI: 10.1007/s00066-017-1258-y.

Bragg M and Kleeman R. 1904. On the ionization curves of radium. Philos Mag 8:726–738. DOI: 10.1080/14786440409463246.

Bray F, Ferlay J, Soerjomataram I, Siegel RL, Torre LA, and Jemal A. 2018. Global cancer statistics 2018: GLOBOCAN estimates of incidence and mortality worldwide for 36 cancers in 185 countries. CA Cancer J Clin 68:394–424. DOI: 10.3322/caac.21492. eprint: https://onlinelibrary.wiley.com/doi/pdf/10.3322/caac.21492.

Brix L, Ringgaard S, Sørensen TS, and Poulsen PR. 2014. Three-dimensional liver motion tracking using real-time two-dimensional MRI. Med Phys 41:042302. DOI: 10.1118/1.4867859.

Brown M and Semelka R. 2003. MRI basic principles and applications - Third edition. Wiley-Liss.

Bujold A, Craig T, Jaffray D, and Dawson L. 2012. Image-guided radiotherapy: Has it influenced patient outcomes? Semin Radiat Oncol 22:50–61. DOI: 10.1016/j.semradonc.2011.09.001.

Bussels B, Goethals L, Feron M, Bielen D, Dymarkowski S, Suetens P, and Haustermans K. 2003. Respiration-induced movement of the upper abdominal organs: A pitfall for the three-dimensional conformal radiation treatment of pancreatic cancer. Radiother Oncol 68:69–74. DOI: 10.1016/S0167-8140(03)00133-6.

Chamie K, Pantuck A, Bass J, James H, Mouraviev V, Gusso T, Grubb R, and Bohnert W. 2014. MP61-17 Initial multicenter experience utilizing an absorbable radiopaque hydrogel for patients with invasive bladder tumors. J Urol 191:689–690.

Chandarana H, Wang H, Tijssen R, and Das I. 2018. Emerging role of MRI in radiation therapy. J Magn Reson Imaging 48. DOI: 10.1002/jmri.26271.

Chen CC, Wan YL, Wai YY, and Liu HL. 2005. Quality assurance of clinical MRI Scanners using ACR MRI phantom: preliminary results. J Digit Imaging 17:279–84. DOI: 10.1007/s10278-004-1023-5.

Cheng HLM and Wright GA. 2006. Rapid high-resolution T1 mapping by variable flip angles: Accurate and precise measurements in the presence of radiofrequency field inhomogeneity. Magn Reson Med 55:566–74. DOI: 10.1002/mrm.20791.

Chicoine M, Lim CCH, Evans JA, Singla A, Zipfel GJ, Rich KM, Dowling J, Leonard JR, Smyth MD, Santiago P, Leuthardt E, Limbrick DD, and Dacey RG. 2011. Implementation and preliminary clinical experience with the use of ceiling mounted mobile high field intraoperative magnetic resonance imaging between two operating rooms. Acta Neurochir Suppl 109:97–102. DOI: 10.1007/978-3-211-99651-5_15.

CIRS CIRS. 2014. User Manual - MRI-LINAC dynamic phantom model 008M.

Coletta F. 2001. A study of water T-1 and T-2 NMR relaxation times in healthy and cancer affected human blood plasma doped with hematoporphyrin IX dye. Spectrosc Lett 34(5):579–589. DOI: 10.1081/SL-100106872.

Combs S, Habermehl D, Kessel K, Bergmann F, Werner J, Brecht I, Schirmacher P, Jäger D, Büchler M, and J D. 2013. Intensity modulated radiotherapy as neoadjuvant chemoradiation for the treatment of patients with locally advanced pancreatic cancer. Strahlenther Onkol 189:738–744.

Czervionke L, Daniels D, Wehrli F, Mark L, Hendrix L, Strandt J, Williams A, and Haughton V. 1988. Magnetic susceptibility artifacts in gradient-recalled echo MR imaging. AJNR Am J Neuroradiol 9:1149–55.

De Bazelaire CMJ, Duhamel GD, Rofsky NM, and Alsop DC. 2004. MR imaging relaxation times of abdominal and pelvic tissues measured in vivo at 3.0 T: Preliminary results. Radiology 230:652–659. DOI: 10.1148/radiol.2303021331.

De Blanck SR, Rydhög J, Larsen KR, Clementsen PF, Josipović M, Aznar M, Af Rosenschold PM, Jølck R, Specht L, Andresen TL, and Persson G. 2018. Safety and long-term visibility of a novel liquid fiducial marker for use in image guided radiotherapy of non-small cell lung cancer. Clin Transl Radiat Oncol 13. DOI: 10.1016/j.ctro.2018.07.004.

De Roover R, Crijns W, Poels K, Peeters R, Draulans C, Haustermans K, and Depuydt T. 2018. Characterization of a novel liquid fiducial marker for multi-modal image guidance in stereotactic body radiotherapy of prostate cancer. Med Phys 45. DOI: 10.1002/mp.12860.

De Ruysscher D, Sterpin E, Haustermans K, and Depuydt T. 2015. Tumour movement in proton therapy: solutions and remaining questions: a review. Cancers 7:1143–53. DOI: 10.3390/cancers7030829.

De Vera P, Abril I, and Garcia-Molina R. 2013. Water equivalent properties of materials commonly used in proton dosimetry. Appl Radiat Isot 83:122–127. DOI: 10.1016/j.apradiso.2013.01.023.

Demol B, Boydev C, Korhonen J, and Reynaert N. 2016. Dosimetric characterization of MRI-only treatment planning for brain tumors in atlas-based pseudo-CT images generated from standard T1-weighted MR images. Med Phys 43:6557–6568. DOI: 10.1118/1.4967480.

Devic S. 2012. MRI simulation for radiotherapy treatment planning. Med Phys 39:6701–11. DOI: 10.1118/1.4758068.

Didolkar M, Coleman C, Brenner MJ, Chu KU, Olexa N, Stanwyck E, Yu A, Neerchal N, and Rabinowitz S. 2010. Image-guided stereotactic radiosurgery for locally advanced pancreatic adenocarcinoma results of first 85 patients. J Gastrointest Surg 14:1547–59. DOI: 10.1007/s11605-010-1323-7.

Doi R, Imamura M, Hosotani R, Imaizumi T, Hatori T, Takasaki K, Funakoshi A, Wakasugi H, Asano T, Hishinuma S, Ogata Y, Sunamura M, Yamaguchi K, Tanaka M, Takao

S, Aikou T, Hirata K, Maguchi H, Aiura K, and Yoshida S. 2008. Surgery versus radiochemotherapy for resectable locally invasive pancreatic cancer: final results of a randomized multi-institutional trial. Surg Today 38:1021–8. DOI: 10.1007/s00595-007-3745-8.

Dolde K, Dávid C, Echner G, Floca R, Hentschke C, Maier F, Niebuhr N, Ohmstedt K, Saito N, Alimusaj M, Fluegel B, Naumann P, Dreher C, Freitag M, and Pfaffenberger A. 2018a. 4DMRI-based analysis of inter - And intrafractional pancreas motion and deformation with different immobilization devices. Biomed Phys Eng Express 5. DOI: 10.1088/2057-1976/aaf9ae.

Dolde K, Naumann P, Dávid C, Gnirs R, Kachelrieß M, John Lomax A, Saito N, Weber D, Pfaffenberger A, and Zhang Y. 2018b. 4D dose calculation for PBS proton therapy of pancreatic cancer using repeated 4DMRI dataset. Phys Med Biol 63. DOI: 10.1088/1361-6560/aad43f.

Dolde K, Schneider S, Stefanowicz S, Alimusaj M, Flügel B, Saito N, Troost EGC, Pfaffenberger A, and Hoffmann AL. 2019a. Comparison of pancreatic respiratory motion management with three abdominal corsets for particle radiation therapy: Case study. J Appl Clin Med Phys 20:111–119. DOI: 10.1002/acm2.12613.

Dolde K, Zhang Y, Chaudhri N, Dávid C, Kachelrieß M, John Lomax A, Naumann P, Saito N, Charles Weber D, and Pfaffenberger A. 2019b. 4DMRI-based investigation on the interplay effect for pencil beam scanning proton therapy of pancreatic cancer patients. Radiat Oncol 14. DOI: 10.1186/s13014-019-1231-2.

Dosanjh M and Bernier J. 2018. Advances in particle therapy: a multidisciplinary approach. CRC Press.

Dou T, Thomas D, O'Connell D, Bradley J, Lamb J, and A. Low D. 2015. Technical note: simulation of 4DCT tumor motion measurement errors. Med Phys 42:6084–6089. DOI: 10.1118/1.4931416.

Durante M and Loeffler JS. 2009. Charged particles in radiation oncology. Nat Rev Clin Oncol 7:37–43. DOI: 10.1038/nrclinonc.2009.183.

Edmund JM and Nyholm T. 2017. A review of substitute CT generation for MRI-only radiation therapy. Radiat Oncol 12. DOI: 10.1186/s13014-016-0747-y.

Ehrbar S, Perrin R, Peroni M, Bernatowicz K, Parkel T, Pytko I, Klöck S, Guckenberger M, Tanadini-Lang S, Weber DC, and Lomax A. 2016. Respiratory motion-management in stereotactic body radiation therapy for lung cancer – A dosimetric comparison in an anthropomorphic lung phantom (LuCa). Radiother Oncol 121:328–334. DOI: https://doi.org/10.1016/j.radonc.2016.10.011.

Engler J. 2017. Report - Entwicklung einer Sicherheits- und Hilfskonstruktion für ein 4D-dynamic Phantom am MRT. Fakultät für Maschinenbau, Institut für Strukturleichtbau, Chemnitz.

Engler J. 2018. Bachelor thesis - Automatisierte Qualitätssicherung zeitaufgelöster MRT-Bildaufnahmen für die Bewegungscharakterisierung von Tumoren für die bildgestützte Strahlentherapie-Planung. Fakultät für Maschinenbau, Institut für Strukturleichtbau, Chemnitz.

Fatemi-Ardekani A, Wronski M, Kim A, Stanisz G, Sarfehnia A, and Keller B. 2015. SU-E-J-209: Geometric distortion at 3T in a commercial 4D MRI-compatible phantom. Med Phys 42:3313–3313. DOI: 10.1118/1.4924295.

Fernandes CD, Dinh CV, Steggerda M, ter Beek L, Smolic M, D. van Buuren L, Pos FJ, and van der Heide UA. 2017. Prostate fiducial marker detection with the use of multi-parametric magnetic resonance imaging. Phys Imaging Radiat Oncol 1:14–20. DOI: 10.1016/j.phro.2017.02.001.

Fernández-Jiménez R, Sánchez-González J, Aguero J, del Trigo M, Galán-Arriola C, Fuster V, and Ibáñez B. 2015. Fast T2 gradient-spin-echo (T2-GraSE) mapping for myocardial edema quantification: First in vivo validation in a porcine model of ischemia/reperfusion. J Cardiovasc Magn Reson 17. DOI: 10.1186/s12968-015-0199-9.

Fokas E, Clifford C, Spezi E, Joseph G, Branagan J, Hurt C, Nixon L, Abrams R, Staffurth J, and Mukherjee S. 2015. Comparison of investigator-delineated gross tumor volumes

and quality assurance in pancreatic cancer: Analysis of the pretrial benchmark case for the SCALOP trial. Radiother Oncol. DOI: 10.1016/j.radonc.2015.08.026.

Fontana G, Riboldi M, Gianoli C, Chirvase C, Villa G, Paganelli C, Summers P, Tagaste B, Pella A, Fossati P, Ciocca M, Baroni G, Valvo F, and Orecchia R. 2016. MRI quantification of pancreas motion as a function of patient setup for particle therapy -A preliminary study. J Appl Clin Med Phys 17:6236. DOI: 10.1120/jacmp.v17i5.6236.

Fraass B, Mcshan D, F Diaz R, Ten Haken R, Aisen A, Gebarski S, Glazer G, and S Lichter A. 1987. Integration of magnetic resonance imaging into radiation therapy treatment planning: I. Technical considerations. Int J Radiat Oncol Biol Phys 13:1897–908. DOI: 10.1016/0360-3016(87)90358-0.

Fuji H, Schneider U, Ishida Y, Konno M, Yamashita H, Kase Y, Murayama S, Onoe T, Ogawa H, Harada H, Asakura H, and Nishimura T. 2013. Assessment of the organ-dose reduction and secondary cancer risk associated with the use of proton beam therapy and intensity modulated radiation therapy in treatment of neuroblastoma. Radiat Oncol 8:255. DOI: 10.1186/1748-717X-8-255.

Ge J, Santanam L, Noel C, and Parikh P. 2013. Planning 4-dimensional computed tomography (4DCT) cannot adequately represent daily intrafractional motion of abdominal tumors. Int J Radiat Oncol Biol Phys 85:999–1005.

Ghiglia D and Pritt M. 1989. Two-dimensional phase unwrapping: theory, algorithms and software. Wiley-Interscience.

Giebeler A, Fontenot J, Baiter P, Ciangaru G, Zhu R, and Newhauser W. 2008. Assessment of implanted helical gold markers for patients receiving proton radiotherapy for prostate cancer. Trans Am Nucl Soc 99:578–579.

Giebeler A, Fontenot J, Balter P, Ciangaru G, Zhu X, and Newhauser W. 2009. Dose perturbations from implanted helical gold markers in proton therapy of prostate cancer. J Appl Clin Med Phys 10:2875. DOI: 10.1120/jacmp.v10i1.2875.

Gillen S, Schuster T, Mayer zum Büschenfelde C, Friess H, and Kleeff J. 2010. Preoperative/neoadjuvant therapy in pancreatic cancer: a systematic review and meta-analysis

of response and resection percentages. PLoS Med 10. DOI: 10.1371/journal.pmed.1000267.

Goto Y, Nakamura A, Ashida R, Sakanaka K, Itasaka S, Shibuya K, Matsumoto S, Kanai M, Isoda H, Masui T, Kodama Y, Takaori K, Hiraoka M, and Mizowaki T. 2018. Clinical evaluation of intensity-modulated radiotherapy for locally advanced pancreatic cancer. Radiat Oncol 13:118. DOI: 10.1186/s13014-018-1063-5.

Graeff C. 2014. Motion mitigation in scanned ion beam therapy through 4D-optimization. Phys Med 30. Particle Radiosurgery Conference:570–577. DOI: https://doi.org/10.1016/j.ejmp.2014.03.011.

Graf H, Steidle G, Martirosian P, A Lauer U, and Schick F. 2006. Effects on MRI due to altered RF polarization near conductive implants or instruments. Med Phys 33:124–7. DOI: 10.1118/1.2132571.

Gurney-Champion O, Bruins Slot T, Lens E, Horst A, Klaassen R, Laarhoven H, van Tienhoven G, E. van Hooft J, J. Nederveen A, and Bel A. 2016. Quantitative assessment of biliary stent artifacts on MR images: Potential implications for target delineation in radiotherapy. Med Phys 43:5603–5615. DOI: 10.1118/1.4962476.

Gurney-Champion O, Lens E, Horst A, Houweling A, Klaassen R, E van Hooft J, Stoker J, van Tienhoven G, J Nederveen A, and Bel A. 2015. Visibility and artifacts of gold fiducial markers used for image guided radiation therapy of pancreatic cancer on MRI. Med Phys 42:2638. DOI: 10.1118/1.4918753.

Gurney-Champion O, Versteijne E, Horst A, Lens E, Rütten H, Heerkens H, M. R. M. Paardekooper G, Berbee M, Rasch C, Stoker J, R. W. Engelbrecht M, van Herk M, J. Nederveen A, Klaassen R, Laarhoven H, van Tienhoven G, and Bel A. 2017. Addition of MRI for CT-based pancreatic tumor delineation: a feasibility study. Acta Oncol 4:923–930. DOI: 10.1080/0284186X.2017.1304654.

Haase A, Frahm J, Matthaei D, Hänicke W, and Merboldt KD. 1986. FLASH imaging: Rapid NMR imaging using low flip-angle pulses. J Magn Reson 67:258–266. DOI: 10.1016/0022-2364(86)90433-6.

Habermehl D, Henkner K, Ecker S, Jäkel O, Debus J, and Combs UPDS. 2013. Evaluation of different fiducial markers for image-guided radiotherapy and particle therapy. J Radiat Res 54. DOI: 10.1093/jrr/rrt071.

Hajatdoost L, Sedeghat K, Walker E, Thomas J, and Kosari S. 2018. Chemotherapy in pancreatic cancer: a systematic review. Medicina (Kaunas) 54:48. DOI: 10.3390/medicina54030048.

Hartwig W, Hackert T, Hinz U, Gluth A, Bergmann F, Strobel O, W Büchler M, and Werner J. 2011. Pancreatic cancer surgery in the new millennium. Ann Surg 254:311–9. DOI: 10.1097/SLA.0b013e31821fd334.

Hattori K, Ikemoto Y, Takao W, Ohno S, Harimoto T, Kanazawa S, Oita M, Shibuya K, Kuroda M, and Kato H. 2013. Development of MRI phantom equivalent to human tissues for 3.0-T MRI. Med Phys 40:032303. DOI: 10.1118/1.4790023.

Heerkens H, Reerink O, Intven M, R. Hiensch R, Berg C, Crijns S, van Vulpen M, and Meijer G. 2017. Pancreatic tumor motion reduction by use of a custom abdominal corset. Phys Imaging Radiat Oncol 2:7–10. DOI: 10.1016/j.phro.2017.02.003.

Van Herk M. 2004. Error and margins in radiotherapy. Semin Radiat Oncol 14:52–64. DOI: 10.1053/j.semradonc.2003.10.003.

Hoult DI. 2000. The principle of reciprocity in signal strength calculations—A mathematical guide. Concepts Magn Reson 12:173–187. DOI: 10.1002/1099-0534(2000)12:4<173::AID-CMR1>3.0.CO;2-Q.

Hsu SH, Peng Q, and A Tomé W. 2019. On the generation of synthetic CT for a MRI-only radiation therapy workflow for the abdomen. J Phys Conf Ser 1154:012011. DOI: 10.1088/1742-6596/1154/1/012011.

IARC. 2018. International Agency for Research on Cancer, GLOBOCAN 2018. URL: http://gco.iarc.fr/today/home.

Jackson EF, Bronskill MJ, Drost DJ, Och J, Pooley RA, Sobol WT, and Clarke GD. 2010. Acceptance testing and quality assurance procedures for magnetic resonance imaging facilities, report 100 of the AAPM task group 1. AAPM Rep.

Jaffray DA, Carlone MC, Milosevic MF, Breen SL, Stanescu T, Rink A, Alasti H, Simeonov A, Sweitzer MC, and Winter J. 2014. A facility for magnetic resonance-guided radiation therapy. Semin Radiat Oncol 24:193–195. DOI: 10.1016/j.semradonc.2014.02.012.

Jølck R, Binderup T, Hansen A, Scherman JB, Munck af Rosenschold P, Kjaer A, and Andresen T. 2014. Injectable colloidal gold in a sucrose acetate isobutyrate gelating matrix with potential use in radiation therapy. Adv Healthc Mater. DOI: 10.1002/adhm.201300668.

Jonsson J, Garpebring A, Karlsson M, and Nyholm T. 2011. Internal fiducial markers and susceptibility effects in MRI-simulation and measurement of spatial accuracy. Int J Radiat Oncol Biol Phys 82:1612–1618. DOI: doi:10.1016/j.ijrobp.2011.01.046.

Jouglar E, Wagner A, Delpon G, Campion L, Meingan P, Bernier V, Demoor-Goldschmidt C, Mahé MA, Lacornerie T, and Supiot S. 2016. Can we spare the pancreas and other abdominal organs at risk? A comparison of conformal radiotherapy, helical tomotherapy and proton beam therapy in pediatric irradiation. PLoS One 11:e0164643. DOI: 10.1371/journal.pone.0164643.

Karava K, Ehrbar S, Riesterer O, Roesch J, Glatz S, Klöck S, Guckenberger M, and Tanadini-Lang S. 2017. Potential dosimetric benefits of adaptive tumor tracking over the internal target volume concept for stereotactic body radiation therapy of pancreatic cancer. Radiat Oncol 12:175. DOI: 10.1186/s13014-017-0906-9.

Kartalis N, Pozzi Mucelli R, and Sundin A. 2015. Recent developments in imaging of pancreatic neuroendocrine tumors. Ann Gastroenterol 28:193–202.

Keall P, Mageras G, Balter J, S Emery R, Forster K, Jiang S, Kapatoes J, Low D, Murphy M, R Murray B, R Ramsey C, B Van Herk M, Sastry Vedam S, Wong JW, and Yorke E. 2006. The management of respiratory motion in radiation oncology, report of AAPM Task Group 76. Med Phys. Med Phys 33:3874–900. DOI: 10.1118/1.2349696.

Kelsen D. 1994. The use of chemotherapy in the treatment of advanced gastric and pancreas cancer. Semin Oncol:58–56.

Kingsley P, Ogg R, Reddick W, and RG S. 1998. Correction of errors caused by imperfect inversion pulses in MR imaging measurement of T1 relaxation times. Magn Reson Imaging 16:1049–1055.

Klein S, Staring M, Murphy K, Viergever MA, and Pluim JPW. 2009. Elastix: A Toolbox for intensity-based medical image registration. IEEE Trans Med Imaging 29:196–205. DOI: 10.1109/TMI.2009.2035616.

Knopf AC, Hong T, and Lomax A. 2011. Scanned proton radiotherapy for mobile targets - The effectiveness of re-scanning in the context of different treatment planning approaches and for different motion characteristics. Phys Med Biol 56:7257–71. DOI: 10.1088/0031-9155/56/22/016.

Koivula L, Wee L, and Korhonen J. 2016. Feasibility of MRI-only treatment planning for proton therapy in brain and prostate cancers: Dose calculation accuracy in substitute CT images. Med Phys 43:4634–4642. DOI: 10.1118/1.4958677.

Kraus KM, Heath E, and Oelfke U. 2011. Dosimetric consequences of tumour motion due to respiration for a scanned proton beam. Phys Med Biol 56:6563–81. DOI: 10.1088/0031-9155/56/20/003.

Lagarias J, Reeds JA, Wright MH, and Wright P. 1998. Convergence properties of the Nelder–Mead simplex method in low dimensions. SIAM J Optim 9:112–147. DOI: 10.1137/S1052623496303470.

Lagendijk J, Raaymakers B, Raaymakers A, Overweg J, Brown K, Kerkhof E, van der Put R, Hårdemark B, van Vulpen M, and van der Heide U. 2008. MRI/linac integration. Radiother Oncol 86:25–29. DOI: 10.1016/j.radonc.2007.10.034.

Lebel M and Wilman AH. 2010. Transverse Relaxometry with Stimulated Echo Compensation. Magn Reson Med 64:1005–14. DOI: 10.1002/mrm.22487.

Lin L, Souris K, Kang M, Glick A, Lin H, Huang S, Stützer K, Janssens G, Sterpin E, Lee J, D. Solberg T, E. McDonough J, B. Simone C, and Ben-Josef E. 2017. Evaluation of motion mitigation using abdominal compression in the clinical implementation of pencil beam scanning proton therapy of liver tumors. Med Phys 44:703–712. DOI: 10.1002/mp.12040.

Liney G and van der Heide U. 2019. MRI for radiotherapy: planning, delivery, and response assessment. DOI: 10.1007/978-3-030-14442-5.

Lühr A, von Neubeck C, Krause M, and Troost EG. 2018. Relative biological effectiveness in proton beam therapy – Current knowledge and future challenges. Clin Transl Radiat Oncol 9:35–41. DOI: https://doi.org/10.1016/j.ctro.2018.01.006.

Lundman J, Bylund M, Garpebring A, Thellenberg-Karlsson C, and Nyholm T. Mar. 2017. Patient-induced susceptibility effects simulation in magnetic resonance imaging. Phys Imaging Radiat Oncol 1:41–45. DOI: 10.1016/j.phro.2017.02.004.

Lutz ST, Jones J, and Chow E. 2014. Role of radiation therapy in palliative care of the patient with cancer. J Clin Oncol 32. DOI: 10.1200/JCO.2014.55.1143.

Machiels M, van Hooft J, Jin P, van Berge Henegouwen M, van Laarhoven H, Alderlisten T, and Hulshof M. 2015. Endoscopy/EUS-guided fiducial marker placement in patients with esophageal cancer: a comparative analysis of 3 types of markers. Gastrointest Endosc 82:641–649. DOI: 10.1016/j.gie.2015.03.1972.

Mampuya A, Matsuo Y, Ueki N, Nakamura M, Mukumoto N, Nakamura A, Iizuka Y, Kishi T, Mizowaki T, and Hiraoka M. 2014. The impact of abdominal compression on outcome in patients treated with stereotactic body radiotherapy for primary lung cancer. J Radiat Res 55. DOI: 10.1093/jrr/rru028.

Mann P, Witte M, Moser T, Lang C, Runz A, Johnen W, Berger M, Biederer J, and P Karger C. 2017. 3D dosimetric validation of motion compensation concepts in radiotherapy using an anthropomorphic dynamic lung phantom. Phys Med Biol 62:573–595. DOI: 10.1088/1361-6560/aa51b1.

Maspero M, Savenije MHF, Dinkla A, Seevinck P, Intven M, Jürgenliemk-Schulz I, Kerkmeijer LGW, and Berg C. 2018. Dose evaluation of fast synthetic-CT generation using a generative adversarial network for general pelvis MR-only radiotherapy. Phys Med Biol. DOI: 10.1088/1361-6560/aada6d.

Meyers S, Kolind S, Laule C, and Mackay A. 2015. Measuring water content using T2 relaxation at 3T: phantom validations and simulations. Magn Reson Imaging 34. DOI: 10.1016/j.mri.2015.11.008.

Milford D, Rosbach N, Bendszus M, and Heiland S. 2015. Mono-exponential fitting in T2-relaxometry: relevance of offset and first echo. PLoS ONE 10:e0145255. DOI: 10.1371/journal.pone.0145255.

Minn YA, Schellenberg D, Maxim P, Suh YJ, McKenna S, Cox B, Dieterich S, Xing L, Graves E, A Goodman K, Chang D, and C Koong A. 2009. Pancreatic tumor motion on a single planning 4D-CT does not correlate with intrafraction tumor motion during treatment. Am J Clin Oncol 32:364–8. DOI: 10.1097/COC.0b013e31818da9e0.

Moertel C, Frytak S, Hahn G, O'Connell J, Reitemeier J, Rubin J, Schutt J, Weiland H, Childs S, Holbrook A, Lavin T, Livstone E, Spiro H, Knowlton A, Kalser M, Barkin J, Lessner H, Kaplan R, Ramming K, and Novak W. 1981. Therapy of locally unresectable pancreatic carcinoma: a randomized comparison of high dose (6000 rads) radiation alone, moderate dose radiation (4000 rads + 5-fluorouracil), and high dose radiation + 5-fluorouracil: The Gastrointestinal Tumor Study Group. Cancer 48:1705–1710. DOI: 10.1002/1097-0142(19811015)48:8<1705::AID-CNCR2820480803>3.0.CO;2-4.

Möhler C, Russ T, Wohlfahrt P, Elter A, Runz A, Richter C, and Greilich S. 2018. Experimental verification of stopping-power prediction from single- and dual-energy computed tomography in biological tissues. Phys Med Biol 63. DOI: 10.1088/1361-6560/aaa1c9.

Mori S, Yanagi T, Hara R, C Sharp G, Asakura H, Kumagai M, Kishimoto R, Yamada S, Kato H, Kandatsu S, and Kamada T. 2009. Comparison of respiratory-gated and respiratory-ungated planning in scattered carbon ion beam treatment of the pancreas using four-dimensional computed tomography. Int J Radiat Oncol Biol Phys 76:303–12. DOI: 10.1016/j.ijrobp.2009.05.026.

Muir C and J Balcom B. 2013. A comparison of magnetic resonance imaging methods for fluid content imaging in porous media. Magn Reson Chem 51. DOI: 10.1002/mrc.3947.

Mutic S and Dempsey JF. 2014. The ViewRay system: magnetic resonance-guided and controlled radiotherapy. Semin Radiat Oncol 24:196–199. DOI: 10.1016/j.semradonc.2014.02.008.

Naumann P, Habermehl D, Welzel T, Debus J, and Combs S. 2013. Outcome after neoadjuvant chemoradiation and correlation with nutritional status in patients with locally advanced pancreatic cancer. Strahlenther Onkol 189:745–752. DOI: 10.1007/s00066-013-0393-3.

Newhauser W, Fontenot J, Koch N, Dong L, Lee A, Zheng Y, Waters L, and Mohan R. 2007. Monte Carlo simulations of the dosimetric impact of radiopaque fiducial markers for proton radiotherapy of the prostate. Phys Med Biol 52:2937–52. DOI: 10.1088/0031-9155/52/11/001.

Newhauser W and Zhang R. 2015. The physics of proton therapy. Phys Med Biol 60:R155–R209. DOI: 10.1088/0031-9155/60/8/R155.

Oborn B, Dowdell S, Metcalfe P, Crozier S, Mohan R, and Keall P. 2015. Proton beam deflection in MRI fields: Implications for MRI-guided proton therapy. Med Phys 42:2113–2124. DOI: 10.1118/1.4916661.

Oborn BM, Dowdell S, Metcalfe PE, Crozier S, Mohan R, and Keall PJ. 2017. Future of medical physics: Real-time MRI-guided proton therapy. Med Phys 44:e77–e90. DOI: 10.1002/mp.12371.

Och JG, Clarke GD, Sobol WT, Rosen CW, and Mun SK. 1992. Acceptance testing of magnetic resonance imaging systems: Report of AAPM Nuclear Magnetic Resonance Task Group No. 6. Med Phys 19:217–229. DOI: 10.1118/1.596903. eprint: https://aapm.onlinelibrary.wiley.com/doi/pdf/10.1118/1.596903.

Paganelli C, Whelan B, Peroni M, Summers P, F Fast M, van de Lindt T, McClelland J, Eiben B, Keall P, John Lomax A, Riboldi M, and Baroni G. 2018. MRI-guidance for motion

management in external beam radiotherapy: current status and future challenges. Phys Med Biol 63. DOI: 10.1088/1361-6560/aaebcf.

Paganetti H. 2012. Range uncertainties in proton therapy and the role of Monte Carlo simulations. Phys Med Biol 57:R99–117. DOI: 10.1088/0031-9155/57/11/R99.

Palmans H and Verhaegen F. 1997. Calculated depth dose distributions for proton beams in some low-Z materials. Phys Med Biol 42:1175–1183.

Pappas E, Alshanqity M, Moutsatsos A, Lababidi H, Alsafi K, Georgiou K, Karaiskos P, and Georgiou E. 2017. MRI-related geometric distortions in stereotactic radiotherapy treatment planning: evaluation and dosimetric impact. Technol Cancer Res Treat 16:1120–1129. DOI: 10.1177/1533034617735454.

Park W, M Yan B, Schellenberg D, Kim J, T Chang D, Koong A, Patalano C, and Van Dam J. 2010. EUS-guided gold fiducial insertion for image-guided radiation therapy of pancreatic cancer: 50 successful cases without fluoroscopy. Gastrointest Endosc 71:513–8. DOI: 10.1016/j.gie.2009.10.030.

Phillips MH, Pedroni E, Blattmann H, Boehringer T, Coray A, and Scheib S. 1992. Effects of respiratory motion on dose uniformity with a charged particle scanning method. Phys Med Biol 37:223–233. DOI: 10.1088/0031-9155/37/1/016.

Pieper S, Halle M, and Kikinism R. 2004. 3D Slicer. Proc IEEE Int Symp Biomed Imaging 1:632–635.

Pollard M, Wen J, Sadagopan Z, Wang R, and Ibbott GJ. 2017. The future of image-guided radiotherapy will be MR-guided. Br J Radiol 90:20160667. DOI: 10.1259/bjr.20160667.

Preston T. 1898. Radiation phenomena in a strong magnetic field. Sci Trans R Dubl Soc 6:385–389.

Raaymakers B, Jürgenliemk-Schulz I, Bol G, Glitzner M, Kotte ANTJ, van Asselen B, de Boer JCJ, Bluemink J, Hackett S, Moerland M, Woodings SJ, Wolthaus JWH, van Zijp L, Philippens M, Tijssen R, Kok J, de Groot-van Breugel EN, Kiekebosch I, Meijers LTC, and Lagendijk JJW. 2017. First patients treated with a 1.5 T MRI-Linac: Clinical proof of

concept of a high-precision, high-field MRI guided radiotherapy treatment. Phys Med Biol 62:L41–L50. DOI: 10.1088/1361-6560/aa9517.

Rank C, Heußer T, Buzan MTW, Wetscherek A, Freitag M, Dinkel j, and Kachelrieß M. 2016. 4D respiratory motion-compensated image reconstruction of free-breathing radial MR data with very high undersampling. Magn Reson Med 77:n/a–n/a. DOI: 10.1002/mrm.26206.

Riou O, Moscardo C, Fenoglietto P, Deshayes E, Tetreau R, Prunaretty J, Lenglet A, Assenat E, Ychou M, Guiu B, Ailleres N, Bedos L, and Azria D. 2017. SBRT planning for liver metastases: A focus on immobilization, motion management and planning imaging techniques. Rep Pract Oncol Radiother 22. DOI: 10.1016/j.rpor.2017.02.006.

Robin T and Goodman KA. 2017. Radiation therapy in the management of pancreatic adenocarcinoma: Review of current evidence and future opportunities. Chin Clin Oncol 6:28–28. DOI: 10.21037/cco.2017.06.12.

Rosenblatt E and Zubizarreta E. 2017. Radiotherapy in cancer care: facing the global challenge. International Atomic Energy Agency.

Roser M and Ritchie H. 2019. Cancer. Our World in Data. [Aktualisiert am 01.04.2018 , Aufruf am: 12.05.2019] URL: https://ourworldindata.org/cancer.

Rouvière O, Reynolds C, Le Y, Lai J, Roberts L, Felmlee J, and Ehman R. 2006. Fiducial markers for MR histological correlation in ex vivo or short-term in vivo animal experiments: a screening study. J Magn Reson Imaging 23:50–59. DOI: https://doi.org/10.1002/jmri.20466.

Rylander S, Thörnqvist S, Haack S, Pedersen E, and Paul Muren L. 2011. Intensity profile based measurement of prostate gold markers influence on 1.5 and 3T diffusion-weighted MR images. Acta Oncol 50:866–72. DOI: 10.3109/0284186X.2011.590523.

Sabati M and Maudsley A. 2013. Fast and high-resolution quantitative mapping of tissue water content with full brain coverage for clinically-driven studies. Magn Reson Imaging 31. DOI: 10.1016/j.mri.2013.08.001.

Scheffler K and Lehnhardt S. 2003. Principles and applications of balanced SSFP techniques. Eur Radiol 13:2409–18. DOI: 10.1007/s00330-003-1957-x.

Schellhammer SM, Hoffmann AL, Gantz S, Smeets J, van der Kraaij E, Quets S, Pieck S, Karsch L, and Pawelke J. 2018. Integrating a low-field open MR scanner with a static proton research beam line: proof of concept. Phys Med Biol 63:23LT01. DOI: 10.1088/1361-6560/aaece8.

Scherman Rydhög J, Jølck R, Andresen T, and Munck af Rosenschold P. 2015. Quantification and comparison of visibility and image artifacts of a new liquid fiducial marker in a lung phantom for image-guided radiation therapy. Med Phys 42:2818–2826. DOI: 10.1118/1.4919616.

Scherman Rydhög J, Mortensen S, Larsen K, Clementsen P, Jølck R, Josipovic M, Aznar M, Specht L, Andresen T, Munck af Rosenschold P, and Persson G. 2016. Liquid fiducial marker performance during radiotherapy of locally advanced non small cell lung cancer. Radiother Oncol 121:64–69. DOI: 10.1016/j.radonc.2016.06.012.

Scherman Rydhög J, Perrin R, Jølck R, Gagnon-Moisan F, Richter Larsen K, Clementsen P, Riisgaard de Blanck S, Persson G, Weber D, Lomax T, Andresen T, and Munck af Rosenschold P. 2017. Liquid fiducial marker applicability in proton therapy of locally advanced lung cancer. Radiother Oncol 122. DOI: 10.1016/j.radonc.2016.12.027.

Schneider S, Aust D, Brückner S, Welsch T, Hampe J, Troost EG, and Hoffmann A. 2019b. Detectability and structural stability of a liquid fiducial marker in fresh ex vivo pancreas tumour resection specimen on CT and 3T MRI. Strahlenther Onkol 195:756–763. DOI: 10.1007/s00066-019-01474-1.

Schneider S, Dolde K, Engler J, Hoffmann A, and Pfaffenberger A. 2019a. Commissioning of a 4D MRI phantom for use in MR-guided radiotherapy. Med Phys 46:25–33. DOI: 10.1002/mp.13261.

Schneider S, Jølck RI, Troost EGC, and Hoffmann AL. 2018. Quantification of MRI visibility and artifacts at 3T of liquid fiducial marker in a pancreas tissue-mimicking phantom. Med Phys 45:37–47. DOI: 10.1002/mp.12670.

Shamonin D, Bron E, Lelieveldt B, Smits M, Klein S, and Staring M. 2014. Fast parallel image registration no CPU and GPU for diagnostic classification of alzheimer's disease. Front Neuroinform 7:1–15. DOI: 10.3389/fninf.2013.00050.

Siegel R, Miller K, and Jemal A. 2015. Cancer statistics, 2015. CA Cancer J Clin 65:5–29. DOI: 10.3322/caac.21254.

Snider JW, Oermann EK, Chen VJ, Rabin J, Suy S, Yu X, Vahdat S, Collins SP, Banovac F, Anderson E, and Collins BT. 2012. CyberKnife with tumor tracking: an effective treatment for high-risk surgical patients with single peripheral lung metastases. Front Oncol 2:63. DOI: 10.3389/fonc.2012.00063.

Soher B, Dale B, and M Merkle E. 2007. A review of MR physics: 3T versus 1.5T. Magn Reson Imaging Clin N Am 15:277–90, v. DOI: 10.1016/j.mric.2007.06.002.

Soliman A, Chugh B, Keller B, Sahgal A, and Song W. 2016. SU-F-I-15: Evaluation of a new MR-compatible respiratory motion device at 3T. Med Phys 43:3389–3390. DOI: 10.1118/1.4955843.

Stefanowicz S, Stützer K, Zschaeck S, Jakobi A, and Troost EGC. 2018. Comparison of different treatment planning approaches for intensity-modulated proton therapy with simultaneous integrated boost for pancreatic cancer. Radiat Oncol 13:228. DOI: 10.1186/s13014-018-1165-0.

Stemkens B, Tijssen R, Senneville B, Lagendijk JJ, and Berg C. 2016. Image-driven, model-based 3D abdominal motion estimation for MR-guided radiotherapy. Phys Med Biol 61:5335–5355. DOI: 10.1088/0031-9155/61/14/5335.

Terry J, Milovancev M, and Nemanic S. 2014. In vitro evaluation of a novel fiducial marker for computed tomography and magnetic resonance imaging of soft tissues in small animals. Am J Vet Res 75:974–81. DOI: 10.2460/ajvr.75.11.974.

Van Tienhoven G, Gouma D, and Richel D. 2011. Review: Neoadjuvant chemoradiotherapy has a potential role in pancreatic carcinoma. Ther Adv Med Oncol 3:27–33. DOI: 10.1177/1758834010383150.

Troost E, Menkel S, Enghardt W, Hytry J, Kunath D, Makocki S, Hoffmann A, and Jølck R. 2017. EP-1710: Chemical stability of BioXmark® following normofractionated and single-fraction proton beam therapy. Radiother Oncol 123:S937–S938. DOI: 10.1016/S0167-8140(17)32242-9.

Tyagi N, Fontenla S, Zhang J, Cloutier M, Kadbi M, Mechalakos J, Zelefsky M, Deasy J, and Hunt M. 2017. Dosimetric and workflow evaluation of first commercial synthetic CT software for clinical use in pelvis. Phys Med Biol 62. DOI: 10.1088/1361-6560/aa5452.

Van der Horst A, Wognum S, Fajardo R, de Jong R, E van Hooft J, Fockens P, van Tienhoven G, and Bel A. 2013. Interfractional position variation of pancreatic tumors quantified using intratumoral fiducial markers and daily cone beam computed tomography. Int J Radiat Oncol Biol Phys 87. DOI: 10.1016/j.ijrobp.2013.05.001.

Van Gelder R, Wong S, Le A, Podreka A, Briggs A, Haddad C, and Hardcastle N. 2018. Experience with an abdominal compression band for radiotherapy of upper abdominal tumours. J Med Radiat Sci 65:48–54. DOI: 10.1002/jmrs.254.

Varadarajulu S, Trevino J, Shen S, and Jacob R. 2010. The use of endoscopic ultrasound-guided gold markers in image-guided radiation therapy of pancreatic cancers: A case series. Endoscopy 42:423–5. DOI: 10.1055/s-0029-1243989.

Vashaee S, Goora F, Britton M, Newling B, and Balcom B. 2014. Mapping B1-induced eddy current effects near metallic structures in MR images: A comparison of simulation and experiment. J Magn Reson 250. DOI: 10.1016/j.jmr.2014.10.016.

Verellen D, de ridder M, and Storme G. 2008. A (short) history of image-guided radiotherapy. Radiother Oncol 86:4–13. DOI: 10.1016/j.radonc.2007.11.023.

Versteijne E, Gurney-champion O, Horst A, Lens E, Willemijn Kolff M, Buijsen J, Ebrahimi G, Neelis K, Rasch C, Stoker J, van Herk M, Bel A, and van Tienhoven G. 2017. Considerable interobserver variation in delineation of pancreatic cancer on 3DCT and 4DCT: A multi-institutional study. Radiat Oncol 12. DOI: 10.1186/s13014-017-0777-0.

Villeirs G, Vaerenbergh KV, Vakaet LAML, Bral S, Claus FP, Neve WD, Verstraete KL, and Meerleer GOD. 2005. Interobserver delineation variation using CT versus combined

CT + MRI in intensity–modulated radiotherapy for prostate cancer. Strahlenther Onkol 181:424–430.

Vincent A, Herman J, Schulick R, Hruban R, and Goggins M. 2011. Pancreatic cancer. Lancet 13:607–620. DOI: 10.1016/S0140-6736(10)62307-0.

Von Siebenthal K, Székely G, Gamper U, Boesiger P, Lomax A, and Cattin P. 2007. 4D MR imaging of respiratory organ motion its variability. Phys Med Biol 52:1547–64. DOI: 10.1088/0031-9155/52/6/001.

Wang D, Doddrell D, and G C. 2004. A novel phantom and method for comprehensive 3-dimensional measurement and correction of geometric distortion in magnetic resonance imaging. Magn Res Imaging 22:529–42. DOI: 10.1016/j.mri.2004.01.008.

Wilson RR. 1946. Radiological use of fast protons. Radiology 47. PMID: 20274616:487–491. DOI: 10.1148/47.5.487. eprint: https://doi.org/10.1148/47.5.487.

Windischberger C, Robinson S, Rauscher A, Barth M, and Moser E. 2004. Robust field map generation using a triple-echo acquisition. J Magn Reson Imaging 20:730–4. DOI: 10.1002/jmri.20158.

Wong M, Jiang J, Liang Y, Fang Y, Yeung S, and Sung J. 2017. Global temporal patterns of pancreatic cancer and association with socioeconomic development. Sci Rep 7. DOI: 10.1038/s41598-017-02997-2.

Wroe AJ, Bush DA, and Slater JD. 2014. Immobilization considerations for proton radiation therapy. Technol Cancer Res Treat 13:217–226. DOI: 10.7785/tcrt.2012.500376.

Yamazaki H, Nishiyama K, Tanaka E, Koiwai K, Shikama N, Ito Y, Arahira S, Tamamoto T, Shibata T, Tamaki Y, Kodaira T, and Oguchi M. 2007. Dummy run for a phase II multi-institute trial of chemoradiotherapy for unresectable pancreatic cancer: inter-observer variance in contour delineation. Anticancer Res 27 4C:2965–2971.

Yarnykh V. 2007. Actual flip-angle imaging in the pulsed steady state: A method for rapid three-dimensional mapping of the transmitted radiofrequency field. Magn Reson Med 57:192–200. DOI: 10.1002/mrm.21120.

Zeeman P. 1896. Ueber einen Einfluss der Magnetisierung auf die Natur des von einer Substanz emittirten Lichtes. Verh Physi Ges Berl 15:128–130.

Zhang Y, Huth I, Weber D, and Lomax A. 2018. A statistical comparison of motion mitigation performances and robustness of various pencil beam scanned proton systems for liver tumour treatments. Radiother Oncol 128. DOI: 10.1016/j.radonc.2018.01.019.

Appendix

A Gel phantom for assessment of MR properties of fiducial markers

A.1 Sequence parameter

Relaxometry of gel samples

In Table A.1 the pulse sequence parameters are listed that were used for relaxometry of the initial gel samples. This was performed as an optimization procedure to determine the optimal aggarose concentration of the gel in order to mimic the T_1 and T_2 relaxation times of *in vivo* pancreas tissue. Besides T_1 mapping by a dual flip angle (FA) method and T_2 mapping by a multi-echo (8 echos) spin echo (SE) method, a B_1 map was determined based on a dual repetition-time (TR) gradient-echo (GRE) method for correction of the spatial inhomogeneities in the radio-frequency (RF) transmit field.

Table A.1: MRI sequence parameters for T_1 and T_2 mapping of prepared gel samples. B_1 mapping was additionally performed for correction of B_1 inhomogeneities for accurate calculation of the T_1 map.

Sequence	Dual TR GRE (B_1 mapping)	Dual FA GRE (T_1 mapping)	8-echo SE (T_2 mapping)
Field-Of-View FOV / mm³	120×120×20	120×120×20	120×120×20
Resolution / mm³	0.94×0.94×3	0.94×0.94×2	0.94×0.94×2
Echo Time TE / ms	1.0	2.3	20 + 7×20
Repetition Time TR / ms	312 / 412	20	2000
Flip Angle FA / °	12	5 / 17	90
Pixel Bandwith BW / Hz	2463	2205	2367

Quantitative evaluation of markers in phantom

For quantification of MRI visibility of the tested solid fiducial markers, a T_2^* map was created based on a multi-echo spoiled gradient-echo (SPGR) sequence and for the liquid markers a ρ(H) map was created based on a multi-echo gradient-and-spin echo (GRaSE) sequence. For the evaluation of induced artefacts a ΔB_0 map was created based on the phase information of the multi-echo SPGR sequence. For correction of T_1 decay within the GRaSE sequence, a T_1 map was created based on the golden standard inversion recovery spin-echo (IRSE) technique. For correction of spatial inhomogeneities in the RF transmit field, a B_1 map was created based on a dual TR GRE sequence. All relevant sequence parameters can be seen in Table A.2.

Table A.2: MRI sequence parameters for quantitative evaluation of fiducial marker visibility and artefacts by T_2^*-, ΔB_0- and ρ(H)-mapping.

Sequence	multi-echo SPGR	multi-echo GRaSE	IRSE	dual TR GRE
FOV / mm³	224×224 ×45	224×224 ×45	224×224 ×45	224×224 ×45
Res / mm³	1.0×1.0 ×1.5	1.0×1.0 ×1.5	1.0×1.0 ×1.5	1.0×1.0 ×5
TE / ms	2.3 + 7×4.6	16 +7×16	28.3	2.7
TR / ms	38	1500	5000	30/150
TI / ms	-	-	50/150/500/ 900/1500/3400	-
FA / °	12	90	90	60
BW / Hz	1236	1316	1296	355
NSA	2	1	1	1
SENSE	2	2	2	2

Qualitative evaluation of marker visibility in phantom

For validation of the determined source of visibility for liquid and solid markers, a qualitative evaluation was performed based on sequences used clinically for patients with PDAC (T_1 weighted 3D GRE (THRIVE), T_2 weighted Turbo SE, Diffusion weighted imaging and the reconstructed appearent diffusion coefficient map (ADC)) and a SE and GRE with two different echo times respectively. The sequence parameters can be seen in Table A.3. The liquid marker was visible in all contrasts created and visible with identical size in GRE at different echo times, whereas solid markers are poorly visible in SE sequences and appear substantially larger in GRE sequences with late echo times.

Table A.3: MRI sequence parameters for qualitative evaluation of fiducial marker visibility. Sequence (a)-(d) are clinically performed for patients with pancreatic carcinoma. Sequence (e)-(h) are two gradient echo and spin echo sequences with two different echo times respectively, to visualize the different visibility characteristics of the three marker types.

Sequence	(a) THRIVE	(b) TSE	(c,d) DWI/ADC	(e, f) GRE	(g,h) SE
FOV	302×302	375×299	375×303	200×200	200×200
/ mm³	×110	×109	×111	×30	×30
Res	1.5×1.5	1.0×1.1	2.0×2.0	1.0×1.0	1.0×1.0
/ mm³	×1.5	×3.0	×3.0	×1.5	×1.5
TE / ms	1.3	120	89	2.3 / 29.9	18 / 109
TR / ms	3.2	1127	2391	38	1500
FA / °	10	90	90	12	90
BW / Hz	723	291	23	858	1216
NSA	1	2	2	1	1
SENSE	2	2	2	1	1

The spherical gel phantom was scanned with a coronal T_1-weighted 3D gradient echo sequence with six different isotropic resolutions (0.125 mm³ – 64 mm³) for evaluation of visibility in dependence of resolution. The resulting six exemplary slices taken from each of the sequence are shown in Figure A.1. In accordance to our study, marker size was computed by segmentation of voxels which show a lower signal than the 3σ deviation of the mean signal of the phantom material. The apparent size of the four BioXmark® marker is shown in Figure A.2. The segmented volume was additionally analyzed regarding its minimal signal, from which the visible magnitude was evaluated as the maximum signal reduction in percent units [pu], where 1 represents a perfect signal void. The evaluation of the induced visible magnitude is shown in Figure A.3. It was observed that at the highest resolution the apparent marker size corresponded well with the injected marker volume. At lower resolution marker size is overestimated while visible magnitude decreases. Marker $\geq 25\,\mu$L were visible at all 6 resolutions.

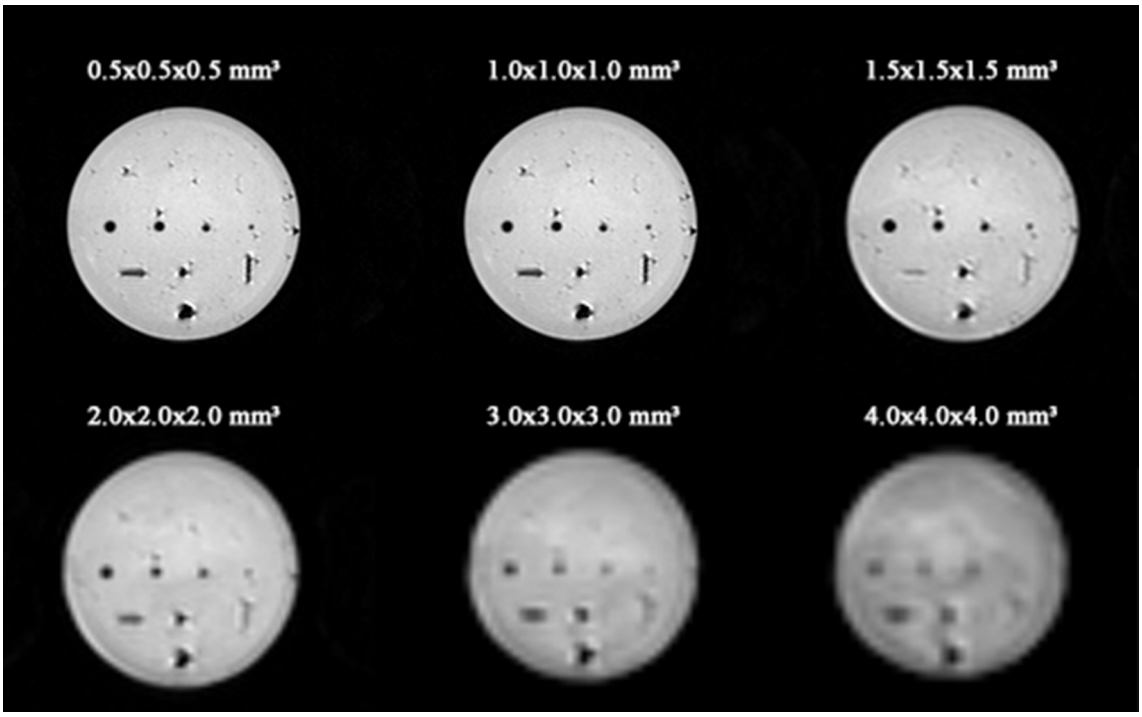

Figure A.1: Marker plane of the spherical phantom acquired with a coronal T_1-weighted 3D gradient echo sequence with six different resolutions

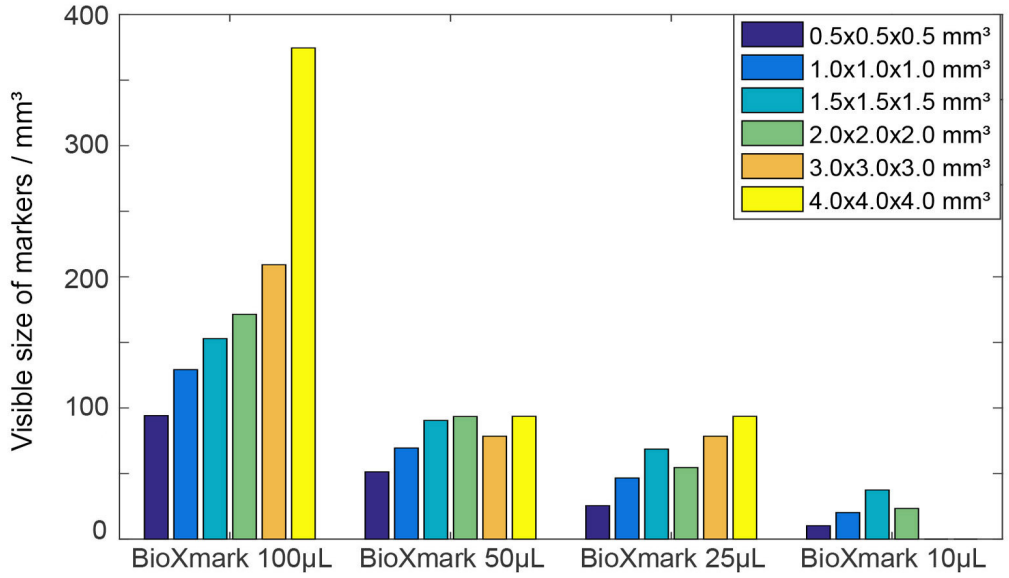

Figure A.2: Visible size of liquid markers of different size as a function of resolution.

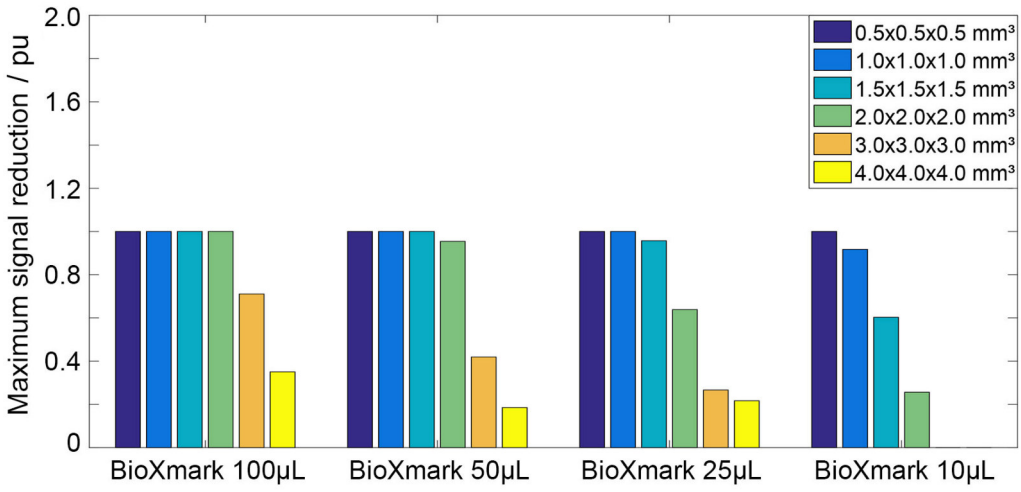

Figure A.3: Maximum signal reduction in liquid marker of different size as a function of resolution.

CT and MRI sequences for qualitative evaluation of liquid fiducial marker visibility in *ex vivo* pancreas tissue

The pancreas resection specimens injected with different sizes of liquid markers were scanned within two hours after resection with CT and MRI. The sequence parameters used can be seen in Table A.4. The scan parameter for both CT and MRI were oriented on clinically used protocols for patients with PDAC. In Figure A.4 all injected marker sides in all three resection specimen are presented for CT, T_1 weighted and T_2 weighted MRI. The markers are marked with a yellow circle. It is obivous that several markers can not be properly visualized in MRI but all marker sizes could be detected. Markers not visible in MRI showed a strong non-spherical gelation in CT.

Table A.4: CT and MRI sequence parameters for evaluation of fiducial marker visibility in freshly resected *ex vivo* tumorous pancreas tissue.

Imaging modality	MRI – T_1w	MRI – T_2w	CT
FOV / mm³	258×258×120	254×254×79	500×500×242
Res / mm³	1.51×1.51×3	0.76×0.76×3	0.98×0.98×2
TE / ms	1.4	80	-
TR / ms	3.2	800	-
FA / °	10	90	-
BW / Hz	721	290	-
NSA	1	1	-
SENSE	2	2	-
X-ray exposure / mAs	-	-	12
X-ray voltage / kVp	-	-	120

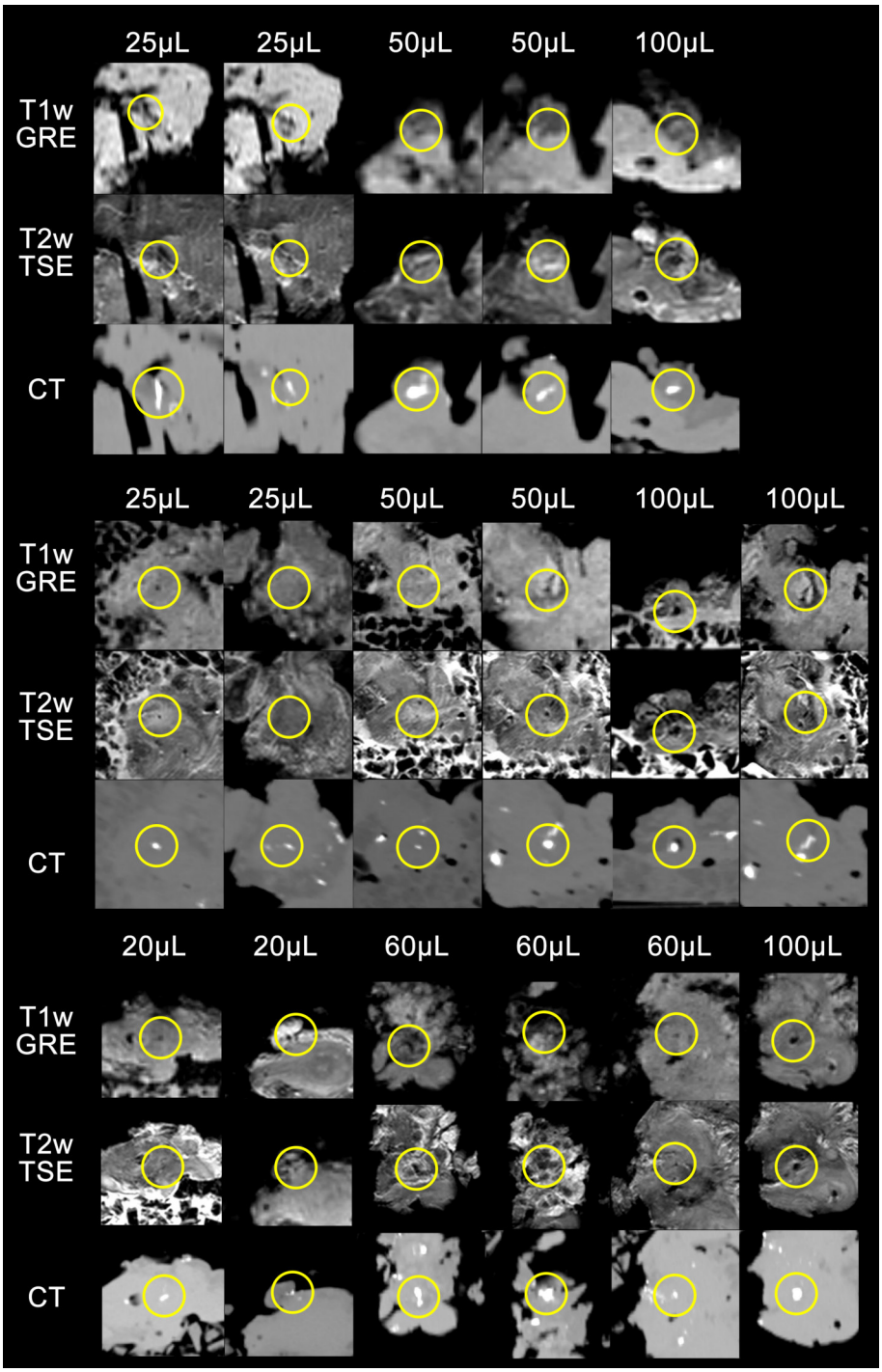

Figure A.4: Exemplary slices of all 17 marker injection sites in three resection specimens showing the markers circled in yellow in (from top to bottom) T_1 weighted gradient recalled echo (T_1-w GRE), T_2 weighted turbo spin echo (T_2-w TSE) and computed tomography (CT) for patient 1-3. Marker injections were ordered form smallest too largest with marker volumes between 20 µL – 100 µL.

B Motion phantom for QA

B.1 Geometric distortion analysis

In Table B.5 the sequence parameters are listed that were used for 3D distortion analysis with a reference CT and a T_1 weighted 3D GRE MRI sequence for evaluation.

Table B.5: Scan parameters used for MR and CT image acquisition of the 3D distortion grid and evaluation of the setup reproducibility.

Modality	MRI - 3D GRE	CT
Resolution / mm²	1.47×1.47	0.68×0.68
Slice thickness / mm	1.5	0.6
FOV / mm³	352×240×200	350×350×315
BW / Hz	721	-
TE/TR / ms	1.4/3	-
Tube voltage / kVp	-	80
Tube current time product / mAs	-	420

B.2 Target relaxometry

Table B.6 lists the pulse sequence parameters for relaxometry of the moving cylinder of the MR-Linac phantom for evaluation of T_1 and T_2 relaxation times in order to facilitate contrast optimization in balanced steady-state free-procession sequences, as used for motion depicting sequences.

B.3 Target tracking analysis

Table B.7 lists all sequence parameters used for motion assessment with the MR-Linac phantom. Single-slice 2D cine, orthogonal 2D cine and retrospectively resorted 4D MRI sequences were used for motion assessment and evaluated regarding their tracking accuracy.

Table B.6: MR sequence parameters used for relaxometry of the moving target and background gel for sequence optimization.

Sequence	IR SE [for T_1 mapping]	GraSE [for T_2 mapping]
Resolution / mm²	1.56×1.56	1.0×1.0
Slice thickness / mm	5	6
FOV / mm³	150×150×50	150×150×6
BW / Hz	2378	2331
TE/TR / ms	26/5000	8.6/5000
TI / ms	50/150/500/ 900/1500/3400	-
ΔTE / ms	-	8.6

Table B.8 lists all motion amplitudes and target velocities of the MR-Linac motion phantom used for assessment of tracking accuracy of the 3.0 T MR scanner.

Table B.7: Scan parameters used in MR and CT imaging for target motion characterization. For 3D motion the 2D cine MRI was acquired interleaved in transverse and sagittal orientation. For reconstruction of a 4D-MRI dataset 40 dynamics were acquired and then resorted to 8 respiratory phases.

Parameter	2D cine (1D motion)	2D cine (2D motion)	2D cine (3D motion)	4D MRI (3D motion)	CT (static)
Resolution / mm²	1.34×1.34	1.34×1.34	1.34×1.34	1.34×1.34	0.68×0.68
Slice thickness / mm	7	7	7	5	0.6
FOV / mm³	300×300×7	300×300×7	300×300×7	300×300×150	350×350×315
BW / Hz	1944	1944	1591	1151	-
TE/TR / ms	1.11/2.22	1.11/2.22	1.16/2.31	1.41/2.81	-
FA / °	30	30	30	30	-
SENSE factor	1	1	1.5	1.5	-
Temporal Resolution / s	0.489	0.489	0.489	0.403	-
Tube voltage / kVp	-	-	-	-	80
Tube current time product [mAs]	-	-	-	-	420

Table B.8: Comparison of pre-set and measured sinusoidal motion parameters. 3D motion was evaluated by means of orthogonal 2D cine MRI (a) and retrospectively binned 4D MRI (b).

Set parameters of target trajectory				Measured parameters of target trajectory			
IS amplitude / mm	AP amplitude / mm	LR ampltiude / mm	Frequency / Hz	IS amplitude / mm	AP amplitude / mm	LR ampltiude / mm	Frequency / Hz
20.0	0.0	0.0	0.2	20.2	-	0.2	0.199
10.0	0.0	0.0	0.2	10.1	-	0.0	0.199
20.0	0.0	0.0	0.1	20.2	-	0.1	0.199
0.0	5.0	0.0	0.2	-	4.6	0.4	0.100
0.0	0.0	5.0	0.2	-	0.5	4.6	0.199
20.0	5.0	0.0	0.2	20.1	4.6	-	0.199
20.0	0.0	5.0	0.2	20.1	-	4.7	0.199
0.0	5.0	5.0	0.2	-	4.8	4.7	0.199
7.5	5.0	2.5	0.2	7.5	4.7	2.3	0.2
7.5	5.0	2.5	0.2	7.5	4.7	2.4	-

Acknowledgement

First and foremost I would like to thank Prof. Wolfgang Enghardt for serving as my first thesis referee and for his approachable and relaxed personality during this phase. Secondly, I would like to thank Prof. Mark Ladd for acting as second thesis referee.

My special gratitude goes to Aswin Hoffmann for his supervision and especially his trust in me, letting me work on a completely new topic. I am very grateful for the amount of work you invested in the supervision of basically a side project and hours you invested in improving this thesis as well as my working style. I would also like to thank Esther Troost for her effective co-supervision and the effort she put in the extra work besides an already completely filled calender.

I furthermore like to thank my joint funding colleagues Kai Dolde and Asja Pfaffenberger for the cooperative work ethic and the fruitful measurement campaigns. I would also like to thank all the physicians Ivan Platzek and Fabian Lohaus who supported me by acquiring patients and helped during their MR scan. In this context I would also like to thank all study nurses Susi, Luisa and Annett for their help in organizing patients, the MTAs Julia, Danilo and Micha for their cooperative attitude and for their help in clinically implementing what we envisioned on paper as well as the colleagues from the ORD Mr. Herrmann, Ms. Gottlöber and Ms. Watza for helping us to realize the corset concept.

I would like to thank my group members and all the colleagues from OncoRay for their help and assistance in a variety of life and work situations. Particularly all colleagues who sacrificed their time for me to scan them as volunteers and optimize my pulse sequences and especially Felix for investing many hours to perform MRI scans when I was trapped in the bore myself. Thanks also for the coffee rounds that took my mind off work for one hour a day.

Finally, I would like to especially thank my significant other, my family and friends, the ones that entered my life and the ones who left it too early, foremost my parents for their help throughout all the years of university and promotion. The strong foundation you created was the basis on which I could follow my dreams without ever feeling the need to worry.

Erklärungen zur Eröffnung des Promotionsverfahrens

1. Hiermit versichere ich, dass ich die vorliegende Arbeit ohne unzulässige Hilfe Dritter und ohne Benutzung anderer als der angegebenen Hilfsmittel angefertigt habe; die aus fremden Quellen direkt oder indirekt übernommenen Gedanken sind als solche kenntlich gemacht.

2. Bei der Auswahl und Auswertung des Materials sowie bei der Herstellung des Manuskripts habe ich Unterstützungsleistungen von folgenden Personen erhalten:
   Dr. Aswin L. Hoffmann
   Dr. Esther G. C. Troost
   Dr. Rasmus I. Jølck
   Dr. Kai Dolde
   Dr. Asja Pfaffenberger
   M.Sc. Nils Peters
   Dr. Alexander Fieguth
   Dr. Karoline Pilz

3. Weitere Personen waren an der geistigen Herstellung der vorliegenden Arbeit nicht beteiligt. Insbesondere habe ich nicht die Hilfe eines kommerziellen Promotionsberaters in Anspruch genommen. Dritte haben von mir weder unmittelbar noch mittelbar geldwerte Leistungen für Arbeiten erhalten, die im Zusammenhang mit dem Inhalt der vorgelegten Dissertation stehen.

4. Die Arbeit wurde bisher weder im Inland noch im Ausland in gleicher oder ähnlicher Form einer anderen Prüfungsbehörde vorgelegt.

5. Die Inhalte dieser Dissertation wurden in folgender Form veröffentlicht und mit Genehmigung der jeweiligen Verlage verwendet:

   - Schneider S, Jølck RI, Troost EGC und Hoffmann AL. 2018. Quantification of MRI visibility and artifacts at 3T of liquid fiducial marker in a pancreas tissue-mimicking phantom. Med Phys 45:37–47. DOI: 10.1002/mp.12670
   - Schneider S, Dolde K, Engler J, Hoffmann A und Pfaffenberger A. 2019a. Commissioning of a 4D MRI phantom for use in MR-guided radiotherapy. Med Phys 46:25–33. DOI: 10.1002/mp.13261

- Schneider S, Aust D, Brückner S, Welsch T, Hampe J, Troost EG und Hoffmann A. 2019b. Detectability and structural stability of a liquid fiducial marker in fresh ex vivo pancreas tumour resection specimen on CT and 3T MRI. Strahlenther Onkol 195:756–763. DOI: 10.1007/s00066-019-01474-1
- Dolde K, Schneider S, Stefanowicz S, Alimusaj M, Flügel B, Saito N, Troost EGC, Pfaffenberger A und Hoffmann AL. 2019. Comparison of pancreatic respiratory motion management with three abdominal corsets for particle radiation therapy: Case study. J Appl Clin Med Phys 20:111–119. DOI: 10.1002/acm2.12613

6. Ich bestätige, dass es keine zurückliegenden erfolglosen Promotionsverfahren gab.
7. Ich bestätige, dass ich die Promotionsordnung der Medizinischen Fakultät Carl Gustav Carus der Technischen Universität Dresden anerkenne.
8. Ich habe die Zitierrichtlinien für Dissertationen an der Medizinischen Fakultät der Technischen Universität Dresden zur Kenntnis genommen und befolgt.

Dresden, 14. Mai 2020 _____

Erklärung über die Einhaltung der gesetzlichen Bestimmungen

Hiermit bestätige ich die Einhaltung der folgenden aktuellen gesetzlichen Vorgaben im Rahmen meiner Dissertation

- das zustimmende Votum der Ethikkommission bei Klinischen Studien, epidemiologischen Untersuchungen mit Personenbezug oder Sachverhalten, die das Medizinproduktegesetz betreffen

☐ ~~die Einhaltung der Bestimmungen des Tierschutzgesetzes~~
nicht zutreffend

☐ ~~die Einhaltung des Gentechnikgesetzes~~
nicht zutreffend

- die Einhaltung von Datenschutzbestimmungen der Medizinischen Fakultät und des Universitätsklinikums Carl Gustav Carus.

Dresden, 14. Mai 2020 _____